

Dissertation

Mass and charge transport properties of Fe-doped SrTiO₃ thin films and their dependence on DC voltage

ausgeführt zum Zwecke der Erlangung des akademischen Grades
eines

Doktors der technischen Wissenschaften

unter der Leitung von

Univ.-Prof. Dipl.-Phys. Dr. Jürgen Fleig

am Institut für chemische Technologien und Analytik
Bereich Elektrochemie

eingereicht an der Technischen Universität Wien
Fakultät für Technische Chemie

von

Dipl.-Ing. Stefanie Huber

Matrikelnr. 0326163

Am Schauerberg 39/ A-3125 Statzendorf

Abstract

The main goal of this work was to investigate slightly (0.4mol%) Fe-doped SrTiO₃ (Fe-STO) thin films by means of impedance spectroscopy and DC measurements to achieve a better understanding of charge carrier transport in such thin films. The acceptor doped layers, with a layer thickness between 60 and 420 nm were prepared by pulsed laser deposition (PLD) on highly conductive Nb-doped SrTiO₃ substrates. This allowed an epitaxial film growth and electrochemical measurements perpendicular to the film.

Impedance spectroscopic measurements were firstly performed without applied bias. The investigated samples exhibit only one pronounced impedance feature and a conductivity which is about three orders of magnitude lower than the grain bulk conductivity of a polycrystalline sample. Also the activation energy (ca. 1.6 eV between 350°C to 700°C) was much larger than that of a typical grain bulk. This is attributed to the probably increased density of dislocations. Space charge layers accompanying dislocations most probably lead to a "homogeneously" depleted layer with decreased conductivity. Still the thickness dependence of the resistance and the capacitance indicate that the entire "bulk" of the film is probed.

Impedance measurements were then extended by applying an additional bias voltage. The monitored changes and the occurrence of additional features in the low frequency range of the spectra made it necessary to develop a physically reasonable equivalent circuit model. This model is based on frequency dependent sample changes due to oxygen vacancy motion and can also quantify the very special feature of inductive loops, often found upon bias. The resulting datasets were analyzed in terms of their bias-, temperature- and thickness-dependence.

The second part of this work deals with results which were achieved by DC measurements. Current-voltage curves were monitored for different layers under different temperatures and with a variation of measurement speed. Very different curves resulted for slow and fast recording rates. It was possible to relate the data from impedance measurements with the rate-dependent current-voltage characteristics and a prediction of the shape of the U-I curve from impedance data became possible. The slowly measured current-voltage curves were analyzed by means of the Wagner-Hebb polarization model. This means that the non-linearity of the slow current-voltage curve can be attributed to different steady states of the vacancy distribution at each voltage point.

On the other hand, the fast DC measurements showed a different and often a diminished non-linearity. Without established non-equilibrium steady state, the non-linearity of a fast U-I curve may be related to the existence of dislocations with space charges and their random location in the material. The development of a pn-junction in the thin layers is most probably the reason for the observed fast U-I curve after positive bias load.

Finally, also DC load and relaxation experiments were performed. The time dependence was analyzed for varying layer thickness and applied bias and this clearly confirms Wagner-Hebb type polarization of the samples. Hence, a modified version of resistive switching takes place in these thin films.

In summary, the combination of impedance spectroscopy and DC measurements allowed an in-depth investigation of Fe-doped SrTiO₃ thin films in terms of charge carrier motion and associated electrochemical properties. Several novel phenomena could be observed upon bias and confirm the importance of oxygen vacancy motion but also of space charges in polarized STO thin films.

Kurzfassung

Im Rahmen dieser Arbeit wurden SrTiO_3 Dünnschichten mit geringer Akzeptordotierung (0.4 mol% Fe), mit Hilfe von Impedanzspektroskopie und DC Messungen auf ihre elektrochemischen Eigenschaften hin untersucht. Mit Hilfe dieser geringen Mengen an Dotierelement konnten Schichten mit definierter und bekannter Defektkonzentration hergestellt werden. Das Ziel dieser Messungen bestand darin, die ablaufenden Ladungsträgertransportprozesse in diesen dünnen Schichten besser zu verstehen. Die Dünnschichten, die eine Dicke zwischen 60 und 420 nm aufweisen, wurden durch "pulsed laser deposition" (PLD) auf elektronisch leitendes Nb-dotiertes SrTiO_3 Substratmaterial aufgebracht. Durch die Wahl dieses Trägermaterials konnte sowohl ein epitaktisches Schichtwachstum, als auch eine elektrische Kontaktierung der Schicht ermöglicht werden.

Zunächst wurden Impedanzmessungen ohne zusätzlich angelegte Gleichspannung (Bias) durchgeführt, welche für die untersuchten Schichten lediglich einen Halbkreis im Impedanzspektrum lieferten. Die ermittelte Gesamtleitfähigkeit für die dünnen STO Filme liegt dabei ungefähr drei Größenordnungen sowohl unter den Werten für Korn- als auch für Korngrenzleitfähigkeit einer polykristallinen makroskopischen Probe. Auch die ermittelte Aktivierungsenergie (1.6 eV zwischen 350°C und 700°C) ist um einiges höher, als Werte für die typische thermische Aktivierung der Leitfähigkeit eines STO-Korns in polykristallinem Material. Die Ursache hierfür kann eine möglicherweise hohe Versetzungsdichte im untersuchten Volumen sein. Die sich ausbildenden Raumladungszonen in der unmittelbaren Umgebung dieser Versetzungen führen dazu, dass eine "homogene" Anreicherung an Ladungsträgern im gesamten Material stattfindet. Widerstände und Kapazitäten der unter-

schiedlichen Schichten zeigen eine Schichtdickenabhängigkeit, wodurch davon ausgegangen werden kann, dass mit der Messung das gesamte Volumen der dünnen Schicht erfasst wird.

Impedanzmessungen, die unter Anlegen einer zusätzlichen Gleichspannung durchgeführt wurden, lieferten Ergebnisse, die die Ausarbeitung eines physikalisch sinnvollen Ersatzschaltbildes unumgänglich machten. Dieses Ersatzschaltbild berücksichtigt die frequenzbedingten Veränderungen der Proben aufgrund der eintretenden Bewegung von Sauerstoffleerstellen. Mit diesem Modell konnte eine quantitative Analyse des im niederfrequenten Bereich zusätzlich auftretenden induktiven "Loops" durchgeführt werden. Die erhaltenen Daten wurden im Folgenden in Bezug auf ihre Bias-, Temperatur- und Schichtdickenabhängigkeit ausgewertet.

Weiters wurden Strom-Spannungskennlinien bei unterschiedlichen Temperaturen und in unterschiedlichen Geschwindigkeiten (schnell = im Bereich von Sekunden, langsam = im Bereich von Stunden) aufgenommen, wobei für die verschiedenen Messzeiten deutliche Unterschiede in den gemessenen Strom-Spannungskurven beobachtet werden konnten. Im Zuge der Auswertung wurden die erhaltenen Impedanzspektren mit den U-I Kurven korreliert, wodurch eine Vorhersage über die Form der U-I Kurven anhand der Impedanzdaten möglich wurde.

Die langsam gemessenen Strom-Spannungskennlinien wurden im Hinblick auf ein Wagner-Hebb ähnliches Verhalten hin ausgewertet und entsprechend diskutiert. Die Ursache für die Nichtlinearität der langsamen U-I Kennlinie kann darin gefunden werden, dass in jedem angelegten Spannungspunkt ein neuer stationärer Zustand erreicht wird, und damit die Sauerstoffleerstellenverteilung immer wieder neu verändert, eingestellt und elektrochemisch abgegriffen wird.

Die schnell gemessenen U-I Kennlinien wiesen ebenfalls eine deutliche Nichtlinearität auf, wobei im Fall dieses Experiments nicht-stationäre Zustände gemessen wurden, und der nichtlineare Verlauf der Kurven der Existenz von Versetzungen und deren ungeordneten Verteilung im Material zugeordnet werden kann. Für den anodischen Ast der Kurve (z.B. Startspannung von +400 mV) kann ein sich ausbildender pn-Übergang für das nichtlineare Verhalten verantwortlich gemacht werden.

In einem weiteren Experiment wurden die Proben konstanter DC Spannung ausgesetzt, und die Veränderungen unter Feld zeitlich verfolgt. Die Ergebnisse deuten auch in diesem Fall auf ein Wagner-Hebb ähnliches Verhalten hin, welches als eine abgeschwächte Form von sogenanntem "resistive switching" betrachtet werden kann.

Zusammenfassend kann die Kombination aus impedanzspektroskopischen Untersuchungen und Gleichspannungsmessungen einen tieferen Einblick in die Transportmechanismen von Ladungsträgern in dünnen Schichten gewähren. Mehrere neue Phänomene konnten unter einer zusätzlich angelegten DC Spannung beobachtet werden. Diese Ergebnisse bestätigen die Bedeutsamkeit der Bewegung von Sauerstoffleerstellen im SrTiO_3 und zeigen, dass der komplexe Einfluss von Raumladungszonen an Versetzungen in die Interpretation der Ergebnisse einfließen muss.

Contents

1	Introduction	1
2	Basic Aspects and Status of Research	4
2.1	Defect chemistry and nonstoichiometry in SrTiO ₃	4
2.2	Theory of space charge layers and the mesoscopic effect	9
2.3	Polarization processes in SrTiO ₃ – Resistance degradation, Wagner-Hebb polarization and resistive switching	15
2.3.1	Resistance degradation	15
2.3.2	Wagner-Hebb polarization	17
2.3.3	Resistive switching	19
3	Experimental	24
3.1	Thin layer preparation by pulsed laser deposition (PLD)	24
3.2	Microelectrode preparation by photolithography	26
3.3	Electrochemical measurements	27
3.4	¹⁸ O tracer experiments and SIMS	30
4	Structural Characterization	32
4.1	Atomic force microscopy (AFM)	32
4.2	Transmission electron microscopy (TEM)	34
5	Results and Discussion: Impedance Measurements With and Without Bias Voltage Performed on Thin Fe-doped SrTiO₃ Films	36
5.1	Impedance measurements of SrTiO ₃ layers without applied bias	36
5.2	Impedance measurements performed under variable bias voltage	42
5.2.1	Quantitative analysis of impedance spectroscopy data . . .	43

5.2.2	Analysis of resistance and capacitance values in dependence of applied bias and temperature	47
5.2.3	Comparison of all observed variations obtained by AC measurements under bias	62
5.2.4	Kramers-Kronig test of the measured impedance data . .	65
6	Results and Discussion: Partial Pressure Measurements on Fe-doped SrTiO₃ Thin Films under Oxidizing Conditions	68
7	Results and Discussion: Current-Voltage Behavior of Thin Fe-doped SrTiO₃ Films Investigated in Two Different Time Modes	75
7.1	U-I characteristics: Slow measurements	76
7.2	U-I characteristics: Fast measurements	82
7.3	Current-voltage characteristics compared with impedance data .	91
8	Results and Discussion: DC load and Relaxation Experiments	94
9	Additional Measurements	101
9.1	Investigations of SrTiO ₃ thin films after an additional annealing step	101
10	Conclusions	110
11	Acknowledgements	135
12	Curriculum Vitae	138

Introduction

Over the last few decades a vast amount of experimental work was performed on perovskite-type materials, with one focus on clarifying defect chemical questions.^[1-13] SrTiO₃ is one of the most intensively investigated materials in this field of research. Consequently its bulk defect chemistry is largely understood.^[14-24] Therefore, it serves as model material for mixed ionic-electronic conducting oxides in general and for large band-gap perovskite-type materials including BaTiO₃ and Pb(Zr,Ti)O₃ in particular.

Fundamental experiments were performed on single crystalline, polycrystalline and even bicrystalline SrTiO₃ samples, and revealed the importance of oxygen vacancies, electrons and holes as relevant charge carriers.^[18,25-34] Variations in temperature and partial pressure can cause changes concerning the majority charge carrier and modify the electrochemical properties in undoped as well as in acceptor (e.g. Fe and Ni)^[16] and donor (e.g. La and Nb)^[35] doped SrTiO₃. In this thesis Fe-doped SrTiO₃, with a slight amount of dopant (0.4mol%) was investigated. The incorporation of Fe on a Ti site is primarily compensated by oxygen vacancies, at least at high oxygen partial pressures.^[16,21] These oxygen vacancies play an important role regarding the incorporation and release reaction of oxygen, but are also involved in polarization phenomena, e.g. resistance degradation, Wagner-Hebb polarization and resistive switching.^[36-48] This is discussed in detail in Chapter 2.

Also internal (grain boundaries, dislocations) and external (surface) interfaces can be the cause of a changed electrochemical behavior. Results obtained for polycrystalline bulk SrTiO₃ reveal that grain boundaries play an extremely

important role concerning the transport of charge carriers through the material. The influence of grain boundaries and dislocations on the electrochemical properties of the material is of further interest, when either the grain size or the entire sample geometry is reduced.^[27,49–57]

SrTiO₃ thin films in particular are known to exhibit charge transport properties that differ from those of the bulk material.^[17,20,58–64] Furthermore, SrTiO₃ –as a thin film– exhibits a lot of interesting properties and thus might find several new applications, e.g. in memory devices based on resistive switching and sensing applications. Despite all these promising applications, the processes of mass and charge transport in such small dimensions are still not fully understood. Recently made investigations on nanocrystalline SrTiO₃ and on layers in the μm range pointed out that a distinct variation in the performance of the material exists due to the decreased size. Further details of the corresponding status of research is also given again in Chapter 2. However, so far the focus of research activities dealing with the defect chemistry of thin films did not extent much into the thickness range of a few 100 nm.

This lack of a systematically performed defect chemical characterization of SrTiO₃ thin films in the nanometer range is the main motivation of this work. The goal is to obtain more information on how charge transport in thin films differs from the situation reported for bulk material. Therefore, Fe-doped SrTiO₃ thin films were deposited on Nb-doped SrTiO₃ by pulsed laser deposition (PLD), and were experimentally investigated by means of electrical impedance spectroscopy, DC measurements and partial pressure dependent measurements.

- **Electrical impedance spectroscopy**

Impedance measurements without externally applied bias voltage were conducted with the focus on clarifying if changes in the overall conductivity of STO thin films can be observed compared to macroscopic samples. Furthermore, the nature of possible changes was analyzed and discussed in the light of mesoscopic effects. By applying an external electrical field, a migration process of charge carriers was induced in the thin films. Simultaneously performed impedance measurements allowed monitoring the effects of the modified charge carrier distribution due to stoichiometric polarization.

- **DC measurements**

Current-voltage characteristics were analyzed for layers with varying thickness. The DC measurements were made in two different time modes (fast = in the range of seconds, slow = in the range of hours) to gain information about the migrating charge carrier species. Furthermore, the obtained results could be compared with data achieved by impedance measurements.

In addition, DC load and relaxation experiments were conducted. From the characteristic times needed by the thin films to reach a new steady state, it is intended to get additional information about the charge carrier, that is responsible for the observed migration (under DC load) and diffusion (relaxation) process.

- **Partial pressure dependent measurements**

Temperature and partial pressure changes represent a powerful tool to achieve information on the partial conductivities. In literature, Brouwer diagrams were developed for bulk material^[21] as well as for thin layers in the range of micrometers^[63]. Recent investigations by Lupetin *et.al.*^[52] focused on the partial pressure behavior of nanocrystalline SrTiO₃ samples. From this report, the interesting question arises of how the situation changes, when the layer thickness further decreases into the 100 nm range and dislocations with surrounding space charge layers dominate the defect chemical behavior of the layers. This was the motivation to investigate the Fe-doped SrTiO₃ layers also under different partial pressures (100% and 1% oxygen atmosphere compared with measurements under air).

Basic Aspects and Status of Research

2.1 Defect chemistry and nonstoichiometry in SrTiO_3

SrTiO_3 (STO) represents one of the most intensely investigated perovskite-type oxides. Therefore, the defect chemistry of this large band gap mixed-conducting oxide is very well understood. This is also the reason why SrTiO_3 serves as model material for many electroceramic oxides. [1,15,16,18,21,23,25–30,33,36–38,49,57,65–68]

At a non-zero temperature, a finite defect concentration due to the configurational entropy exists in any solid material.^[2] Furthermore, it is a matter of fact that chemical and physical properties are affected by these point defects. For the description of the defect-chemical processes in SrTiO_3 the widely employed Kröger-Vink notation will be used throughout this thesis.^[69] In this notation system the defects are characterized by three symbols in the form S_P^C . S stands for the species of the occurring defect, e.g. vacancies (V), atoms or ions (e.g. Fe, La), holes (h) or electrons (e). The subscripted P denotes the species, which would occupy the lattice site in the unperturbed ideal crystal. For the sake of completeness it has to be mentioned, that an ion or atom located at an interstitial site of the lattice would be described by an i. In the case of SrTiO_3 , however, the formation of occupied interstitial sites can be neglected. Furthermore, the notation gives information about the effective charge of the defects (C), which is depicted by the superscript. The effective charge (C_e) is

Kröger-Vink notation

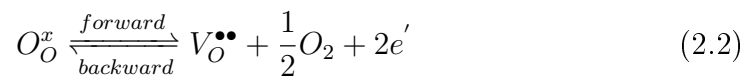
the charge located at the defect (z_d) with respect to the ideal charge of this lattice site in the unperturbed crystal (z_s) (see Eq. 2.1).

$$C_e = z_d - z_s \quad (2.1)$$

In short, missing cations create relative negatively ($'$) charged cation vacancies, whereas removed anions generate relative positively charged (\bullet) anion vacancies. Neutral defects are denoted by an x.

To completely describe the defect chemistry and its consequences for oxides in general and for SrTiO₃ in particular, compositional variations caused by interaction with the surrounding gas atmosphere have to be taken into account. It has to be emphasized that the incorporation and removal of oxygen due to partial pressure variations directly influences the presence and amount of charge carriers in the material which further strongly affects the behavior of STO under electrical field. The extent of nonstoichiometry caused by oxygen partial pressure changes is determined by the tendency of cations to change their valence states. Fig. 2.1 illustrates the changes in the electrical properties which come along with significant deviations from stoichiometric composition. For an undoped ionic oxide (MO) a stoichiometric point can be found where $[e'] = [h\bullet]$ and $[V_O^{\bullet\bullet}] = [V_M^{\prime\prime}]$ is valid. This oxide can then be changed into a metal-excess –n-conducting– material by releasing oxygen which involves formation of oxygen vacancies (see Eq. 2.2 forward direction of the reaction).

Nonstoichiometry



For a more specific quantification of defect concentrations in the near stoichiometric range, an assumption concerning the dominating defect formation is often made. Then simple equations describing the partial pressure dependent defect chemical conditions in oxides result. With regard to the investigated SrTiO₃, it is supposed that Schottky defect formation (K_s) overrules electronic defect formation (K_e)^[70] ($K_s > K_e$ see Eq. 2.3).

$$K_s = [V_M^{\prime\prime}] \cdot [V_O^{\bullet\bullet}] \quad \text{and} \quad K_e = [e'] \cdot [h\bullet] \quad (2.3)$$

Therefore, by taking the condition at the stoichiometric point and the mass action law (Eq. 2.4) into account, it can be shown that the concentration of

electrons in this regime (regime 1 in Fig. 2.2) depends on the oxygen partial pressure according to Eq. 2.5.

$$K_r = K_r^\circ \exp\left(-\frac{\Delta H_r}{kT}\right) = [V_{O^{\bullet\bullet}}][e']^2 p_{O_2}^{\frac{1}{2}} \quad (2.4)$$

$$[e'] = K_r^{\frac{1}{2}} K_s^{-\frac{1}{4}} p_{O_2}^{-\frac{1}{4}} \quad (2.5)$$

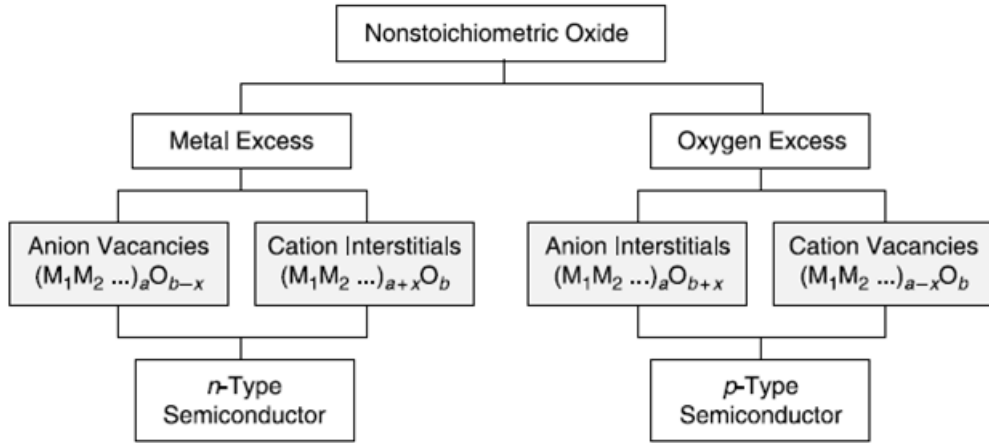


Figure 2.1

Fig. 2.1: Schematic picture of how non-stoichiometry influences the electrical properties in oxides by shifting the material into the n- as well as into the p-conducting regime^[70].

With a further decrease of the partial pressure (shifting into regime 2 depicted in Fig. 2.2) the dependence on the partial pressure changes. To describe this regime it is necessary to adapt the electroneutrality equation to $[e'] = 2[V_{O^{\bullet\bullet}}]$, by ignoring the minority defects. With this new approach Eq. 2.2 can be used to describe the adjusted defect concentration by:

$$[V_{O^{\bullet\bullet}}] = \frac{K_r}{[e']^2 p_{O_2}^{\frac{1}{2}}} \implies \frac{1}{2}[e']^3 = K_r p_{O_2}^{-\frac{1}{2}} \quad (2.6)$$

$$[e'] = \sqrt[3]{2} K_r^{\frac{1}{3}} p_{O_2}^{-\frac{1}{6}} \quad (2.7)$$

From Eq. 2.5 and Eq. 2.7 it can be concluded that by moving from regime 1 to regime 2 in the Brouwer diagram (Fig. 2.2) by lowering the partial pressure, the slope of the $[e']$ -curve changes from $-\frac{1}{4}$ to $-\frac{1}{6}$.^[70] An increasing oxygen partial pressure on the other hand leads to an oxygen-excess –p-conducting– compound. The considerations in terms of the partial pressure dependency are

analogous to those for decreasing p_{O_2} . However, owing to the reversed reaction path (Eq. 2.2 backward reaction path) the slopes for the $[e']$ - and $[h^\bullet]$ -curves become inverse and therefore positive values ($+\frac{1}{4}$ to $+\frac{1}{6}$) are obtained (see regime 3 in Fig. 2.2).

All assumptions which were made for binary oxides of the form MO_{1-x} become more complex for a ternary perovskite oxide like $SrTiO_3$. Fortunately, complications due to variations of the Sr/Ti ratio only occur at temperatures higher than 900°C .^[16] For this temperature regime the partial Schottky equilibrium (Eq. 2.8) has to be considered, as it is described in the work of Moos and Härtl^[23].

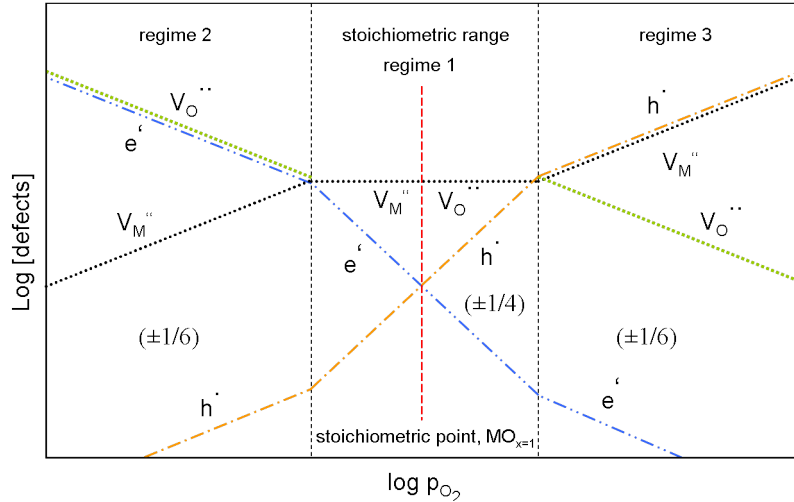
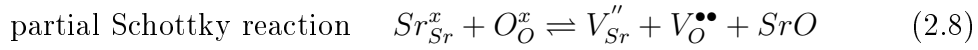


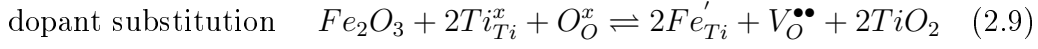
Figure 2.2

Fig. 2.2: Brouwer diagram for an undoped MO_X compound^[2].

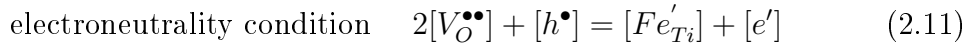
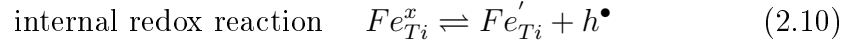
The experiments of the present work were made at temperatures between 325°C and 750°C . In this temperature region $SrTiO_3$ behaves as a pseudo-binary oxide, because all existing metal vacancies (V_{Sr}'') are frozen in (i.e. immobile) and therefore only act as intrinsic acceptor dopants. The disadvantage of this situation is the unknown defect concentration. To obtain $SrTiO_3$ with well-defined $V_O^{\bullet\bullet}$, e' and h^\bullet concentrations it can be deliberately acceptor doped with small amounts of Fe as it is the case in this work.

Iron is located on the Ti site and appears in the two valence states +III and +IV. It is worth mentioning that Fe^{4+} is stable in this case due to the almost ideally matching ion size in the lattice.^[16] This is in contrast to the situation in aqueous chemistry where Fe^{4+} is usually not stable. The incorporated Fe^{3+}

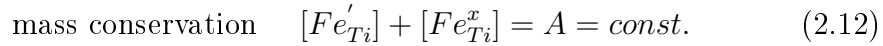
is primarily compensated by the formation of oxygen vacancies as illustrated by Eq. 2.9.



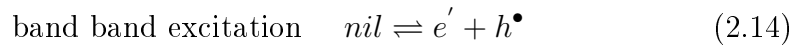
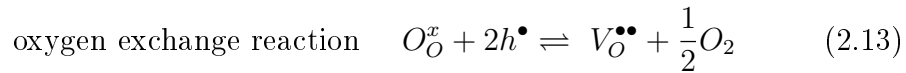
Only to a small extent electronic holes will be formed in the valence band (Eq. 2.10) to fulfill the demanded electroneutrality condition (Eq. 2.11).



The Fe^{3+}/Fe^{4+} ratio (i.e. Fe'_{Ti}/Fe_{Ti}^x ratio) in the material is governed by different parameters such as oxygen partial pressure, temperature and the total iron concentration.^[16] As described by Eq. 2.12 the sum of Fe^{3+} and Fe^{4+} is constant.



It is important to emphasize that the defect equilibria for the undoped case are also valid for the doped situation. Hence, again the oxygen exchange reaction with the ambient atmosphere (Eq. 2.13) and the band band excitation (Eq. 2.14) have to be considered.



Taking these two relevant reactions and additionally the electroneutrality condition (Eq. 2.11), the set of defect chemical reactions for Fe-doped $SrTiO_3$ are complete.^[16,18,21,24,30,33] This knowledge can now be used to obtain the Brouwer diagram for acceptor doped ternary oxides, as it is pictured in Fig. 2.3 (bottom diagram).

These concentrations are also reflected in the plot of the partial conductivities (Fig. 2.3 top diagram): There also charge and particularly mobility have to be considered. Therefore, electronic charge carriers dominate several regimes and cation vacancies are no longer present.

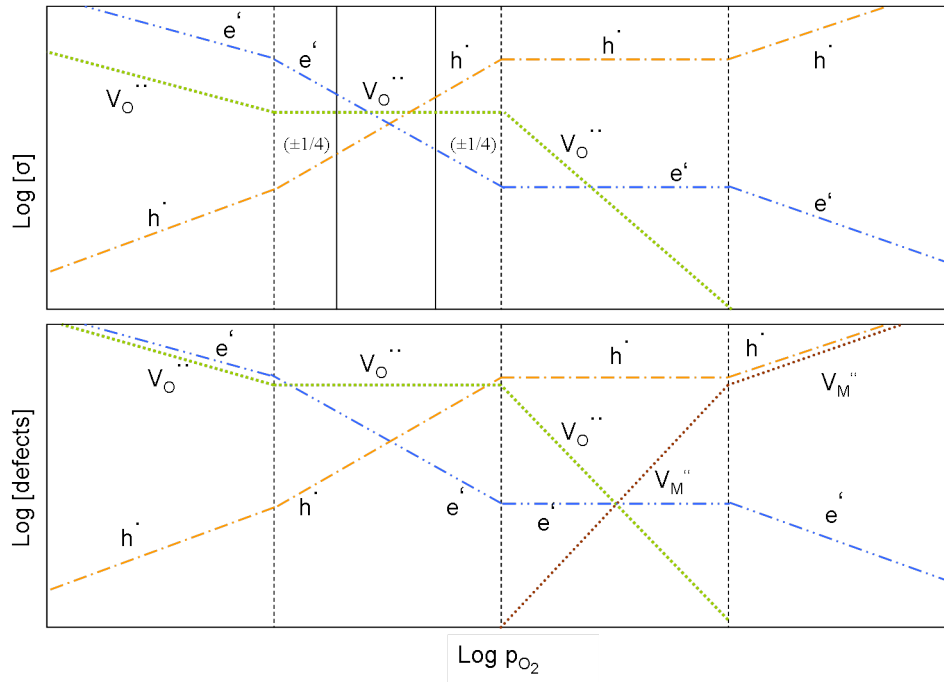


Figure 2.3

Fig. 2.3: The top diagram shows the conductivity characteristics against partial pressure, the Brouwer diagram for the acceptor doped case is illustrated beneath.^[70]

2.2 Theory of space charge layers and the mesoscopic effect

By means of measurements on single crystalline and bicrystalline SrTiO_3 a fundamental understanding of the electrical properties, which are affected by concentration and mobility of charge carriers, has been obtained. In polycrystalline material a modified micro-structure, i.e. the formation of grain boundaries has to be also considered. A closer observation shows that –from an electrical point of view– grain boundaries can be divided into a grain boundary core and adjacent space charge regions. Based on the changes in the crystal structure, a change in the standard chemical potential has to be taken into account in the core region. Browning *et. al.*^[55] sees the origin for the generally positive boundary charge in undoped or acceptor-doped SrTiO_3 , in the incomplete octahedra structure in this regions. Thus an immobile fraction of oxygen vacancies is located in the grain boundary plane. As a consequence, the charge carrier distribution deviates from the bulk value due to the separation of charge and leads to an oxygen vacancy depleted zone (space charge zone) adjacent to the grain boundary core to satisfy electroneutrality. By as-

suming a diluted case for the defects under consideration, we can combine the Maxwell-Boltzmann distribution Eq. 2.15 with the Poisson equation Eq. 2.16,

$$\zeta_j = \frac{c_j(x)}{c_{j,\infty}} = \exp\left(\frac{z_j e}{k_B T} (\Phi(x) - \Phi_\infty)\right) \quad (2.15)$$

$$\frac{\partial^2 \Phi(x)}{\partial(x)^2} = -\frac{Q(x)}{\epsilon_r \epsilon_0} = -\frac{1}{\epsilon_r \epsilon_0} \sum_j (z_j e c_j(x)) \quad (2.16)$$

and obtain the following differential equation Eq. 2.17 (Poisson-Boltzmann),

$$\frac{\partial^2 (\Phi - \Phi_\infty)}{\partial(x)^2} = -\frac{e}{\epsilon} \sum_j c_{j,\infty} z_j \exp\left(-z_j e \frac{(\Phi - \Phi_\infty)}{k_B T}\right) \quad (2.17)$$

where Φ is the electrostatic potential, $\epsilon = \epsilon_r \epsilon_0$ is the dielectric constant, z_j is the charge of the defect, $Q(x)$ denotes the charge density, $c_j(x)$ and $c_{j,\infty}$ are the defect concentrations in the space charge layer and the bulk and e , k_B and T have their usual meanings.

Going a step further and analyzing the number of mobile majority charge carriers we can distinguish between a high temperature and a low temperature regime. At high temperatures with slightly mobile cations, or in the so-called Gouy-Chapman case, two mobile charge carriers of opposite signs have to be considered. In SrTiO_3 these two defects are the singly ionized Fe_{Ti}' and $\text{V}_{\text{O}}^{\bullet\bullet}$. The depletion of oxygen vacancies in this region is much more pronounced due to the double charge. Consequently, the acceptor dopant determines the defect concentration in this region of the material and thus defines the charge density in the space charge zone. The Poisson equation (Eq. 2.16) therefore changes to Eq. 2.18.

Gouy-Chapman
case

$$\frac{\partial^2 \Phi(x)}{\partial(x)^2} = -\frac{Q(x)}{\epsilon_r \epsilon_0} = -\frac{e}{\epsilon_r \epsilon_0} \left[-c_{\text{Fe},\infty} \exp\left(\frac{e(\Phi(x) - \Phi_\infty)}{k_B T}\right) + 2c_{\text{V}_{\text{O}}^{\bullet\bullet},\infty} \exp\left(\frac{-2e(\Phi(x) - \Phi_\infty)}{k_B T}\right) \right] \quad (2.18)$$

In order to get the charge carrier concentration for the defect j in the corresponding space charge region, we have to define the Debye length λ (Eq. 2.19).

$$\lambda = \sqrt{\frac{\epsilon k_B T}{2z^2 e^2 c_\infty}} \quad (2.19) \quad \text{Debye length}$$

By taking Eq. 2.15 into account we achieve the solution for the Gouy-Chapman case (Eq. 2.20).

$$\zeta_j(x) = \left(\frac{1 + \vartheta_{\pm} \cdot \exp\left(\frac{-x}{\lambda}\right)}{1 - \vartheta_{\pm} \cdot \exp\left(\frac{-x}{\lambda}\right)} \right)^2 \quad (2.20)$$

with

$$\vartheta_{\pm} = \frac{\sqrt{\zeta_{\pm}} - 1}{\sqrt{\zeta_{\pm}} + 1} \quad (2.21)$$

Here, the same absolute charge numbers (z) are assumed for both charge carriers, for Fe-doped SrTiO₃ slight deviations of Eq. 2.20 result. For higher temperatures, which are reached for SrTiO₃ at preparation conditions, the charge carrier distribution depends on the concentration of the charge carrier in the bulk and at $x=0$, as well as on the dielectric constant ϵ , cf. Eq. 2.20. The Debye length is reflecting the dimension of the space charge layer, because at $x \cong 2\lambda$ the charge carrier concentration is already close to bulk concentration.^[71]

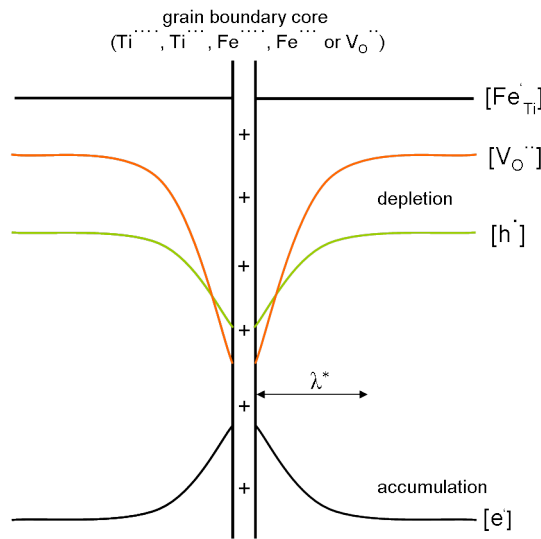


Figure 2.4

Fig. 2.4: Charge carrier distribution in the Mott Schottky case.

The second possibility how the charge carriers can be distributed in the space charge zone is described by the Mott-Schottky model. In that case only one of the majority charge carriers is mobile and, therefore, depleted or accumulated at the grain boundary. The concentration of the second charge carrier, which is immobile as a result of the lowered temperature can be assumed constant up to the surface. This means that this charge carrier is not in electrochemical equilibrium. However, due to the strong depletion of oxygen vacancies the charge density is again determined by the –now immobile– acceptor dopant.

Mott-Schottky
case

For SrTiO₃ at T<900°C the Mott-Schottky case can safely be assumed and since the experiments in the present thesis were conducted between 325°C and 700°C this model is assumed to be valid. A schematic picture of the Mott-Schottky-type charge carrier distribution in the vicinity of the grain boundary is shown in Fig. 2.4.^[1,29,49,57,72-74]

The simplified Poisson equation is shown in Eq. 2.22, where $c_{j,\infty}$ is the concentration of Fe'_{Ti} in the bulk (i.e. far away from the grain boundary region, $c_{Fe'_{Ti},\infty}$).

$$\frac{\partial^2 \Phi(x)}{\partial(x)^2} = -\frac{Q(x)}{\epsilon_r \epsilon_0} = -\frac{ze c_{j,\infty}}{\epsilon_r \epsilon_0} \quad (2.22)$$

This leads to:^[74]

$$\phi(x) - \phi_\infty = -\frac{ze c_{j,\infty}}{\epsilon_r \epsilon_0} (x - \lambda^*)^2 \quad (2.23)$$

The difference between the high and the low temperature case is that, in contrast to the Gouy-Chapman situation, λ^* depends on the potential difference $(\phi(x) - \phi_\infty)$ (Eq. 2.23). The Debye length λ and the "effective" Debye length λ^* have the relation shown in Eq. 2.24.

$$\lambda^* = \lambda \sqrt{\frac{4z_+ e}{\epsilon k_B T} (\Phi_0 - \Phi_\infty)} \quad (2.24) \quad \text{effective Debye length}$$

Taking again Eq. 2.16 and $z_+ = z_- = z = 2$ (two equivalently charged carriers, e.g. Ni- instead of Fe-doping), we obtain the oxygen vacancy concentration in the space charge layer (Eq. 2.25).

$$\zeta_j(x) = -\exp\left(\frac{x - \lambda^*}{2\lambda}\right)^2 \quad (2.25)$$

It is worth noting that this derivation is also valid for the double Schottky barrier situation of a grain boundary. Without external DC voltage these two space charge layers are symmetrical. But if a DC bias is applied the symmetric space charge zone is altered into an asymmetrical state. On the one side of the grain boundary the space charge layer becomes extended whereas on the other side a reduction of the layer thickness can be observed. Fig. 2.5 shows the change in the oxygen vacancy concentration gradient occurring during applied DC voltage. Referring to literature, the work of Denk *et. al.*^[29] has to be mentioned in this context. They conducted impedance spectroscopy measurements on SrTiO₃ bicrystals with defined grain boundaries under DC

SCL under applied DC voltage

bias and observed a bias dependence only for the grain boundary part in the impedance spectra, as shown in Fig. 2.6. The bulk part at higher frequencies was unperturbed by the applied voltage in all cases. Similar considerations are also valid for dislocations and some special grain boundaries can even be treated as a sequence of dislocations.^[75]

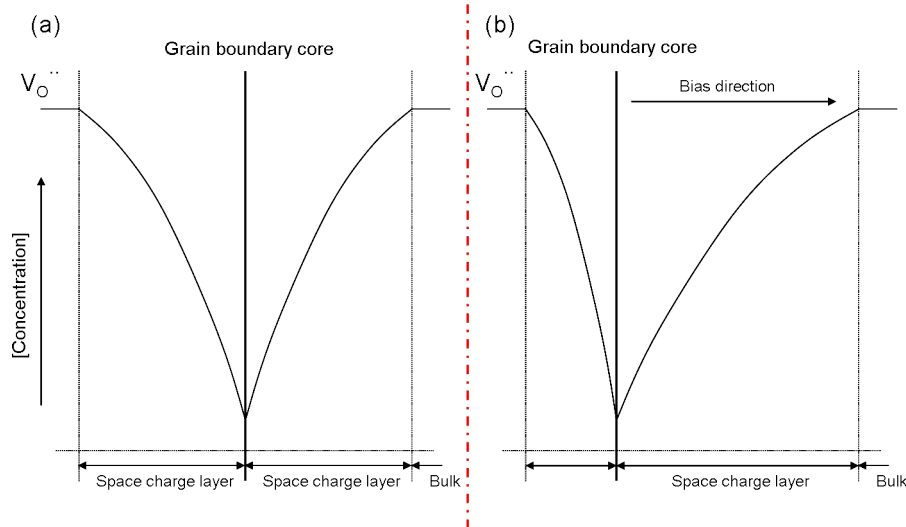


Figure 2.5

Fig. 2.5: A sketch of the oxygen vacancy concentration without bias is shown in (a), compared with the situation under applied DC bias (b).^[72]

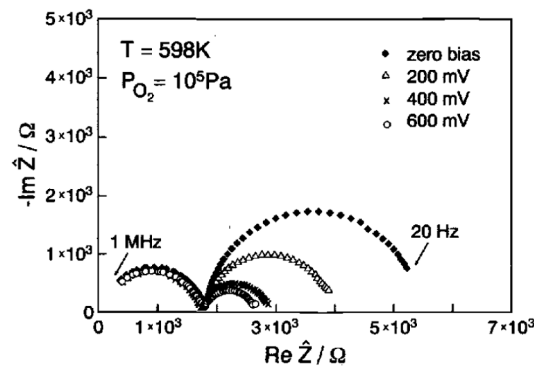


Figure 2.6

Fig. 2.6: Behavior of a bicrystal SrTiO_3 sample under an applied bias voltage, with a clear dependence of the grain boundaries on bias.^[29]

Another question is, how the influence of grain boundaries and dislocations changes when the grain size decreases into the nanometer range (i.e. into the range of the Debye-length or below). Investigations on different materials, e.g. nanocrystalline CeO_2 or YSZ show that the variations in the electrochemical behavior are not trivial to explain. Various experiments on these materials suggested an increase in conductivity at grain boundaries in comparison to polycrystalline samples. All proposed causes for this behavior observed in

those materials are dealing with effects that do not consider a true grain size effect.^[6,76]

In SrTiO₃ the most accepted approach to describe nano-scaled conditions, therefore involves a true grain size effect, namely the overlapping of space charge layers.^[21,77,78] This situation is not necessarily constricted to bulk material with grains in the nm-range, but can be also used to describe the situation in thin layers. For thin layers the increased density of grain boundaries or dislocations as well as the difference in the volume to surface ratio compared to bulk samples may be relevant. The previously introduced Debye length (or effective Debye length) can be used as the relevant parameter indicating overlapping or non-overlapping space charge zones. Fig. 2.7 shows that in the limit of small grains and thin layers the local electroneutrality condition is nowhere satisfied.

As already shortly mentioned above, impedance spectroscopy can be employed to separate grain and grain boundary contributions to the total conductivity of STO. As long as the grain size L is larger than 4λ the sample still shows two clearly separated semicircles in impedance measurements with high and low frequency arcs representing grain and grain boundary, respectively. A reduction of the grain size leads to the point where the L value reaches 4λ (or $2\lambda^*$) or becomes even smaller. This is the situation when the entire grain is charged and the transport properties are governed solely by the grain boundary properties.

Mesoscopic ionic conductivity effect

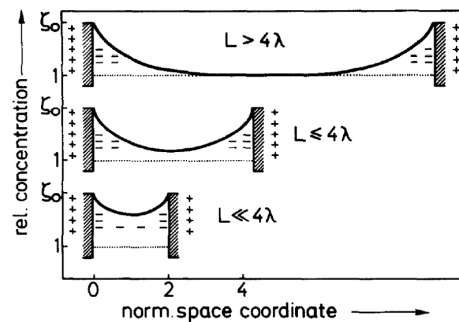


Figure 2.7

Fig. 2.7: Schematic picture of the space charge overlapping effect with decreasing grain size.^[20]

Balaya *et. al.*^[77,78] reported that for nanocrystalline SrTiO₃ material with a Fe-doping level of around 100 ppm and a grain size of around 80 nm the bulk part completely vanishes. The residual semicircle has to be attributed to

the grain boundary response. Another highly interesting discovery concerning nanocrystalline SrTiO_3 has been made by Lupetin *et. al.*^[52]. In this work, investigations under changing oxygen partial pressures were compared with results for coarsened samples. The results are shown in Fig. 2.8 and indicate obvious changes in the n-, p- as well as in the ionically conducting regime. The observed results can also be explained in terms of adjacent space charge layers and their overlapping in the nm-range. Regarding thin films of SrTiO_3 , space

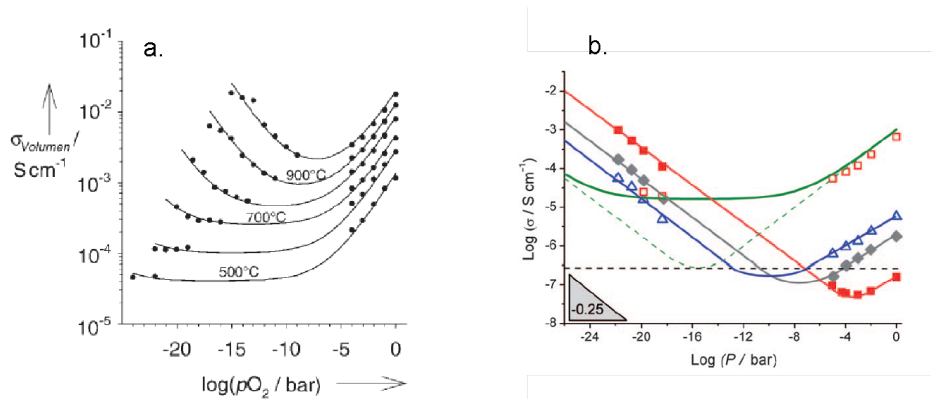


Figure 2.8

Fig. 2.8: Shift of the conductivity in the oxygen partial pressure range for single crystal bulk STO^[16] (a) compared with nanocrystalline SrTiO_3 (b).^[52]

charges influencing at least parts of the investigated material have also been used to explain the observed results. Ohly *et. al.*^[61–63] suggested in his work, that space charge layers can also be located at surfaces of thin films and at the film|substrate interface. By reducing the thickness of the films an overlapping of the surface and interface space charge layers is supposed which could lead to a shift in the dependence of conductivity on oxygen partial pressure.

2.3 Polarization processes in SrTiO_3 – Resistance degradation, Wagner-Hebb polarization and resistive switching

2.3.1 Resistance degradation

In single crystalline as well as polycrystalline perovskite-type titanates, resistance degradation under an applied DC field is a well known phenomenon. An accepted explanation approach is based on the field driven motion of oxygen vacancies and their (partial) blocking at electrodes. This leads to a redistribu-

tion of oxygen vacancies upon DC field load and modified electrical properties of the sample. This is further detailed in Sec. 2.26. Hence, the concentration of oxygen vacancies greatly influences the degradation process and its extent.^[36–38] Focusing again on SrTiO₃, the oxygen vacancy concentration in undoped and acceptor doped material is significantly higher than in donor doped SrTiO₃. According to the defect chemical situation illustrated in Chapter 2.1, acceptor doping is mainly compensated by the formation of oxygen vacancies. As a consequence, donor doping leads to a stabilizing effect against degradation. Resistance degradation does not occur immediately after applying bias voltage. Rather oxygen vacancies need some time to move in a DC field and this causes conductivity changes. Increasing the DC voltage causes a faster motion of $V_{\text{O}}^{\bullet\bullet}$.

Resistance degradation

Waser *et. al.*^[36,37], Baiatu *et. al.*^[38] and Rodewald *et. al.*^[33,34,67] quantitatively analyzed the resistance degradation phenomena by their theoretical and experimental work. The highly resolved impedance measurements done by Rodewald confirmed the theory behind the field-induced electro-coloration (and resistance degradation) in Fe-doped SrTiO₃. As it can be seen in Fig. 2.9, the applied voltage leads to a redistribution of charge carriers in the material and a spatially varying conductivity profile in the material becomes observable. Consequently it is quite reasonable that the demixing of the charge carriers results in the formation of a pn-junction within the material.

Especially in the case of Fe-doped SrTiO₃, the internal redox-reaction of the dopant may not be neglected. On the one hand, it provides the opportunity to visualize the electro-migration of the oxygen vacancies due to the differences in color of Fe³⁺ and Fe⁴⁺ states. On the other hand, redox-reactions cause a complication in terms of defect chemical considerations (compared to Brouwer diagrams for the undoped (Fig. 2.2) and acceptor doped case (Fig. 2.3)). Furthermore, resistance degradation is also different for single crystalline and polycrystalline titanates. As discussed earlier, grain boundaries have always a great influence on the transport properties of the investigated material, and this also affects the degradation behavior. Simulations done by Waser^[36] showed an enhanced electric field located in the vicinity of grain boundaries shortly after applying a DC voltage. This "barrier" for oxygen vacancy migra-

tion is assumed to be the rate limiting step of resistance degradation in SrTiO₃ polycrystalline ceramics.

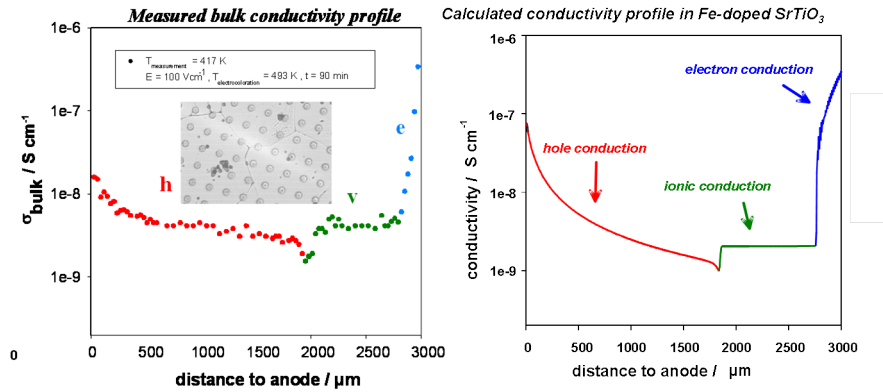


Figure 2.9

Fig. 2.9: Results for locally resolved conductivity measurements after exposing SrTiO₃ single crystals to a high DC field, compared with simulated data reported by Rodewald *et. al.* [33,34,67,68,79]

2.3.2 Wagner-Hebb polarization

A bias voltage applied to SrTiO₃ can not only be the reason for degradation phenomena in the material, it also can be used to separate partial ionic and electronic conductivity. This approach was firstly published by Hebb^[80] and more or less simultaneous by Wagner^[81]. The corresponding sample set-up, also realized for our Fe-doped SrTiO₃ thin films, is shown in Fig. 2.10(a). SrTiO₃ is sandwiched between an oxygen blocking electrode (in our case Nb-SrTiO₃) and a completely or at least partially reversible counter electrode (here (La,Sr)CoO_{3-δ} (LSC)). An additional sealing of the free STO surface is not necessary due to the slow surface exchange reaction as long as the considered temperature range is low enough.^[72] Furthermore, this exchange is irrelevant for thin films due to geometrical reasons, cf. aspect ratio.

In the first moment when voltage is applied to the cell, the vacancy concentration is still homogeneously distributed throughout the sample. The total current consists of an ionic and an electronic contribution ($J=J_e+J_i$). With proceeding time a demixing occurs, which is induced by the migration of effectively positive charged oxygen vacancies towards the negative cathode (see Fig. 2.10(b)). As a consequence of the blocking character of the cathode, the oxygen vacancies pile up and are compensated by electrons released from the adjacent electrode. On the side of the anode, oxygen vacancies will be

Wagner-Hebb polarization

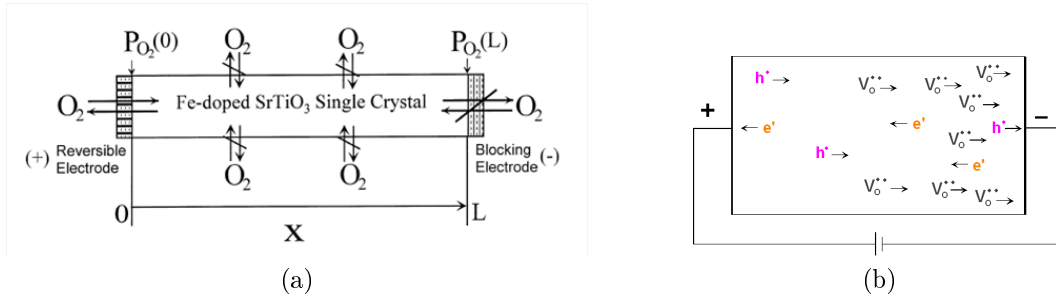


Figure 2.10

Fig. 2.10: (a) Picture of a polarization cell with STO sandwiched between a blocking electrode and a reversible electrode, with the advantage of a self-sealed free STO surface^[48], (b) Schematic picture of the occurring electromigration process of oxygen vacancies due to field stress.

generated according to Eq. 2.13. In the course of the experiment, growing of the n-conducting regime can be observed starting from the cathode and moving into the material. Alternatively we can describe the situation by a change in the chemical potential of the oxygen at the cathode side. This results in a vacancy concentration gradient, which has to be compensated by electronic charge carriers. Assuming the anode to be at least partly reversible, the chemical potential is pinned at this electrode. The steady state is then characterized by the vanishing of the ionic current density. This experiment is obviously strongly related to the resistance degradation discussed above.

In this Wagner-Hebb-type experiment one electrode (the top electrode in the thin film case) serves as "open road" for release and incorporation of oxygen. The O₂ reduction/O²⁻ oxidation reaction at the gas/solid interface is commonly known to be a thermally activated process and, therefore, a decrease in temperature gradually closes this way for oxygen exchange. Assuming this reaction path to be fully blocked the amount of oxygen vacancies in the material stays more or less constant ($\int [V_{O}^{\bullet\bullet}] dx$ independent of t, T and p_{O₂}). For the polarization experiment this means that the point where the vacancy concentration stays invariant switches from position x=0 (Fig. 2.11(a)) into the sample. For small perturbations we obtain a symmetric case (to x=L/2) as it is shown in Fig. 2.11(b).

In the "ideal" Wagner-Hebb case a mixed ionic and electronic conductor is sandwiched between a blocking and a reversible electrode. Upon polarization

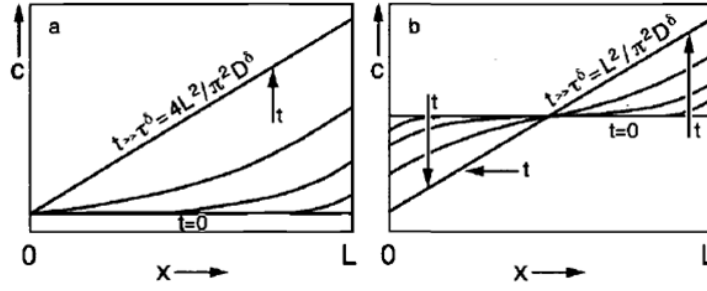


Figure 2.11

Fig. 2.11: Concentration gradient of oxygen vacancies build up during a polarization experiment. In (a) the situation with one blocking electrode and in (b) with two blocking electrodes is illustrated.^[2]

by a DC voltage U the following equation (Eq. 2.26) can be assumed to describe the current-voltage relationship (Wagner-Hebb polarization).^[2,81]

$$i_{eon} = i_n + i_p = \quad (2.26)$$

$$\frac{k_B T}{\alpha e L} \left\{ \sigma_n(0) \left[\exp\left(\frac{\alpha e U}{k_B T}\right) - 1 \right] + \sigma_p(0) \left[1 - \exp\left(-\frac{\alpha e U}{k_B T}\right) \right] \right\}$$

Therein α is defined as $\alpha = \nu z |N|$, with N describing the characteristic exponent in $\sigma_p \propto \sigma_n^{-1} \propto p_{O_2}^{|N|}$, ν is the molecularity of the gaseous component (oxygen in the oxide case) and z is the number of electrons needed to ionize one gas atom to the bulk state. Oxides exhibit $\alpha = 4N$ and when $N=0.25$ an α -value of 1 is expected. For larger positive or negative voltages either the first or the second term in Eq. 2.26 can be approximated by the prefactor $\sigma_{n/p}(0)$ which denotes the electron or hole conductivity in equilibrium. The other term increases exponentially. This is illustrated in Fig. 2.12.

It is clearly visible that for predominant hole conduction in equilibrium the inflection point is shifted to positive bias values. Please note that here the voltage is measured versus the reversible electrode while in this thesis it is defined versus the substrate of the thin film (Nb-SrTiO₃).

2.3.3 Resistive switching

A third interesting effect which can occur by applying bias voltage to mixed ionic and electronic conducting materials, became known as resistive switching phenomenon. This effect can be potentially applied for non-volatile data storage and it is therefore intensively investigated. In this section a short overview is given with the focus on investigations performed on SrTiO₃. In general, a

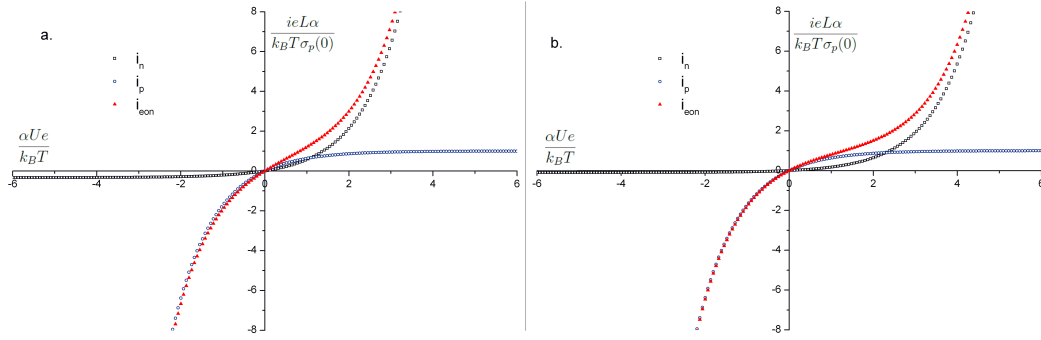


Figure 2.12

Fig. 2.12: Simulation of the Wagner-Hebb case ($\alpha = 1$) for i_n , i_p as well as for i_{eon} with $\sigma_p(0) = 3\sigma_n(0)$ (depicted in a) and $\sigma_p(0) = 10\sigma_n(0)$ (shown in b).

resistive switching device is assembled by an insulating material sandwiched between two electron conductors. We focus on such metal-insulator-metal (MIM) structures where chemical effects are discussed to be responsible for the resistive switching behavior.

- The **electrochemical metallization memory (ECM)** is based on metal deposition and subsequent dissolution to perform resistive switching. The active electrode mainly consists of Ag or Cu. The inert counter electrode (Pt, W, Ir) is separated from the active electrode by an M^{z+} ion conducting electrolyte. As shown in Fig. 2.13, the whole process can be divided into 4 states. Starting from initial state D a sufficiently positive bias voltage leads to an anodic dissolution ($M \rightarrow M^{z+} + ze^-$). Because of the applied electrical field, a subsequent migration of the ions in direction to the inert cathode takes place. At the cathode, the reduction reaction occurs leading to deposition and growth of a metal filament (state A). In this stage of the process, the sample is still in the so-called OFF state or high resistance state (cf. state D). The ON state is not reached until the filament reaches the active electrode, which causes a short circuit of the cell as consequence (state B). By applying a voltage with opposite polarity, the low resistance state is destructed because of the dissolution of the filament and the loss of the metallic contact between the two electrodes (state C).
- The other important type of resistive switching phenomenon is based on the **valence change mechanism (VCM)**. This mechanism is also found in $SrTiO_3$ and thus is especially interesting for the present work. In the case of VCM's the same migration processes as described above

Electrochemical metallization memory/ECM

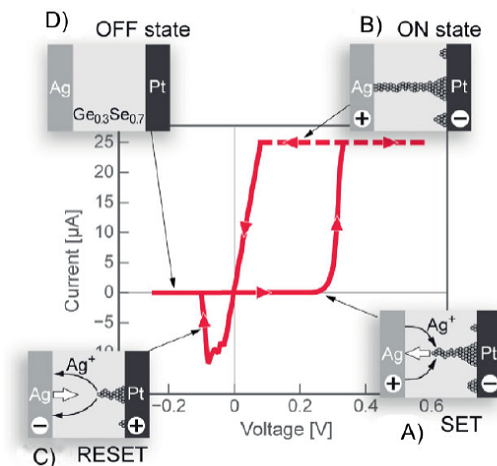


Figure 2.13

Fig. 2.13: Process steps of forming a conductive Ag-filament (ON state) in one bias direction and after switching polarization reaching again the OFF state by dissolving the filament.^[39]

for resistance degradation (Section 2.3.1) and Wagner-Hebb polarization (Section 2.26) are responsible for the typical characteristics. In particular, for SrTiO₃ it is quite likely that again the electrochemical migration of $V_{\text{O}}^{\bullet\bullet}$ is responsible for the switching. To gain reproducible changes in resistance states, an initial electro-forming step similar to ECM's is also required for materials based on valence change reactions.

Valence change
memory/VCM

The localization of the relevant resistive changes resulting from electrical stimulation are still under discussion. Szot *et. al.*^[40,41] reported an enhanced conductivity due to fast dislocations in SrTiO₃, indicating a filamentary switching behavior. Their investigations on Fe-doped SrTiO₃ by conductive-atomic force microscopy (C-AFM) showed strong inhomogeneities of electrical conductivity after etching with diluted HCl. They discussed dislocations to be responsible for this behavior (see Fig. 2.14). TEM investigations as well as simulations and calculations of the electronic structure of such dislocations were performed to find the origin for the high conductivity in dislocations.^[40,82–84]

All these investigations agree in terms of the changed defect chemical situation in and near a dislocation. In detail, a high degree of self-assembly of oxygen vacancies can be found. This highly localized oxygen deficiency causes a valence change of the adjacent Ti-atoms. Because the increased concentration of oxygen vacancies in the core of dislocations reacts much faster on applied voltage (or changed oxygen partial pressure) than the

surrounding bulk, the whole switching mechanism is located at these specific filaments. Besides studies on defect motion, the density of dislocations was intensively investigated. For bulk samples the highest density of dislocations was found in the near surface region. For single crystalline material the existence of such a disruption of the perfect lattice is not surprising due to the necessary grinding and cutting steps required in the preparation procedure. Investigations of SrTiO₃ thin films on LaAlO₃ done by Qin *et. al.*^[60] demonstrated the high importance of dislocations also in thin films.

Filamentary resistive switching

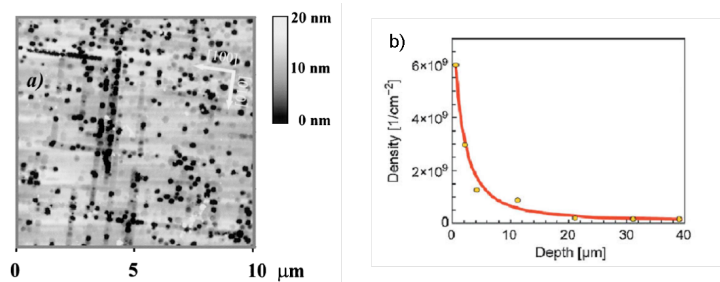


Figure 2.14

Fig. 2.14: In (a) the chemically etched surface of a (100) SrTiO₃ sample is shown^[85]; the dark dots indicate dislocations. In (b) the spatial distribution of dislocations in a bulk SrTiO₃ sample is illustrated.^[86]

However, filamentary resistive switching is only one of the observed mechanisms. Sawa *et. al.*^[87] reported the existence of area related resistive switching. In this case, the resistive switching initiates at the interface of the oxide with one of the metal electrodes. Further details depend on the investigated material.

Studies on Nb-doped SrTiO₃ were published reporting a dependence of resistive switching behavior on the active area. There, the contact resistance at the metal/oxide interface changes due to applied DC bias. This was also found by Baikalov *et. al.*^[88] for the Ag/Pr_{0.7}Ca_{0.3}MnO₃/YBa₂Cu₃O₇ system and they found that the measured resistance correlates with the Schottky barrier located at such an interface. An increase or decrease of the oxygen vacancy concentration, e.g. caused by field induced defect motion, is directly correlated with the width of the vacancy depletion layer (= Schottky barrier) and further with the investigated contact resistance.

Area related resistive switching

This theoretical overview should emphasize the importance of defect motion and migration in SrTiO₃. Furthermore, it is interesting to see how

far results and findings obtained on bulk material are at least partly transferable to thin layers. The investigation of SrTiO₃ thin layers is thus a promising way, to achieve more information on the defect chemical processes induced by an applied DC bias, and how those processes are influenced by one or two dimensional defects in thin films.

Experimental

3.1 Thin layer preparation by pulsed laser deposition (PLD)

All investigated SrTiO₃ films were prepared by pulsed laser deposition (PLD). As target a polycrystalline pellet of 0.4mol% Fe-doped SrTiO₃ was used. The target material was made by means of the classical solid-state reaction. As starting materials Fe(NO₃)₂·9H₂O, SrCO₃ and TiO₂ were used. The powder pellet was prepared by cold isostatic pressing. Afterwards the green body was sintered at 1400°C under ambient atmosphere for several hours.

The experimental deposition set-up as it is shown in Fig. 3.1 consists of two main components, the laser source and the vacuum chamber. For the preparation of thin metal oxide layers on various substrates an accurate heating stage, a pump system as well as a controlled gas inlet are necessary to achieve stable conditions and thus defined and reproducible thin films. Inside the vacuum chamber, the heating stage and the rotating target are aligned to the same axis with the option of varying the distance between target and substrate. The inherent laser beam, which is provided by a KrF excimer laser with a wavelength of 428 nm (Coherent Lambda Physics, Germany), is focused on the target. With a pulse energy of 400 mJ/pulse and a pulse frequency of 5 Hz the energy density achieved on the target is around 2.2 J/cm²/pulse. All samples have been prepared at 650°C and at an oxygen pressure of 0.15 mbar. During deposition the temperature was measured with a pyrometer (Heitronics, Germany) and was recorded by LabView. Differences in the layer thickness

were achieved by changing the deposition time. These times varied between 10 minutes and 50 minutes and lead to layer thicknesses between 60 and 420 nm. The subsequent cooling of the samples was performed under continuous oxygen flow. For the electrochemical experiments thin films were deposited on Nb-doped SrTiO₃ and mostly used as prepared in the subsequent electrical studies. Some films were additionally annealed at 920°C for 2 hours prior to the electrochemical characterization.

For the structural characterization, SrTiO₃ was also grown on LaAlO₃ and Al₂O₃. For the deposition of (La_{0.6}Sr_{0.4})CoO_{3-δ} (LSC), which was used as micro-electrode material, the temperature was lowered to 450°C and the pressure to 0.04 mbar. This is known to lead to LSC electrodes with very fast oxygen exchange kinetics.^[89] In the case of LSC the deposition time of 20 minutes and the resulting electrode thickness of 150-180 nm were kept constant for all samples.

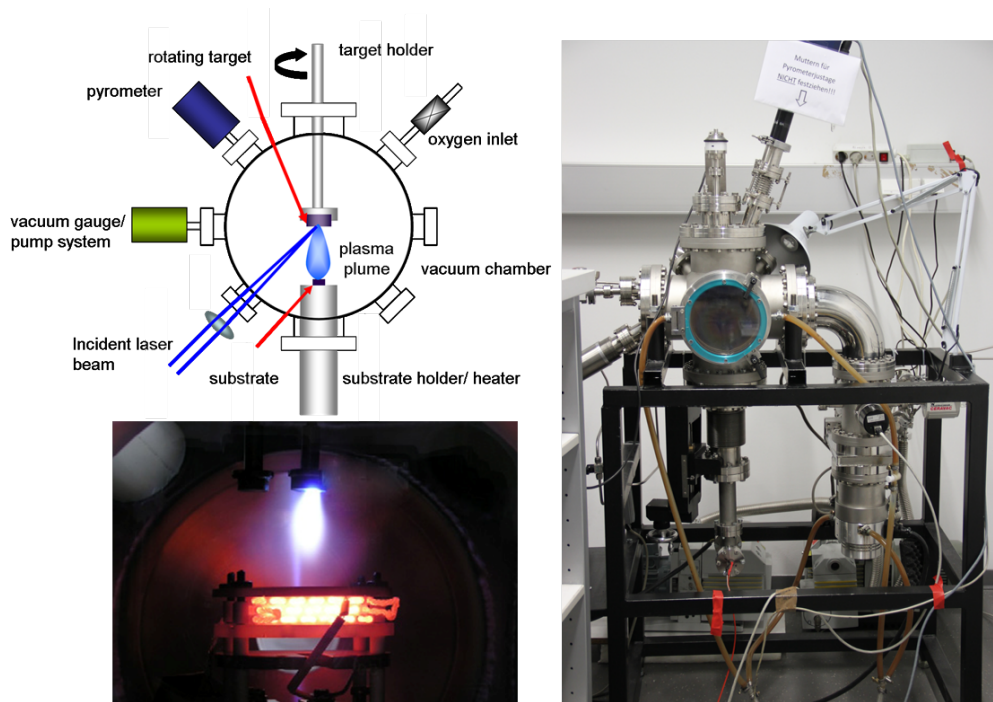


Figure 3.1

Fig. 3.1: Schematic picture of the pulsed laser deposition set-up and photos of the entire set-up (without laser) and the plasma plume during deposition.

3.2 Microelectrode preparation by photolithography

LSC was used as electrode material on top of the Fe-doped SrTiO₃. For the micro-structuring of a LSC layer, a thin film of photoresist (Microresist Technology, Germany) was spin coated. After a heating step at 100°C for 2 minutes, a photomask (Rose, Germany) with the appropriate structure was positioned on top of the sample. Via the exposure (40 s) of UV light by using an UV lamp from USHIO Japan (USHIO 350DP Hg UV Lamp) the shielded parts of the sample were excluded from the polymerization process and therefore could be removed in a subsequent developing step. After an etching step with diluted HCl, where the excess LSC was removed, the photoresist was dissolved in acetone. In Fig. 3.2 the preparation steps are sketched. For the investigation of the electrode material impact, also a few samples with metallic electrodes (Pt or Cr/Au) were made. These micro-electrodes were prepared using the lift-off method. A BAL-TEC Coating System (BAL-TEC, Germany) was used to sputter the metal layer with a thickness of around 120 nm on top of the SrTiO₃ thin film.

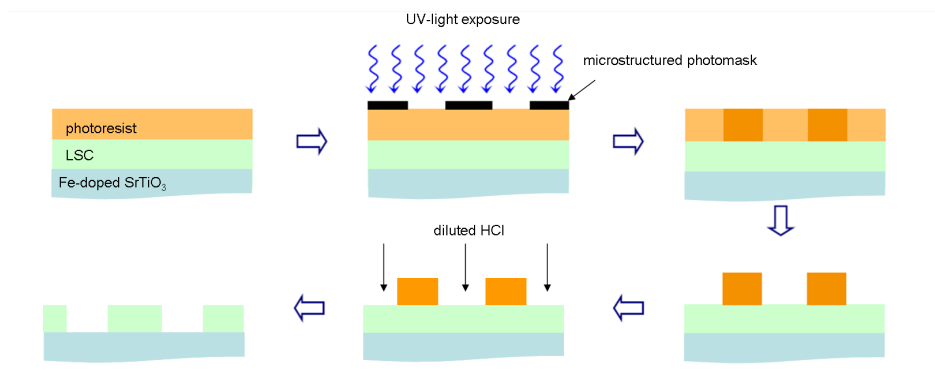


Figure 3.2

Fig. 3.2: Spin coating of the photoresist on top of the LSC and subsequent heating → exposure to UV light leads to a polymerization of the unprotected photoresist → removal of the non-exposed photoresist → etching away the uncoated LSC areas with diluted HCl → removing the protective photoresist layer with acetone.

3.3 Electrochemical measurements

SrTiO₃ thin films were analyzed by alternating current (AC) and DC measurements, performed in two different experimental set-ups. On the one hand, samples were measured in a micro-contact set-up (Fig. 3.3) with the sample being positioned on a heating stage. This setup provided advantages for the experiments especially at different partial pressures due to the possibility of rapid cooling and heating, as well as a controlled filling with different gas mixtures. As disadvantages, the limitation in automation and the inaccuracy in the temperature measurement due to the cooling effect of the used needles and the absence of a local temperature measurement should be mentioned.^[90] The temperature deviation between the data set "Micro" and the data set "Micro-Macro", was evaluated by plotting the complete conductivity data of one and the same film within one Arrhenius diagram. The Arrhenius plot of the "Micro" sample exhibits a shift of $\approx 53^\circ\text{C}$ at lower T and of $\approx 92^\circ\text{C}$ for higher T, as it is depicted in Fig. 3.4. A further difference in the magnitude of deviation also for different electrode diameters (\downarrow diameter \Rightarrow \uparrow cooling effect/temperature difference) could be observed.

Measurement set-ups, Micro and Micro-Macro

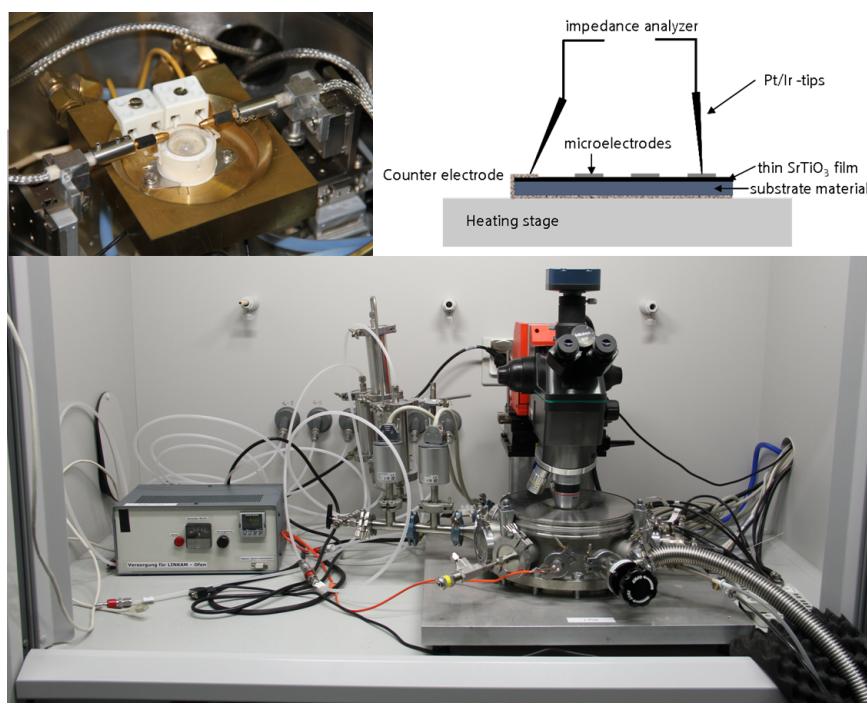


Figure 3.3

Fig. 3.3: "Micro" set-up: heating stage, entire set-up and a schematic picture of the contacted sample situation.

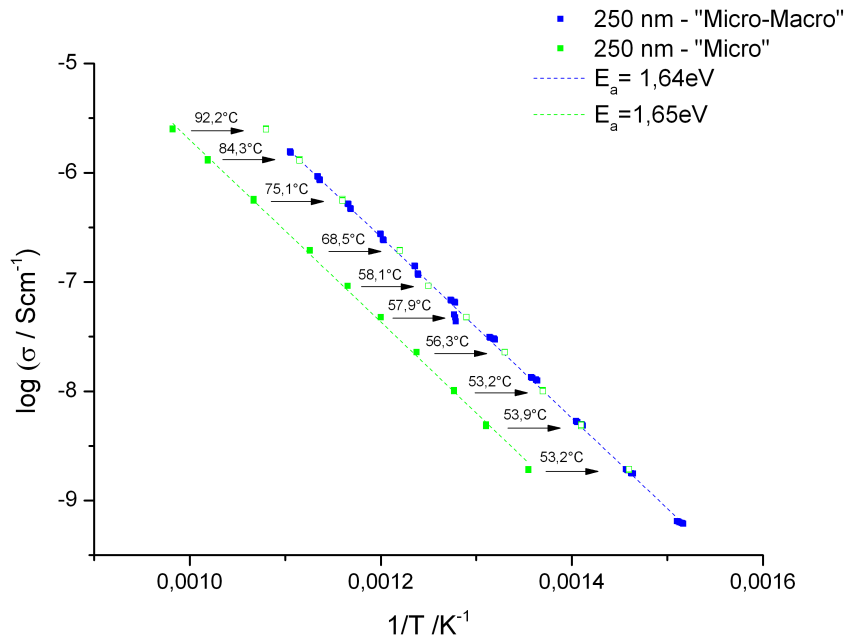


Figure 3.4

Fig. 3.4: Comparison between impedance data recorded within the "Micro" set-up and data obtained by using the "Micro-Macro" set-up for a 300 μm electrode prepared from a 180 nm LSC thin film on a 250 nm STO film, gives clear evidence of the cooling effect by the contacting needle.^[90]

To avoid the mentioned problems of the "Micro-contact" set-up, the samples were measured in the so called "Micro-Macro" set-up. This new experimental approach offers a beneficial combination of ambient heating and recording of the sample temperature. Additionally, it is still possible to contact defined microelectrodes with a flexible needle cantilever. Long cycle measurements with changing temperatures become possible, because the cantilever adjusts thermal expansion of the material and therefore the contact is kept up over the whole temperature cycle. (Fig. 3.5) In both set-ups the electrochemical characterization by impedance spectroscopy (IS) and DC was done with an Alpha analyzer and a Pot/Gal-interface from Novocontrol (Novocontrol, Germany). The AC measurements without bias were performed in a temperature range from 700°C to 400°C on electrodes with diameters of 300 μm and 200 μm . Sample characterization under bias was done in the same temperature range and on the same electrodes, with applied bias voltages between -300 and $+300$ mV. For the thin film samples an amplitude of 10 mV was used to stay within the linear range. In comparison, for the measurements on a bulk sample, an amplitude of 100 mV was applied.

Alternating
current (AC)
measurements

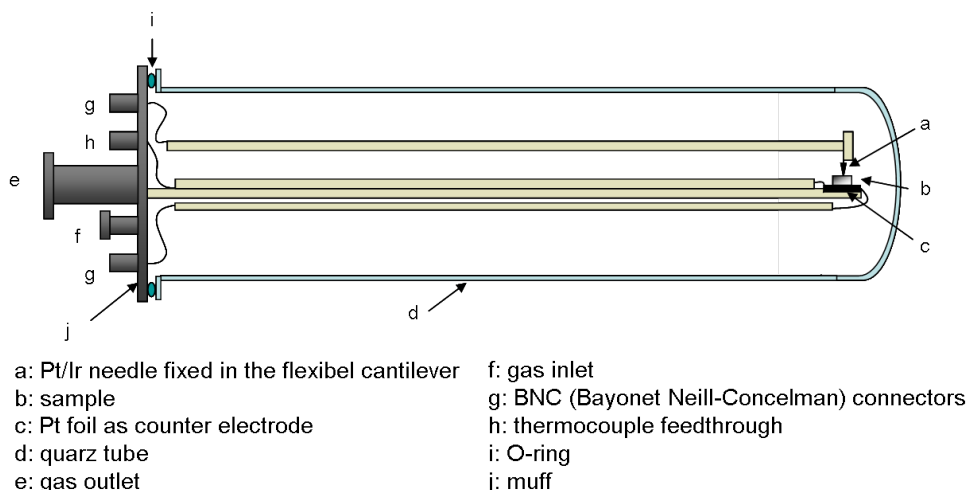


Figure 3.5

Fig. 3.5: Drawing of the "Micro-Macro" test rod.

Further experiments were performed under direct current (DC). To get a clearer picture of the current-voltage behavior of the investigated SrTiO₃ thin layers, U-I curves were detected over a voltage range of 1 V (+500 mV in the anodic range and -500 mV in the cathodic range). The sign always refers to the polarity of the top LSC electrode compared to the Nb-STO substrate. Hence, cathodic range essentially means that the oxide ion blocking bottom electrode is anodically polarized. By using the appropriate software from Novoccontrol (WinChem, Novocontrol, Germany) the time per voltage point could be adapted. This flexibility in the experimental parameters made it possible to record the behavior over a wide temperature range. At lower temperatures ($\approx 350^\circ\text{C}$) recording of an equilibrium (more precise: steady-state) U-I curve took several hours (3-12 h) due to increased equilibration time. In addition to these "slow" (steady-state) U-I curves, representing a time-independent sample state for each measured voltage point, also very fast measurements (1-5 s) have been carried out.

Direct current measurements

Measurements performed under air were repeated under changing oxygen partial pressure (157 nm and 413 nm film thickness). Those experiments were performed in the "Micro" set-up under three different atmospheres (Air, 100 % O₂, 1 % O₂) and at three different temperatures (500°C, 600°C, 700°C \Rightarrow set-temperature = temperature at the controller). For each temperature the atmosphere was changed three times to achieve sufficient data and test the reproducibility under various oxygen contents.

Measurements under different P_{O_2}

3.4 ^{18}O tracer experiments and SIMS

In addition to all the electrochemical measurements, some of the deposited SrTiO_3 thin films were also investigated by means of ^{18}O tracer exchange experiment and subsequent SIMS (Secondary Ion Mass Spectrometry) analysis. The tracer exchange was performed in a lockable test rod with an attached vacuum system. For each sample, a previous 30 min annealing step in ambient air was made. This time was considered as sufficient, due to the decreased dimension of the layer and the assumption that the chemical diffusion is much faster than the tracer diffusion in STO. ^{18}O tracer gas with a chemical purity of 97% (Campro Scientific, Germany) was used for the tracer exchange experiments performed under 450°C , 500°C and 550°C for 30 minutes. For a fast cooling of the samples, the test rod was pulled out of the furnace. During cooling, the samples were left under ^{18}O atmosphere. For the tracer exchange experiment samples with as-prepared and annealed "free" SrTiO_3 surface on Nb- SrTiO_3 were used.

To visualize ^{18}O diffusion profile in the prepared layers, a TOF.SIMS⁵ machine (ION TOF GmbH, Germany) with a pulsed Bi_3^{++} primary ion beam (25keV in CBA (collimated burst alignment) mode, 0.02 pA, $60 \times 60 \mu\text{m}^2$ raster) and a Cs^+ sputter beam (1-2 keV, 175 nA, $310 \times 310 \mu\text{m}^2$ raster and 512×512 resolution) was utilized. The used CBA mode was optimized by Kubicek^[91] and Holzlechner^[92] for oxygen isotope analysis and is characterized by an improved lateral resolution. To avoid charging effects, which can easily occur on insulating samples, a 21 eV low energy electron floodgun was used to ensure charge compensation. The distribution of the tracer was monitored by depth profiling, whereupon sputter craters from the experiment were analyzed by means of DHM (digital holographic microscopy, Lyncée, Switzerland). The evaluated thickness of the layers was then taken to normalize the tracer concentration versus sputter time plots. For the evaluation of the tracer diffusion coefficient D^* and surface exchange coefficient k^* , the corrected relative tracer concentration was plotted against layer thickness. To correct the achieved data the following equation was used:

$$c_{18\text{O}} = \frac{c_{18\text{O}}^* - c_b}{c_{\text{gas}} - c_b} \quad (3.1)$$

By this equation, we take account of the initial tracer concentration in the investigated layer prior to the exchange experiment. Symbol c_b denotes this initial "background" concentration, which is set to the value of natural abundance for ^{18}O (0,0205%) and c_{gas} is the concentration of the ambient tracer gas (97%). $c_{^{18}\text{O}}$ and $c_{^{18}\text{O}}^*$ describe the corrected relative tracer fraction, and the relative tracer fraction, respectively. The FEM (finite element modulation) calculation program Comsol (ver.4.2, Comsol Multiphysics, Sweden) was used to simulate the obtained tracer diffusion profiles in the Fe-doped SrTiO_3 layers and thus to calculate values for D^* and k^* . In these calculations also space charge effects were included.

Structural Characterization

4.1 Atomic force microscopy (AFM)

To get a clearer picture of the surface, samples which were deposited on different substrates (Al_2O_3 , LaAlO_3 , Nb-SrTiO_3 and undoped $\text{SrTiO}_3(110)(111)(100)$) were analyzed by atomic force microscopy.

The measurements were performed on a NanoScope V Multimode SPM (Bruker AXS, USA) in tapping mode under ambient conditions. In Fig. 4.1(a-c) the AFM scans for thin films on Al_2O_3 ($a=0,4785$ nm), LaAlO_3 ($a=0,3821$ nm) and Nb-SrTiO_3 ($a=0.391$ nm (Crystec, data sheet)) are shown. The thin film on Al_2O_3 reveals a columnar layer growth, occurring due to the distinct deviation in the lattice parameters between substrate and SrTiO_3 thin film. The evaluation of grain size (d_g) was performed manually by the linear intercept method using Eq. 4.1.

$$d_g = \frac{\text{Total length of reference lines}}{\text{Total number of linear intercepts}} \quad (4.1)$$

For the STO film- Al_2O_3 substrate systems, having a film thickness of 150 nm the grain size was ≈ 48 nm.

Epitaxial growth preferably happens when substrate material and layer material are the same. Besides deposition on Nb-SrTiO_3 , Fe-SrTiO_3 layers were also deposited on undoped SrTiO_3 with three different orientations. Fig. 4.1(d) illustrates the differences occurring due to the varying orientation of the substrate. The results go from a very smooth surface on the (100) substrate, which indicates more or less epitaxial growth of the film, to a columnar growth on

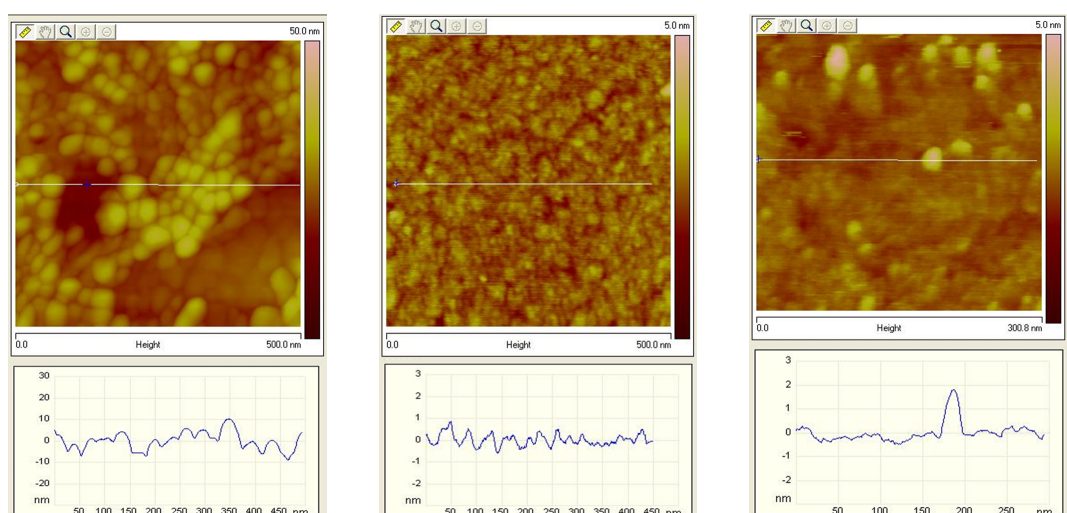
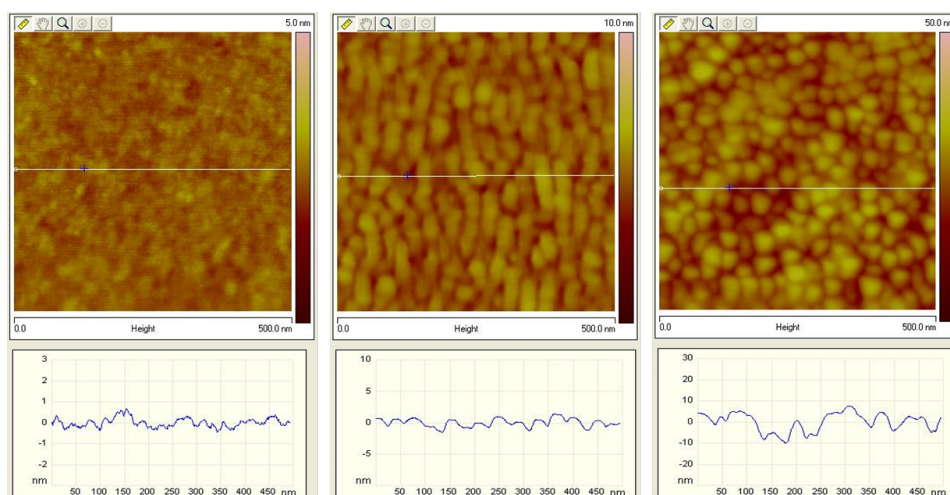


Figure 4.1

(a) STO layer on Al_2O_3 (100) with a grain size of 48 nm

(b) STO layer on LaAlO_3 (100) substrate

(c) STO layer deposited on Nb-SrTiO_3 (100) substrate



(d) AFM images of STO thin layers deposited on undoped STO with three different orientations (100), (110) and (111) (from left to right)

Fig. 4.1: AFM images for Fe-doped SrTiO_3 layers deposited on (a) Al_2O_3 , (b) LaAlO_3 and (c) Nb-SrTiO_3 , exhibiting columnar layer growth due to deviating lattice parameters for (a) and (b) and planar layer growth for (c). In (d) layers deposited on differently orientated (100, 110 and 111) undoped STO substrates are compared.

the (111) substrate. Because of the high electronic conduction of Nb-SrTiO_3 this substrate was used for all electrochemical experiments performed in this work.

4.2 Transmission electron microscopy (TEM)

Besides their high electrical conductivity which is necessary for measurements across the Fe-SrTiO₃, a further advantage of Nb-SrTiO₃ substrates is the identical lattice parameter of substrate and film. As it was mentioned in Section 2.2, the appearance of grain boundaries makes the electrochemical interpretation of experimental data more complex than for a single crystal. By the selection of Nb-SrTiO₃ substrates, layers unperturbed by grain boundaries are expected. A representative sample of Fe-STO on Nb-STO was analyzed by TEM and compared with layers on Al₂O₃ and LaAlO₃. A cross-section was prepared by focused ion beam (FIB) method to make the thin films and their structure visible. The TEM investigations were made on a FEI Tecnai F20 transmission electron microscope (FEI, USA) under guidance of Prof. Bernardi.

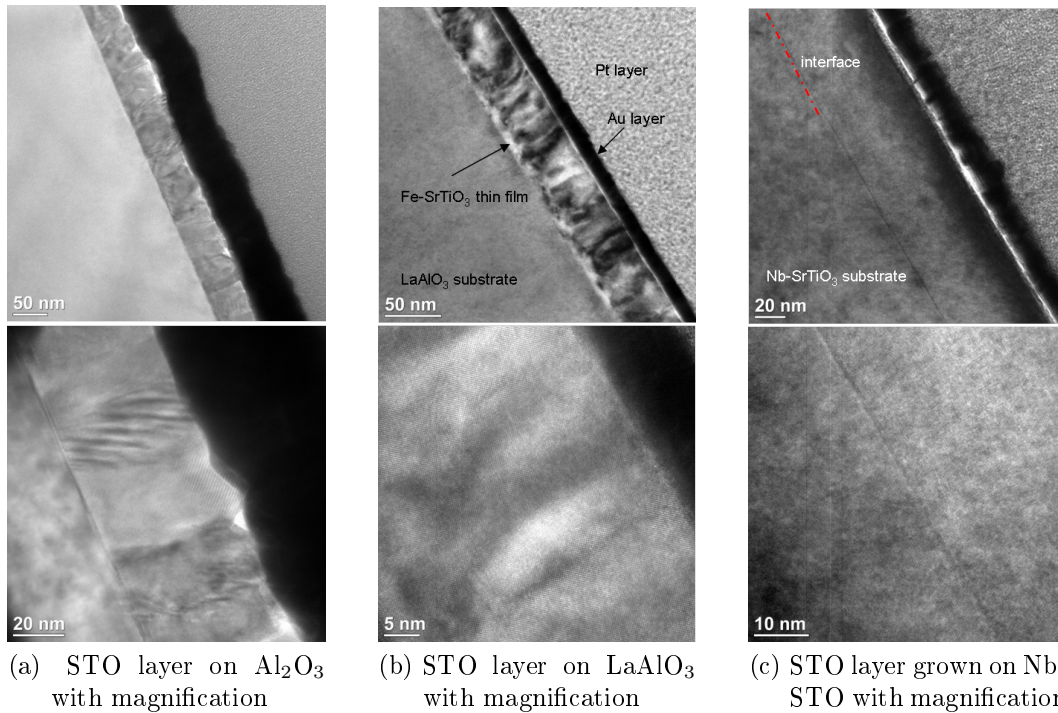


Figure 4.2

Fig. 4.2: TEM results for Fe-SrTiO₃ thin films on (a) Al₂O₃, (b) LaAlO₃ and (c) Nb-SrTiO₃

The TEM images for Fe-STO on Al₂O₃, Fe-STO on LaAlO₃ and Fe-STO on Nb-STO are depicted in Fig. 4.2 from left to the right. In the highest magnification shown, distinct deviations in layer growth can be clearly observed for the different substrate materials. Sapphire as substrate leads to the devel-

opment of grains and grain boundaries. The STO layer depicted in image (a) (Fig. 4.2) exhibits regions which show interference patterns. These phenomena are caused by the overlap of two grains. The smaller deviation in the lattice parameters of STO and LaAlO_3 prohibits the generation of grain boundaries. The darker regions, observed in image (b) indicate stress and strain, which can not be fully excluded. The assumption of Nb-STO being the preferable substrate material could be confirmed by the performed TEM investigation. The Fe-STO/Nb-STO interface is marked with a red line (image (c)) due to the fact, that other differences between substrate and layer do not exist.

Results and Discussion: Impedance Measurements With and Without Bias Voltage Performed on Thin Fe-doped SrTiO₃ Films

5.1 Impedance measurements of SrTiO₃ layers without applied bias

Several Fe-doped STO layers of different thickness were electrochemically characterized by impedance spectroscopy over a wide temperature range (400-700°C). First of all, the samples were investigated in the "Micro" set-up pictured in Fig. 3.3. Because of the described cooling effect of the contacting needle and the resulting temperature gradient on the investigated electrode, numerous experiments were also performed in the temperature optimized "Micro-Macro" set-up (see Fig. 3.5), partly for reproducing the "Micro"-experiments. To test the stability and reproducibility, more than one temperature cycle was conducted on several microelectrodes. In order to gain reasonable statistics, three to four microelectrodes were analyzed on one and the same sample. Excellent stability and reproducibility for all experiments on a given layer were achieved (see discussion in Section 5.2 and data presented in Fig. 5.6).

Typical impedance spectra for two samples with different thickness are shown in Fig. 5.1. The approach chosen for data evaluation can be easily described on the basis of this comparison. Both spectra are characterized by one dominating

arc which is rather semicircle-like for thinner layers (100-140 nm) and strongly distorted for the thicker one (413 nm). The small additional feature at low frequencies was erratically pronounced (never large) and is neglected in the following analysis. For the thinner layer with a thickness of ca. 100 nm a simple R-CPE (CPE denotes Constant Phase Element) could be used to excellently fit the spectra. The impedance of the CPE is given by

$$Z_{CPE} = \frac{1}{(i\omega)^n Q} \quad (5.1)$$

By using the complex nonlinear least square (CNLS) fit program Z-View (Scribner,USA) the parameterization was carried out. Owing to the increased layer thickness (see (c) and (d) in Fig. 5.1) an equivalent circuit with an additional R_S-CPE_S element was used to take account of the high frequency shoulder. Then again excellent fit quality could be obtained as shown in these complex impedance and modulus planes in Fig. 5.1. For a further analysis of capacitance contributions the CPE elements were converted into real capacitances by Eq. 5.2.^[93] Values of n obtained for both, CPE₁ and CPE_S are between 0.98 and 0.95.

$$C = (R^{(1-n)} \cdot Q)^{(1/n)} \quad (5.2)$$

Resistance and capacitance values were evaluated for each sample and the results are plotted against layer thickness to analyze whether the observed semicircle originates from the entire Fe-doped SrTiO₃ layer or from interfacial regions only. The corresponding diagram is depicted in Fig. 5.2 and shows a continuous change of resistance as well as capacitance for changing thickness. This strongly suggests that the observed processes are not mainly caused by the interfaces to the electrodes but originates from the interior of the acceptor-doped SrTiO₃ layer. For the thicker layers (230 nm and 413 nm) two resistance and capacitance values result from the fit and the total resistance and capacitance values plotted in Fig. 5.2 (R_{HF,total} and C_{HF,total}) are then defined by

$$R_{HF,total} = R_1 + R_s \quad \text{and} \quad C_{HF,total} = \frac{1}{\frac{1}{C_1} + \frac{1}{C_s}} \quad (5.3)$$

For thinner layers R_{HF,total} = R₁ and C_{HF,total} = C₁ is used. In the next step, total capacitances were taken to gain relative dielectric permittivity (ε_r) values

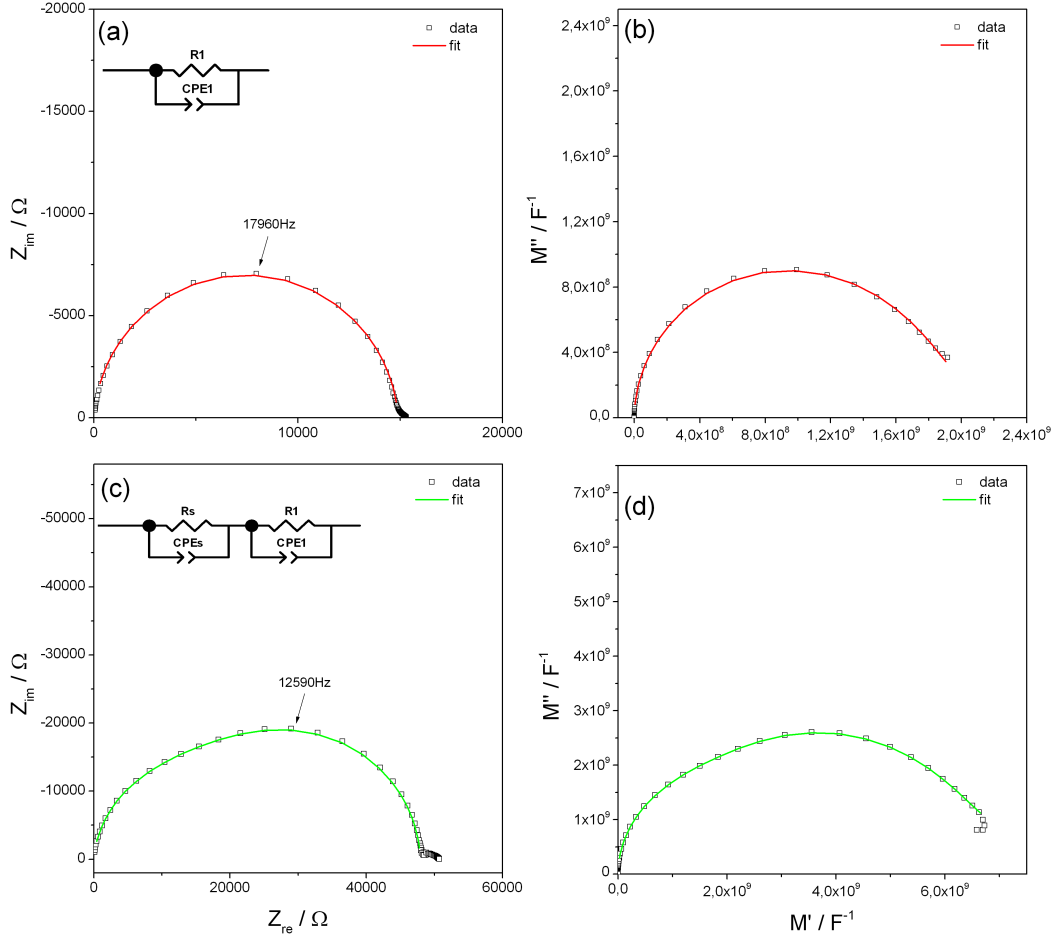


Figure 5.1

Fig. 5.1: Impedance data (Nyquist plot shown in (a) and (c), Modulus plot shown in (b) and (d)) for a 100 nm sample at 600°C and a 314 nm sample at 620°C, measured without applied bias voltage. In (a) and (c) the used equivalent circuits and the fits –in red and green– are also depicted in this illustration.

by using Eq. 5.4, with d_{layer} denoting the layer thickness, A_{el} describes the electrode area and ϵ_0 has its usual meaning.

$$\epsilon_r = \frac{C_{HF,total} d_{layer}}{\epsilon_0 A_{el}} \quad (5.4)$$

The results for different thicknesses are shown in Tab. 5.1 and reveal Curie-Weiss-type behavior, i.e. the permittivity value decreases with increasing temperature. The obtained values are in good agreement with literature data^[94–99] assembled by DeSouza *et.al.*^[25].

The monitored total resistance values ($R_{HF,total}$) were converted into conductivity values, using the following equation:

$$\sigma = \frac{1}{R_{HF,total}} \cdot \frac{d_{layer}}{A_{el}} \quad (5.5)$$

layer thickness [nm]	rel. dielectric constant ϵ_r	temperature [°C]
100	128	407
	92	504
	91	600
	82	672
132	133	409
	128	508
	121	606
	118	631
125	132	490
	124	609
	122	634
157	147	403
	126	500
	130	595
230	125	487
	117	534
	113	609
413	111	595
	106	643
	101	690
bulk sample (grain)	163	429
	131	479

Tab. 5.1: Evaluation of the relative dielectric constant ϵ_r for different layers under different temperatures, compared with results for the grain part of the bulk sample.

The activation energy was determined in accordance with

$$\ln(\sigma) = \ln(\sigma_0) - \frac{E_a}{k_B T} \quad (5.6)$$

The analysis of the conductivity versus temperature is shown in Fig. 5.3 for samples with varying layer thickness. The diagram not only shows the Arrhenius data for all investigated samples but also compares the achieved data for the thin films with data obtained from a polycrystalline bulk sample and literature data^[33,68]. The bulk sample was a pellet originally used as a target for PLD thin film preparation. It was polished and on both sides covered with LSC layers. In accordance with literature^[16,18,21,33], two semicircles were found in the complex impedance plane, one caused by grain boundaries and the other by the grain interior, respectively. The measured data are plotted as Nyquist plot (a) and also as Modulus plot (b) in Fig. 5.4, including fit results using two serial R-CPE elements.

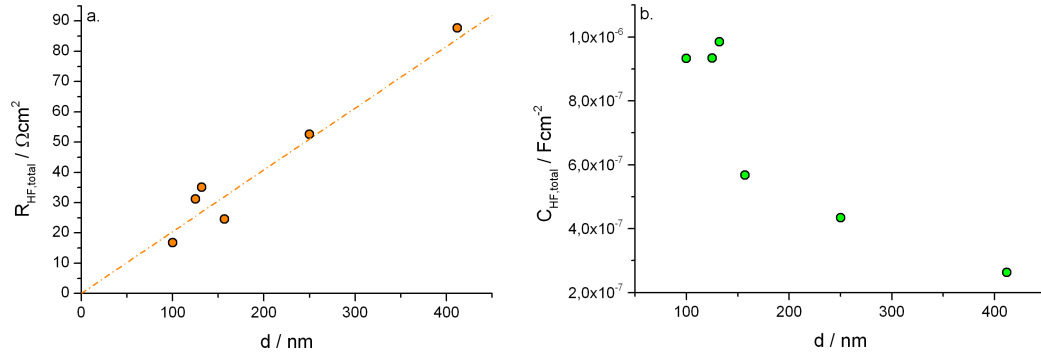


Figure 5.2

Fig. 5.2: In (a) the resistance and in (b) the capacitance is plotted against the layer thickness for 500°C .

The calculation of the activation energies for grain boundary and bulk part from the Arrhenius plot of the polycrystalline sample led to values which are in very reasonable agreement with literature data.^[33] From the Arrhenius diagram for the thin films it becomes also very obvious that there is a strong shift to lower conductivities by 3 orders of magnitude, compared to the bulk sample. Moreover, the activation energy for the thin films is in the order of 1.65 eV and therefore much higher than that of the bulk sample grains (≈ 0.95 eV) and also somewhat higher than the grain boundary activation energy of the polycrystalline sample (≈ 1.4 eV). However, higher grain boundary activation energies are also reported for polycrystalline samples.^[27] From the results achieved by TEM measurements, where no grain boundaries in the SrTiO₃ layer grown on Nb-SrTiO₃ could be found (see Section 4.2), we would expect that the analyzed activation energy is in the range of the grain bulk value. However, space charge layers may not only appear at grain boundaries but also at interfaces/surfaces or dislocations. Assuming a high dislocation density in our layers, may explain the observed results.

As Balaya *et. al.*^[77,78] showed, a characteristic grain size exists at which the bulk response disappears due to an overlap of space charge regions (see Section 2.2). Then the size of the remaining arc in the impedance plane is determined by the depleted charge carriers but still reflects the capacitance properties of the grain bulk. This idea of overlapping space charge layers can also be applied to our thin film situation even though the films are free of grain boundaries, since dislocations can still be located very close to each other and lead to a network of overlapping space charge regions. This would explain the low conductivity and also the grain bulk-type capacitive behavior. Moreover, the

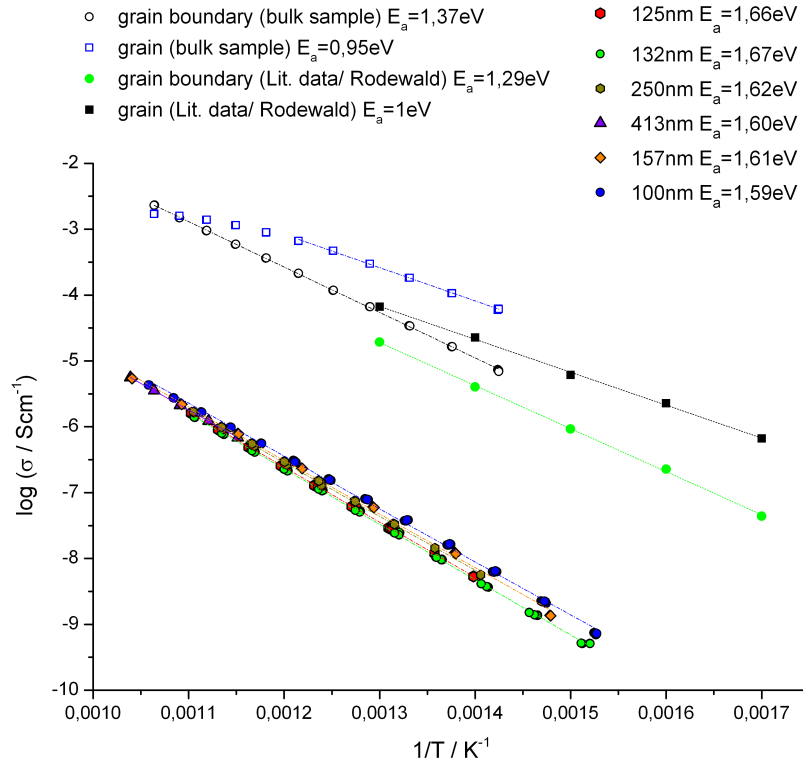


Figure 5.3

Fig. 5.3: The shown Arrhenius plot contains the measured data for the thin layer samples, further grain and grain boundary data and literature data^[33] are shown.

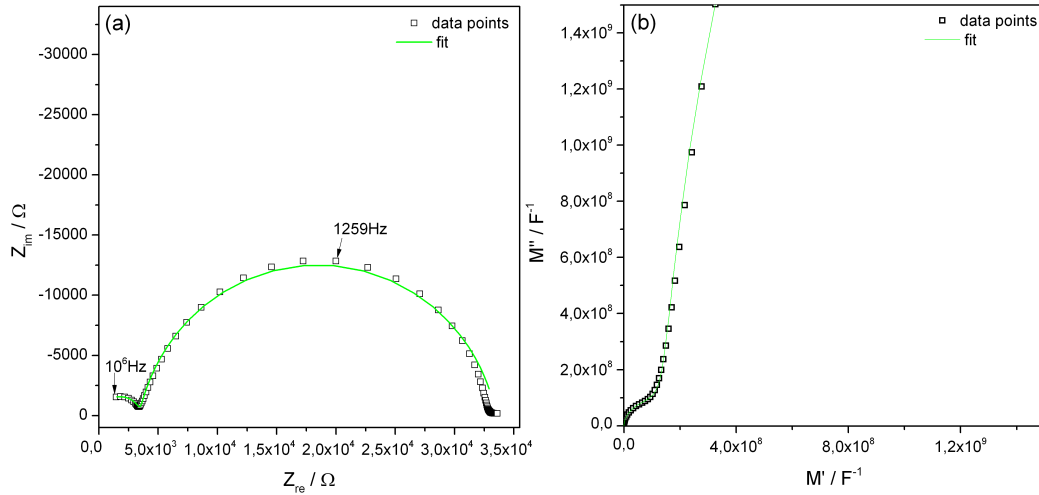


Figure 5.4

Fig. 5.4: Nyquist plot (a) and Modulus plot (b) for the polycrystalline bulk sample of Fe-SrTiO₃ at 454°C, measured in the "Micro-Macro" setup.

activation energy of the resistances of space charge related regions is expected to be higher than the bulk activation energy, cf. Rodewald *et.al.*^[68], in accordance with the thin film results. There only remains the question why a larger film thickness leads to an additional shoulder. This will be further discussed in Sec. 5.2. However, since only the entire sample capacitance $C_{HF,total}$

scales with the sample thickness it is excluded that the high frequency shoulder reflects film bulk properties.

5.2 Impedance measurements performed under variable bias voltage

In the next experimental step AC experiments were performed while an additional bias voltage was applied. The bias values were in the range from -400 mV to $+400$ mV and the steps between each bias point varied from 50 mV to 200 mV. Measurements were performed for different temperatures, hence an Arrhenius analysis of the different processes was possible. Especially in the low frequency part of the spectra the bias voltage has a strong effect. This often manifests itself in a second semicircle for negative bias and in an "inductive" loop under positive bias voltage. This was the most frequently observed case for the investigated thin Fe-doped SrTiO₃ thin layers. However, in some cases the transition from loop to arc was shifted to other bias values or further features were found. For the sake of completeness all effects that were monitored in the experiments are shown at the end of this chapter.

Fig. 5.5 illustrates the standard features under DC voltage by showing a complete bias cycle for a 413 nm sample. A second semicircle (cathodic, Fig. 5.5(a)) as well as the loop (anodic, Fig. 5.5(c)) can be observed. The results shown for this sample, are used to describe the observed phenomena, but all addressed aspects are valid for many other samples which show the same bias trends. The second semicircle is subjected to a distinct increase with increasing voltage and in this case the second semicircle becomes even more pronounced than the high frequency feature for -300 mV.

However, the bias voltage not only has an impact on the low frequency part, but also affects the high frequency semicircle. The corresponding resistance again increases with increasing negative bias. Moreover another interesting effect occurs: First evidence of a high frequency shoulder was already found for the measurement without bias (413 nm sample). Under negative bias this shoulder becomes clearly visible (see impedance spectra in Fig. 5.5(b)). For thinner layers without any shoulder in the case of missing external bias voltage, the shoulder also appeared under negative applied bias. In order to see whether

these phenomena are associated with irreversible processes taking place under bias voltage, temperature cycles from 400°C to 700°C were performed, with bias cycles from -200 mV to +200 mV at each temperature. The results of this experimental series are depicted in Fig. 5.6 and clearly show that temperature as well as bias do not change the samples irreversibly. Rather excellent stability and reproducibility were found for all experimental conditions and even after days of measuring.

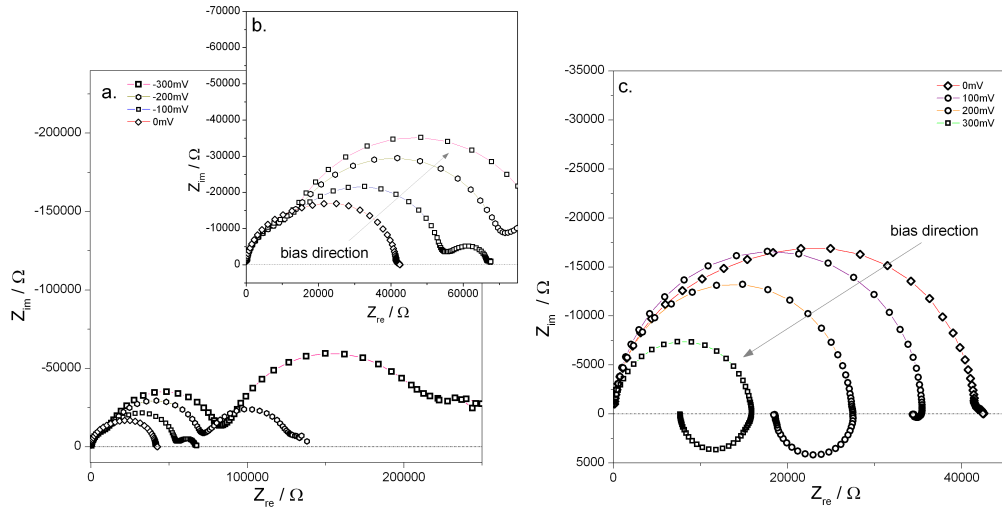


Figure 5.5

Fig. 5.5: Representation of a bias cycle performed for the 413 nm sample at 700°C (T_{set}) in the "Micro" set-up, where the negative bias range is shown in (a) with an additional zoom in of the high frequency feature (b). The negative bias range with its appearing loop is shown in (c).

5.2.1 Quantitative analysis of impedance spectroscopy data

The impedance data shown in the previous section raise the question about a reasonable equivalent circuit to parameterize and understand the measured spectra. The first approximation of a potential equivalent circuit is shown in Fig. 5.7(a). The resistive high frequency part of the spectra is represented by $R_{STOfilm,fast}$ and describes the high frequency "bulk" resistance of the Fe-doped SrTiO₃ film. In series to this resistance a second component indicated as ΔR_{slow} is assumed, which reflects the difference between high and low frequency impedance, i.e. the size of the loop or second semicircle. The exact meanings of the subscripts "fast" and "slow" are related to the fast and slow U-I curves (see Chapter 7). Further the geometrical capacitance C_{geom} as well

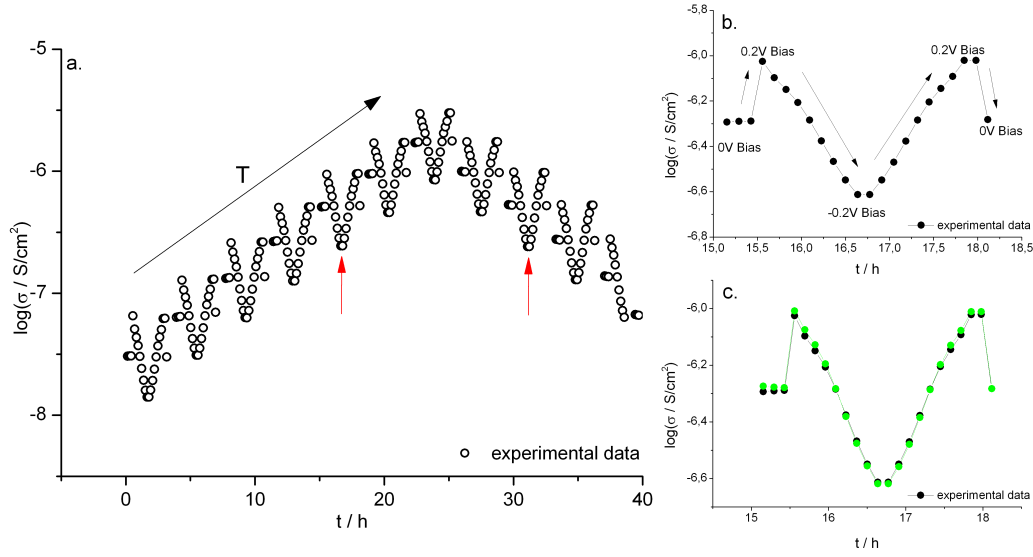


Figure 5.6

Fig. 5.6: Results for checking whether the ongoing processes are fully reversible. The diagram in (a) shows a complete measurement series with all changes in temperature as well in bias. In (b) one cycle is emphasized and in (c) two cycles at the same temperature with more than 10 hours between these two cycles are compared.

as the serial element ($R_{ion}C_{el}$) are connected in parallel. The latter represents the ionic current which is blocked by one electrode. This circuit is a simplification of a more exact circuit given in Ref.^[100].

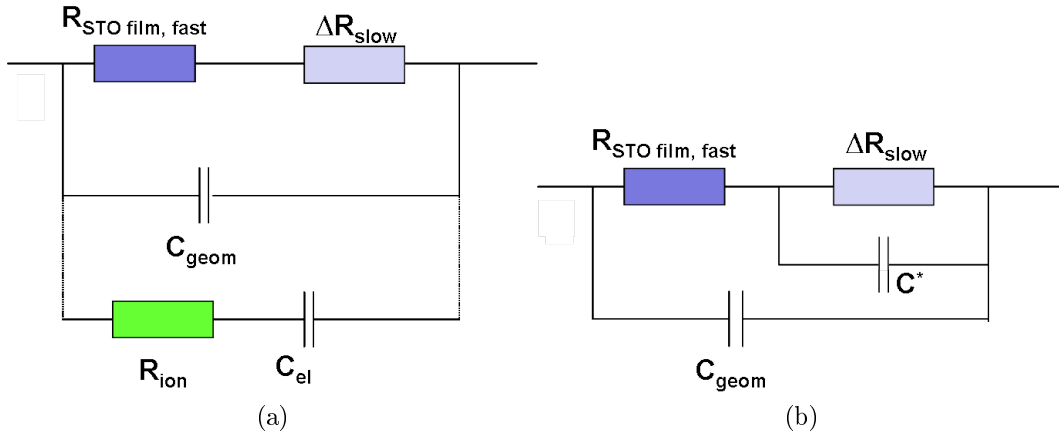


Figure 5.7

Fig. 5.7: In (a) the first approximation of an equivalent circuit is shown, which was adapted to the equivalent circuit depicted in (b). This is the equivalent circuit which was used to fit all the measured data.

For all further considerations it is important to understand the influence of R_{ion} . In the ideal case of two completely blocking electrodes on both sides of the mixed-ionic-electronic conducting material, R_{ion} would only include transport of oxygen vacancies through the MIEC material, e.g. SrTiO₃. For the situation of one reversible electrode, processes, i.e. incorporation and release of oxygen

at the electrode, electrochemical processes on/in the electrode material and charge transfer from the electrode into the thin film have to be considered too. In addition to these processes a possible bias dependency has to be included. A more accurate description instead of the simple R_{ion} would be Z_{ion} , with all processes involving oxygen vacancy motion.

As it can be seen from Fig. 5.7 the conductive part due to ions is neglected in the subsequently used equivalent circuit, because the ionic resistance is assumed to be much higher than the electronic one. The reason can be found in either the low mobility of oxygen vacancies compared with electronic charge carriers or the strongly reduced concentration of $V_{O}^{\bullet\bullet}$ in space charge regions. Although these assumptions were made, R_{ion} plays an important role in the subsequent interpretation. The remaining current path with $R_{STOfilm,fast} + \Delta R_{slow}$ originates from electrons and holes, but the reason why electrons and holes are affected by a bias voltage and thus cause ΔR_{slow} is again related to ion motion.

First, the DC voltage causes a gradient in the oxygen vacancy concentration in accordance with the Wagner-Hebb model. This process takes place before the impedance spectrum is measured or within the time frame of recording the very first high frequency data, cf. Section 8 (time dependence). On the way from high to low frequencies the $V_{O}^{\bullet\bullet}$ have more and more time to react on the applied AC signal (10 mV). As a consequence the already existing gradient in the oxygen vacancy concentration is changed within each half wave of a low frequency AC signal, accompanied by a compensation via electrons and/or holes. This process is reflected by ΔR_{slow} . To quantify this behavior, a weight factor $F(\omega)$ is introduced which is 0 for the extreme case of high frequencies, and 1 for the situation where ΔR_{slow} is "switched on". The weight factor represents nothing but the ion flow which could be neglected in terms of its contribution to the total current (see above) but not in his effect on the electronic current via compositional changes. In Eq. 5.7 $F(\omega)$ is defined as the ratio of voltage drop on C_{el} and the total voltage ($U_{R_{ion}C_{el}}$). This is very much like the charging process of a capacitor. To charge the capacitor completely, a certain time has to pass by (due to the serial resistor) and this is also valid for oxygen vacancy migration under an electric field.

Instead of the voltage ratios the behavior can also be described by impedances and those can be further expressed in terms of resistance and capacitance (see Eq. 5.7). With this new parameter $F(\omega)$, it is possible to define an impedance Z^* (Eq. 5.8). Definition of R^* and C^* according to Eq. 5.9 lead to the last term of Eq. 5.8 which is a R^*C^* element in parallel. Whether R^* and C^* lead to a second semicircle or an additional loop at low frequencies depends on whether the value for both parameters is positive or negative, i.e. on the sign of ΔR_{slow} , see below.

$$F(\omega) = \frac{U_{C_{el}}}{U_{R_{ion}C_{el}}} = \frac{Z_{C_{el}}}{Z_{R_{ion}C_{el}}} = \frac{1/i\omega C_{el}}{R_{ion} + 1/i\omega C_{el}} \quad (5.7)$$

$$\begin{aligned} Z^* &= \Delta R_{slow} F(\omega) = \Delta R_{slow} \frac{1/i\omega C_{el}}{R_{ion} + 1/i\omega C_{el}} \\ &= \frac{\Delta R_{slow}}{1 + i\omega C_{el} R_{ion}} = \frac{R^*}{1 + i\omega R^* C^*} \end{aligned} \quad (5.8)$$

$$R^* = \Delta R_{slow} > 0 \quad \text{or} \quad < 0 \quad (5.9)$$

$$C^* = C_{el} \frac{R_{ion}}{\Delta R_{slow}} > 0 \quad \text{or} \quad < 0$$

Using this equivalent circuit approach, impedance spectra for both cases were simulated to check if the established model indeed leads to the two types of spectra measured experimentally. The obtained data is pictured in Fig. 5.8 and Fig. 5.9 showing on the left hand side the Nyquist plot and on the right hand side the Bode plot. Obviously loops as well as second arcs result, depending on the sign of ΔR_{slow} (negative values cause loops).

Many measured impedance data for positive bias can be successfully fitted with the described equivalent circuit, keeping in mind that R^* and C^* can adopt negative values. Fig. 5.10(a) shows the impedance data for the anodic (again for the 413 nm sample) with the associated fit. However, the equivalent circuit needs to be adapted for the data under negative bias, due to the shoulder formed at the highest frequency points (see Fig 5.10(b)). To highlight this additional feature, the modulus plot for those two spectra is shown in Fig. 5.10(c), and again clearly displays two separated high frequency contributions. In the zoom of Fig. 5.10(c) the low frequency part is visible. It displays the

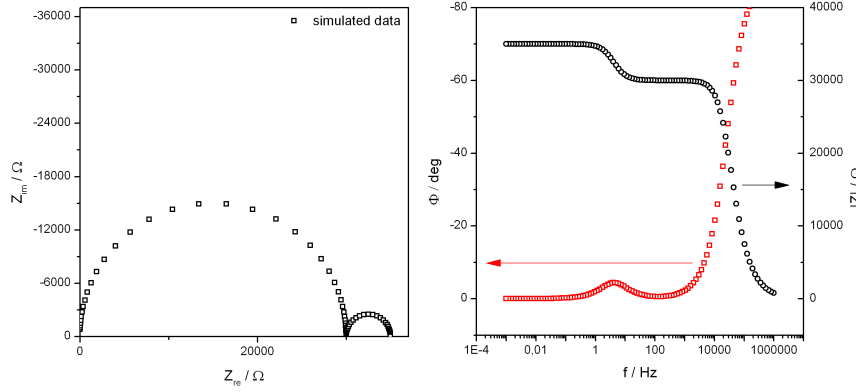


Figure 5.8

Fig. 5.8: Simulation of an impedance spectrum with a positive ΔR_{slow} , resulting in a second semicircle in the lower frequency part.

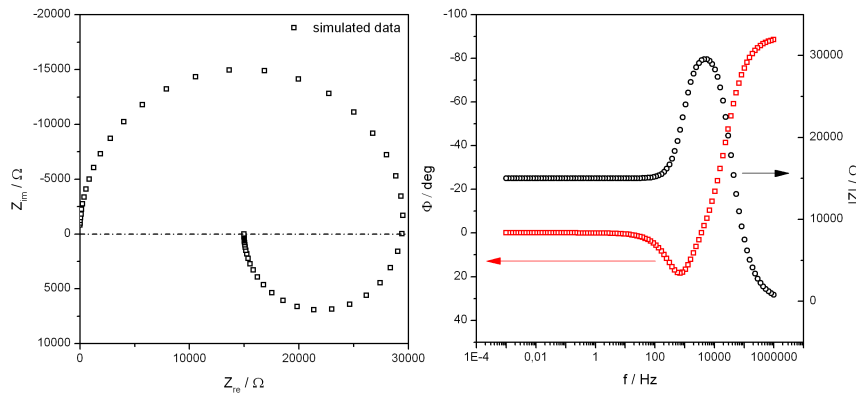


Figure 5.9

Fig. 5.9: Impedance spectrum containing a loop which results for a negative parameter ΔR_{slow} .

situation for a negative capacitance value of the loop, in comparison to the characteristics of a second semicircle.

5.2.2 Analysis of resistance and capacitance values in dependence of applied bias and temperature

In the following, all fit results and their dependence on bias and temperature are discussed. For a better overview all results related with $R_{STOfilm,fast}$ and C_{geom} are denoted as R_1 and C_1 , respectively. Resistance and capacitance in the low frequency range are addressed as R_2 and C_2 during evaluation. As it was depicted in Fig. 5.10(b) a third equivalent circuit element was used to describe the appearing shoulder feature in the highest frequency range (start frequency = 10^6 Hz). In the description and following discussion, the resistance and the capacitance which are caused by this shoulder are denoted as R_S and C_S .

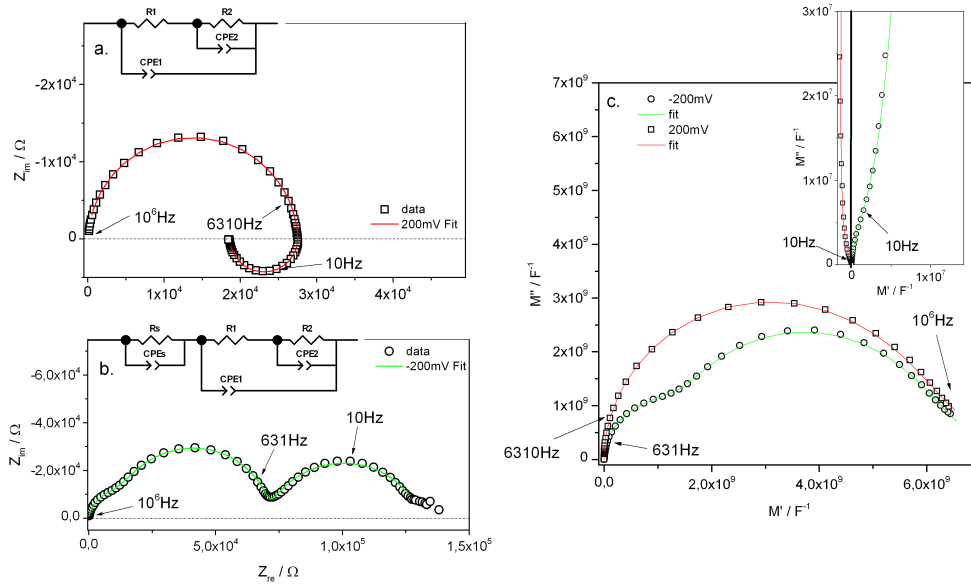


Figure 5.10

Fig. 5.10: Fitting results obtained from the given equivalent circuit for measurements on a 413 nm sample for different bias voltages (+200 mV (a) and -200 mV (b)) at 600°C. In (a) and (b) the data is plotted in the Nyquist plot. In (c) both spectra are compared in the Modulus plot.

For a better overview the observed behavior of several investigated STO thin layers under varying applied bias is separately discussed for the anodic and cathodic range. Furthermore, the results are firstly analyzed for the higher frequencies (R_1 , R_S and C_1 , C_S). Subsequently the low frequency range with the two parameters R_2 and C_2 is evaluated. The results shown on the following pages sum up observations which were made for several samples. Differences in the evaluated data will be discussed at the corresponding position in the text.

• Analysis of R_1 and R_S in the cathodic range

In the high frequency range, differences in the shape of impedance spectra due to a variation in layer thickness could be observed already for data without an applied bias as it was shown in Fig. 5.1 and again in Fig. 5.11. The most pronounced high frequency shoulder was observed for the thickest STO film (413 nm). The negative bias range is characterized by an increased visibility of this shoulder in the first frequency points (see Fig. 5.14 (413 nm), Fig. 5.15 (157 nm), Fig. 5.16 (161 nm) and Fig. 5.13 (125 nm)). The strongest separation of this shoulder feature from the main arc could be observed again for the thickest layer.

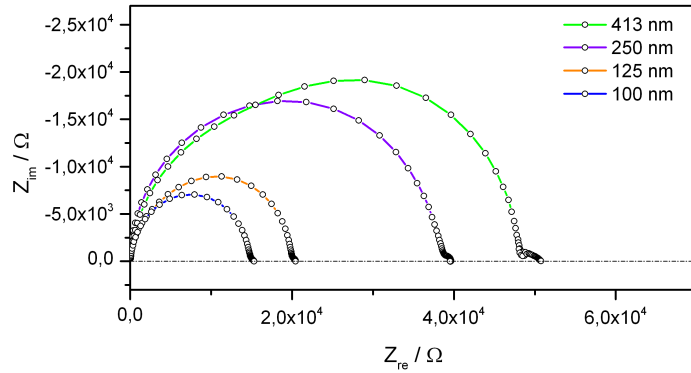


Figure 5.11

Fig. 5.11: Comparison of high frequency impedance arcs measured without an external applied bias for 4 layers with varying layer thickness. Measurements were performed on 300 μm electrodes using the "Micro" as well as the "Micro-Macro" set-up at around 615°C.

Although thinner layers showed an almost ideal impedance arc in the "no-applied-bias" case, cathodic bias voltage leads to an impedance arc which represents more than one process. From the results of a 125 nm layer shown in the Nyquist plot (Fig. 5.12(a)) the high frequency feature is difficult to analyze.

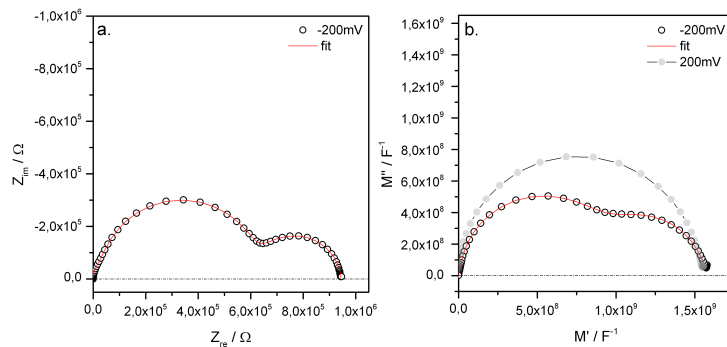


Figure 5.12

Fig. 5.12: For the 125 nm sample despite the minor high frequency feature in the Nyquist plot (a) a distinct difference between spectra recorded at +200 mV and -200 mV can be found by illustrating the data in the Modulus plot (b).

On this account the appropriate impedance data was also depicted in Modulus plot (see Fig. 5.12(b)). Therein, two quite nicely separated semicircles can be monitored due to the different peak frequencies ($\omega = \frac{1}{RC}$ and $f = \frac{\omega}{2\pi}$) of the two processes ($f_1 = 892$ Hz and $f_S = 12923$ Hz under the depicted conditions). The observed behavior is furthermore emphasized by comparing the results for the cathodic bias with data for the anodic regime (grey colored semicircle). The semicircle recorded under positive bias voltage is clearly characterized by only one process. By means of these observations, the evaluations of the

cathodic high frequency impedance data by using 2 R-CPE elements seems quite reasonable.

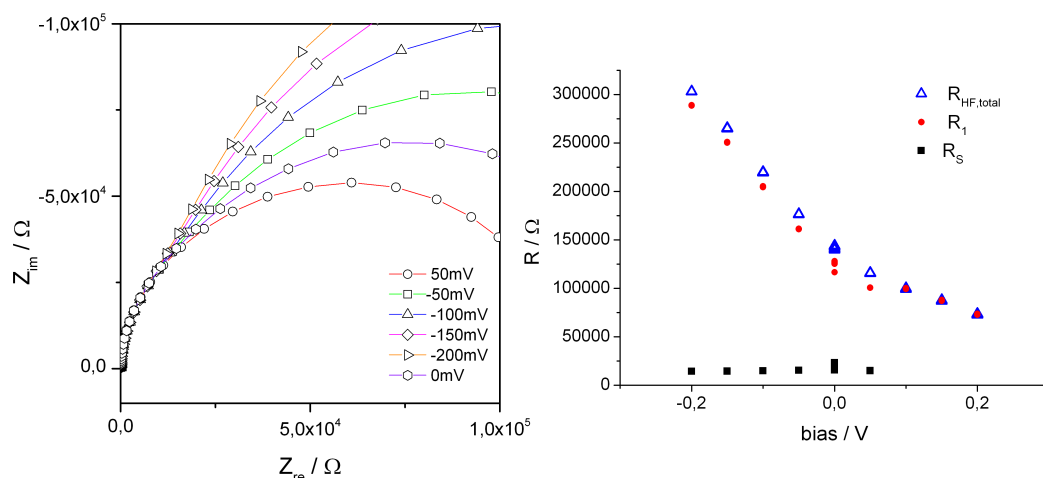


Figure 5.13

Fig. 5.13: Analysis of the high frequency response of a 125 nm layer at 540°C ("Micro-Macro" set-up), impedance spectra measured with different values of cathodic bias show only a minor development of a shoulder response. An evaluation of R_S , R_1 is still possible and the results are plotted together with $R_{HF,total}$.

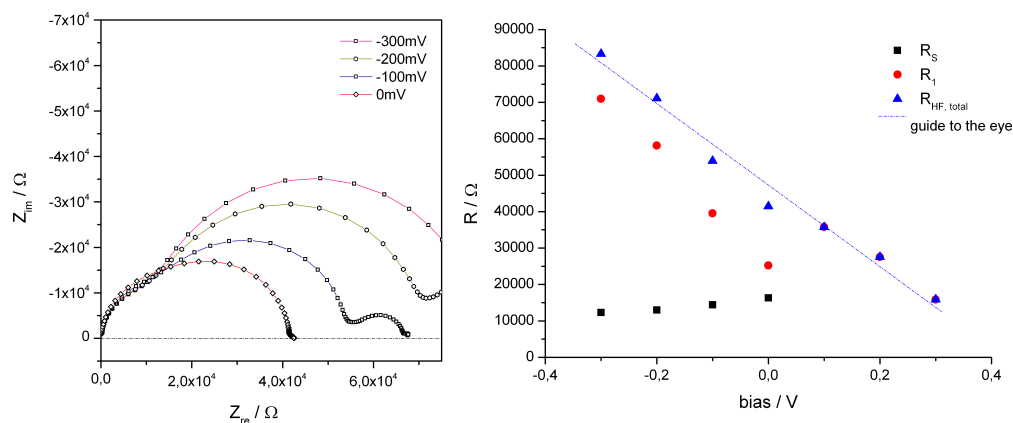


Figure 5.14

Fig. 5.14: High frequency part of the impedance spectra (measured on a 413 nm sample) compared for different bias voltages (left hand side) and resistance values plotted against bias for the cathodic range (right hand side).

Plotting both resistance values (R_1 and R_S) against bias yields an interesting result: The high frequency shoulder (R_S) only slightly depends on the applied bias voltage, in contrast to the distinct changes of the main semicircle (R_1). A closer look reveals a minor opposite progress of resistance values R_S and R_1 for some samples under the applied voltage (see Fig. 5.14 - Fig. 5.16). In Fig. 5.15 it can be seen that the low frequency feature (in this case a loop was observed) does not influence the high frequency part of the plot. Therefore,

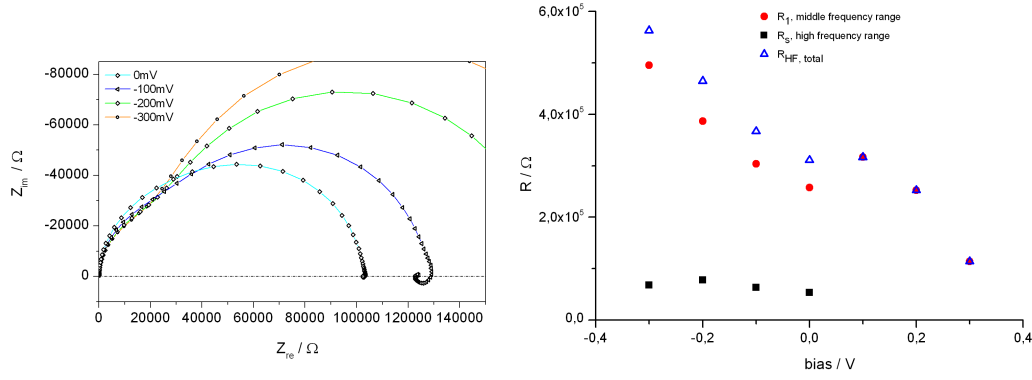


Figure 5.15

Fig. 5.15: Analysis of the $R_{HF,total}$ part for a 157 nm sample at 600°C (T_{set}) investigated in the "Micro" set-up.

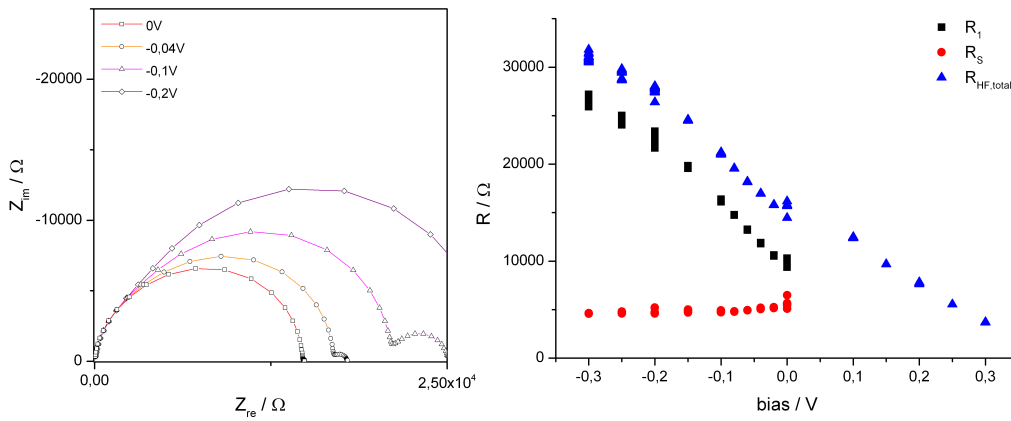


Figure 5.16

Fig. 5.16: Analysis of the high frequency shoulder feature monitored for negative bias voltages for a 160 nm sample.

this distinct thinner sample also exhibits a high frequency shoulder, which is although less pronounced than the shoulder for the thicker layers.

Spatial changes of space charge layers due to the response of the material on bias voltage might provide an explanation at least for the bias dependence of R_1 . Firstly, the density of dislocations could play an important role. A high density of dislocations in the thin layer, may lead to an overlap of the regions of depleted charge carriers in the vicinity of these imperfections and thus to a "homogeneously depleted" material, as it was already mentioned in Sec. 2.2. Such an entirely depleted thin layer would exhibit, on the one hand, a decreased total conductivity. On the other hand, bias dependence of grain boundaries have been assigned to space charge zones in the vicinity of grain boundaries. Therefore the space charges in a "homogeneously depleted" thin layer should also react on the bias voltage.

Beside this aspect, the position of dislocations is important especially when an applied bias voltage causes an asymmetry of the investigated system. Only those defects which are located partly crosswise to the surface/interface feel the driving force of the applied electric field, and only the space charge layers of these dislocations may change upon bias. The situation resulting for space charges under perpendicular bias was already illustrated in Fig. 2.5. Owing to its high resistance value, which is in the same order of magnitude as the value for the main arc, the shoulder-like feature cannot be caused by unperturbed bulk material. Rather, it is much more probable that the thin layer includes different origins for the generation of space charge zones, e.g. dislocations with a wide variety of positions, surface and/or interface. Therefore an applied bias could change the "fully" overlapping state of the layer into a more diverse situation by partly loosing the "homogeneously depleted" situation.

- **Analysis of $R_{HF,total}$ in both bias directions**

In addition to the development of resistance data in the cathodic range, the results also for the anodic range are depicted in the illustrated diagrams (see Fig. 5.14 (413 nm), Fig. 5.15 (157 nm), Fig. 5.16 (161 nm) and Fig. 5.13 (125 nm)). With few exceptions, the anodic part could be analyzed by using one R_1 -CPE₁ element due to the almost ideal first semicircle (high frequencies). The high-frequency part of the anodic data shows also a distinct dependence on the magnitude of the applied bias voltage: The resistance of the first semicircle decreases with increasing anodic bias. This is in clear contrast to the increase of the total resistance with increasing cathodic bias voltage.

Summing up R_1 and R_S to a total cathodic resistance $R_{HF,total}$ brings the evaluated cathodic data sets more in line with the anodic resistance values. Although a shift in the resistance values due to the change in the algebraic sign of the bias could still be found for some samples, cf. Fig. 5.15, the general trend is very obvious: $R_{HF,total}$ is largest for the most negative bias and smallest for the most positive one with an almost continuous decrease in between.

For the subsequent evaluation of conductivity values the total resistance ($R_{HF,total}$) was used. Results for the bias (a) and temperature (b) dependence of the conductivity for a 413 nm sample are depicted in Fig. 5.17. In comparison results for a 125 nm samples are shown in Fig. 5.18. A linear

behavior for the bias dependence of this sample is plotted in (a). In (b) the Arrhenius plot is shown for all investigated bias voltages. As it was shown for the thicker layer the evaluated activation energies for this sample again scatter only slightly around the value for the 0 V bias measurement.

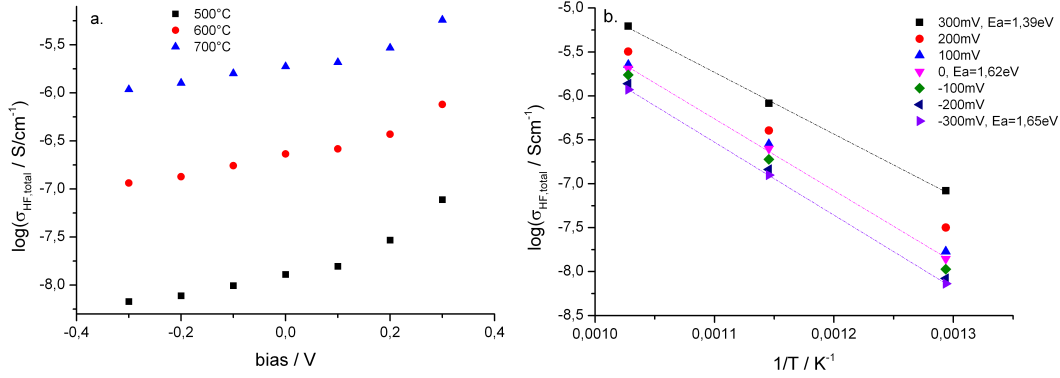


Figure 5.17

Fig. 5.17: Illustration of the bias dependency of the conductivity for the HF-semicircle of the 413 nm sample (conductivity evaluated from $R_{HF,total}$) (a). Arrhenius plot for the complete applied voltage range (b).

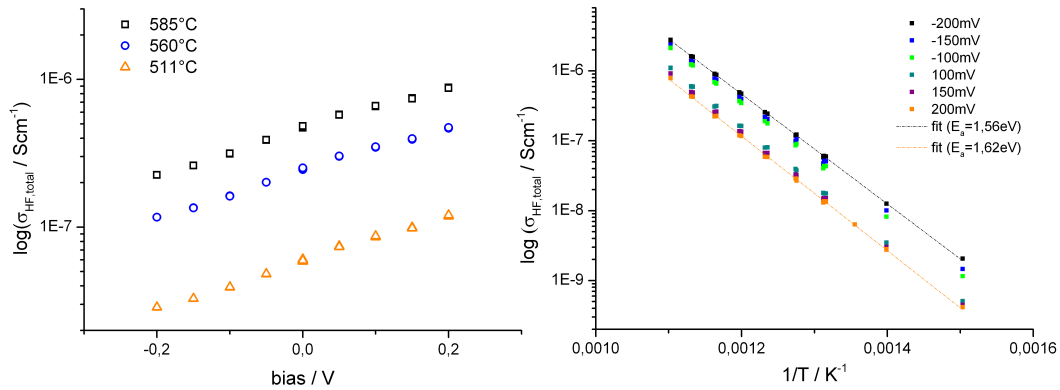


Figure 5.18

Fig. 5.18: Behavior of the high frequency part of the impedance measurement, performed on a 125 nm sample under different temperature over a bias range from -200 mV to $+200$ mV.

In Fig. 5.19 normalized high frequency resistance ($R_{HF,total}$) values are plotted against layer thickness. In this case the resistance values were evaluated for measurements performed under $+200$ mV and -200 mV. As it can be seen from the depicted diagram, a clear linear behavior can be found for both bias voltages. These results again indicate that the entire layers are measured. Because of the fact that $R_{HF,total}$ is evaluated, the approach that two serial regions in the material are probed by impedance spectroscopy under applied bias voltage is reinforced.

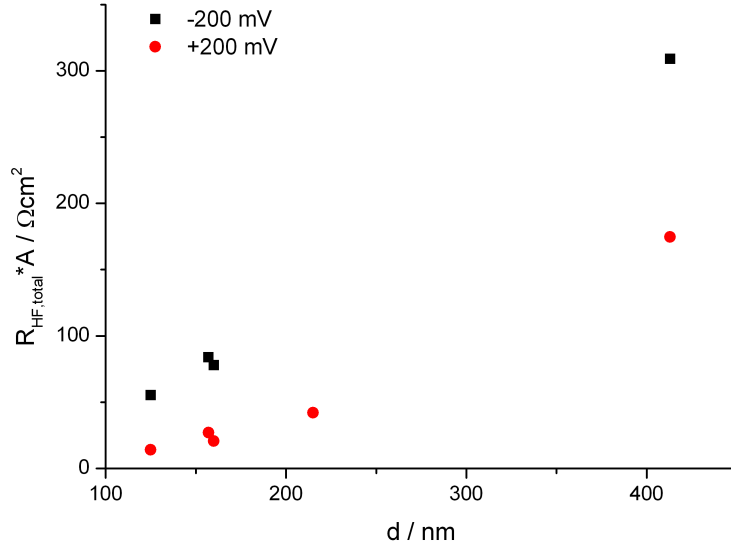


Figure 5.19

Fig. 5.19: Evaluation of the thickness dependence of $R_{HF,total} \cdot A$ for ± 200 mV, measured at a temperature of around 600°C .

• Analysis of R_2 for the anodic and cathodic bias regime

Under applied bias the low frequency part of the measured impedance spectra became interesting due to the either appearing second semicircle (cathodic range) or loop (anodic range). Impedance data for two different thin films are shown in Fig. 5.20 and Fig. 5.21. The impedance data recorded under

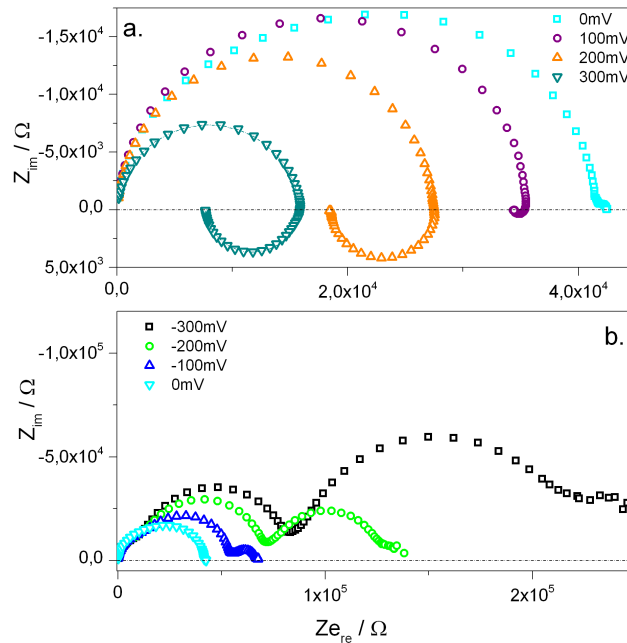


Figure 5.20

Fig. 5.20: Impedance plots of a 413 nm sample for the anodic (a) and the cathodic (b) range recorded at 700° (T_{set}). 3 different bias voltages are depicted and compared with the plot measured at 0 V bias.

relatively small anodic applied bias (approx. +20 mV to +100 mV) show none

or only a very small loop. However, when applying voltages in the range of +200 mV the loop becomes often very pronounced. In the cathodic regime the second semicircle is continuously increasing with increasing bias voltage.

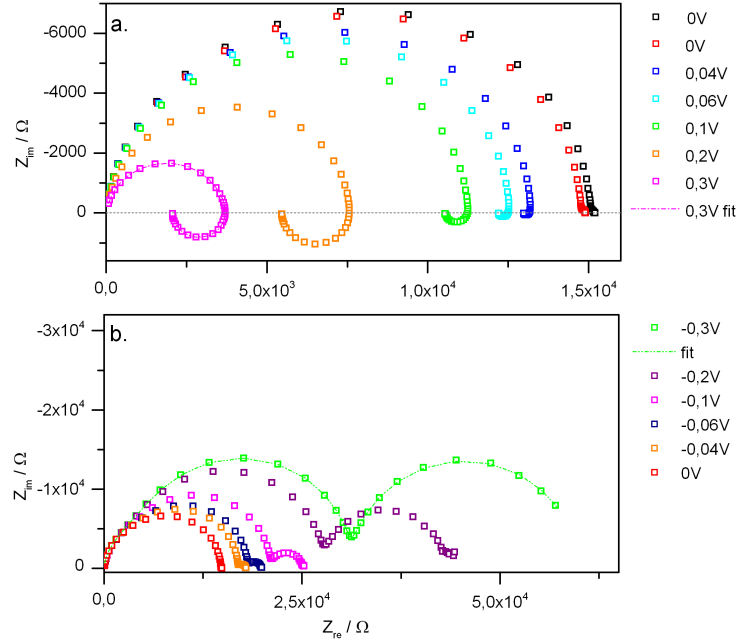


Figure 5.21

Fig. 5.21: Impedance plots of a 161 nm sample. The anodic (a) and the cathodic (b) range are separately depicted (700°C (T_{set})).

For data analysis the already shown and discussed equivalent circuit depicted in Fig. 5.7 (or its extension by R_S and CPE_S , see Fig. 5.10) was used. By permitting a negative sign for R_2 and C_2 it was possible to fit most of the recorded data with this model. For a comparative evaluation the absolute values of R_2 and C_2 were used.

In Fig. 5.22 resistance values are plotted for the entire bias range. On the basis of this graphical plot a clear linear behavior of σ_2 in the cathodic range can be observed. By switching into the anodic range, this linear behavior vanishes. The evaluated values for the positive bias range were more or less independent of bias voltage.

Because of the fact that $R_{HF,total}$ is continuously decreasing with increasing positive bias voltage, the low frequency part becomes increasingly pronounced. On this account the ratio $\frac{R_2}{R_{HF,total}}$ was also analyzed and plotted against bias. The obtained results are depicted in Fig. 5.23. In this diagram 4 samples with varying thickness are compared. The two layers with 161 nm (black) and 413 nm (green) are those samples which showed loops in the entire anodic and

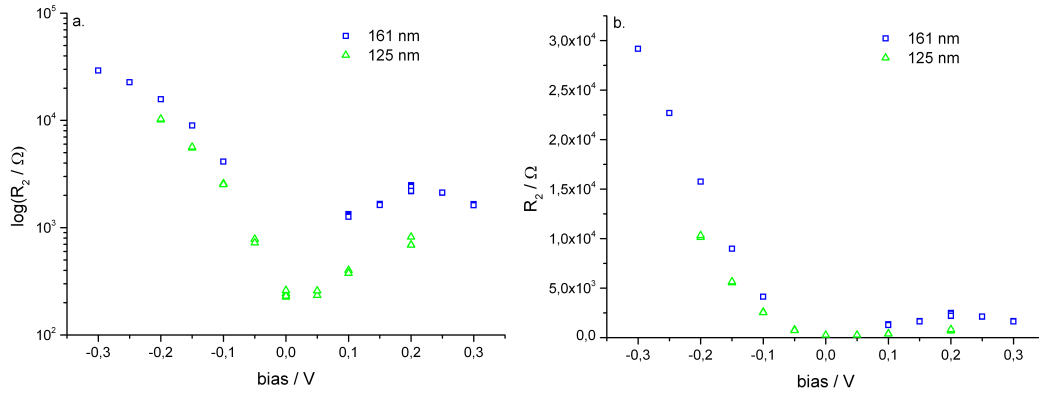


Figure 5.22

Fig. 5.22: R_2 is plotted against bias for two different samples (125 and 161 nm). (Logarithmic plot shown in (a) and in (b) the linear plot is depicted.) In the cathodic range a distinct change in the resistance can be observed. In the anodic range only slight variations can be seen.

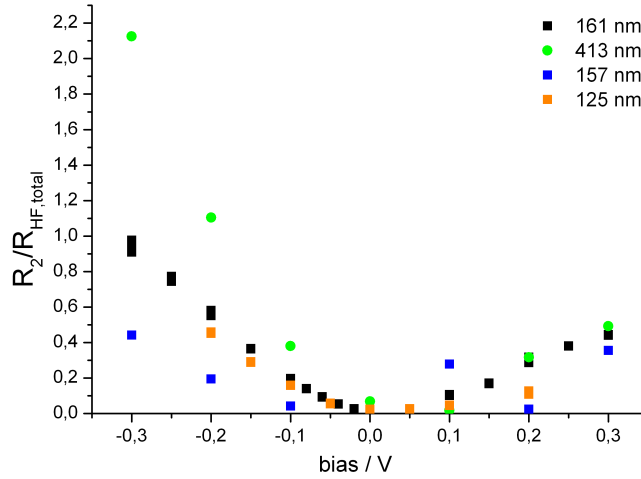


Figure 5.23

Fig. 5.23: The ratio $\frac{R_2}{R_{HF,total}}$ is plotted against bias. 4 samples with varying thickness are compared. The low frequency features become in both cases increasingly important with increasing anodic as well as cathodic bias. (600°C actual temperature)

semicircles in the entire cathodic range. Even though the absolute resistance values of the loop do not change much with increasing bias, they nevertheless become increasingly pronounced with increasing anodic bias. The same behavior was observed for the cathodic range.

Bias measurements were also performed over a broad range of temperatures, thus the data could be analyzed in terms of the activation energy. The corresponding Arrhenius plot is shown in Fig. 5.24. Interestingly both anodic and cathodic activation energies are similar and close to those of the high frequency resistance. This supports our model that both are related to electron/hole transport in the STO film with the R_2 reflecting the change of this

property if oxygen vacancy motion takes place even within a single halfwave of the applied AC signal.

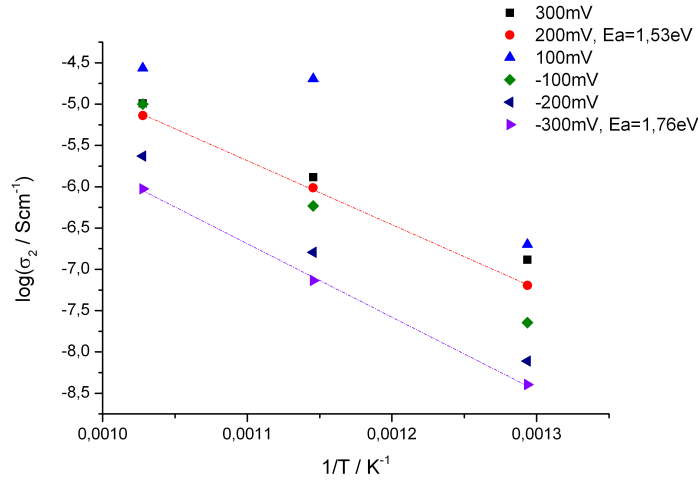


Figure 5.24

Fig. 5.24: Arrhenius plot for the 413 nm sample. Analysis of a possible change in the activation energy of the low frequency process under different bias voltages.

As it was performed for $R_{HF,total}$, low frequency resistance values (R_2) were plotted against layer thickness (d). The resulting trends for +300 mV and -300 mV are depicted in Fig. 5.25. In both cases a clear dependence on the layer thickness can be observed.

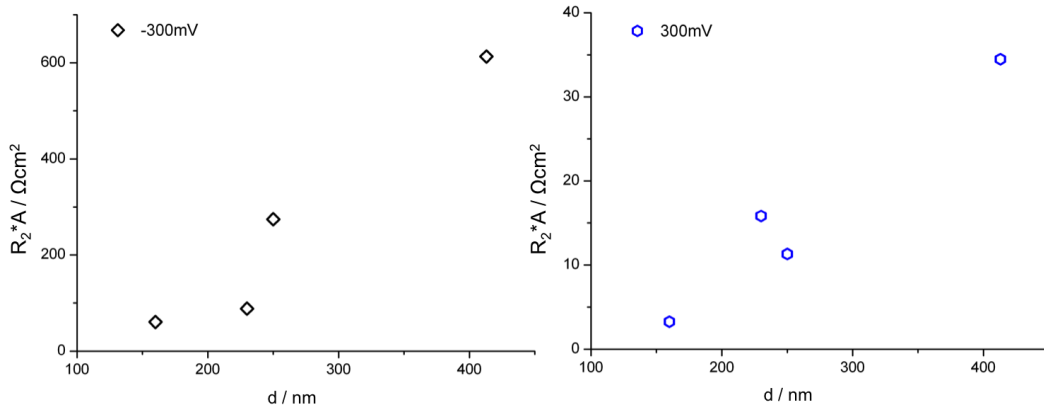


Figure 5.25

Fig. 5.25: Plot of low frequency resistance at +300 mV and -300 mV bias against layer thickness with an obvious bias dependence for resulting resistance in both bias regimes (600°C T_{set}).

- **Summing up all observations made for the analyzed resistances (R_1 , R_S and R_2)**

A clear bias dependence could be found for R_1 as well as for R_2 . R_1 (= high frequency impedance arc) showed a continuous (monotonic) trend over

the entire investigated bias range, despite the fact of a polarity change of the applied voltage. In the anodic range the high frequency part could be fitted by using one R-CPE element. In case of the cathodic experimental data, a shoulder in the highest frequency points appeared under bias. Hence, the equivalent circuit had to be expanded by an additional R-CPE element. This resistance R_S on its own did not show a distinct bias dependence.

The comparative evaluation of the anodic and the cathodic bias range resulted in the approach to take a total cathodic resistance ($R_{HF,total} = R_1 + R_S$). Most probably neither $R_{1,anodic}$ and $R_{1,cathodic}$ nor $R_{1,anodic}$ and R_S describe the same process –meaning charge carrier migration under field– since only the sum ($R_{HF,total}$) shows a continuous bias dependence into the anodic regime ($R_{1,anodic}$).

R_2 is a highly non-trivial resistor, due to the fact that two different responses (loops and semicircle) were observed during measurements. The analyzed activation energy for different bias voltages only slightly deviate from the 0 V bias value. The occurrence of second semicircles in the the cathodic range comes along with a very clear trend in the bias dependence of the evaluated resistance (the more negative the bias, the larger R_2). Resistance values recorded in the anodic range showed more "random-like" bias dependence.

- **Analysis of C_1 and C_S in the cathodic regime**

The capacitance values were analyzed in terms of their bias and temperature dependence. The achieved results are depicted in the following subsection. The occurring shoulder in the high frequency range was fitted by means of an additional R-CPE element. The evaluated CPE was converted into a real capacitance (C_S) by using Eq. 5.2 as it was performed for C_1 . In Fig. 5.26 these two capacitances (C_1 and C_S) are plotted against bias. In addition, the analyzed values for the anodic range (C_1) and $C_{HF,total}$ are depicted.

The consideration of only one capacitance (C_1) in the cathodic regime leads to a distinct step when the capacitance data is plotted over the complete bias range. However, using a total cathodic capacitance ($C_{HF,total}$) leads to an almost constant value over the entire bias range. Hence $C_{HF,total} = C_{1,anodic}$ can be clearly attributed to the entire thickness of the STO thin film while

$C_{1,cathodic}$ and C_S seem to be related to two serial regions in the sample which are both thinner than the entire film.

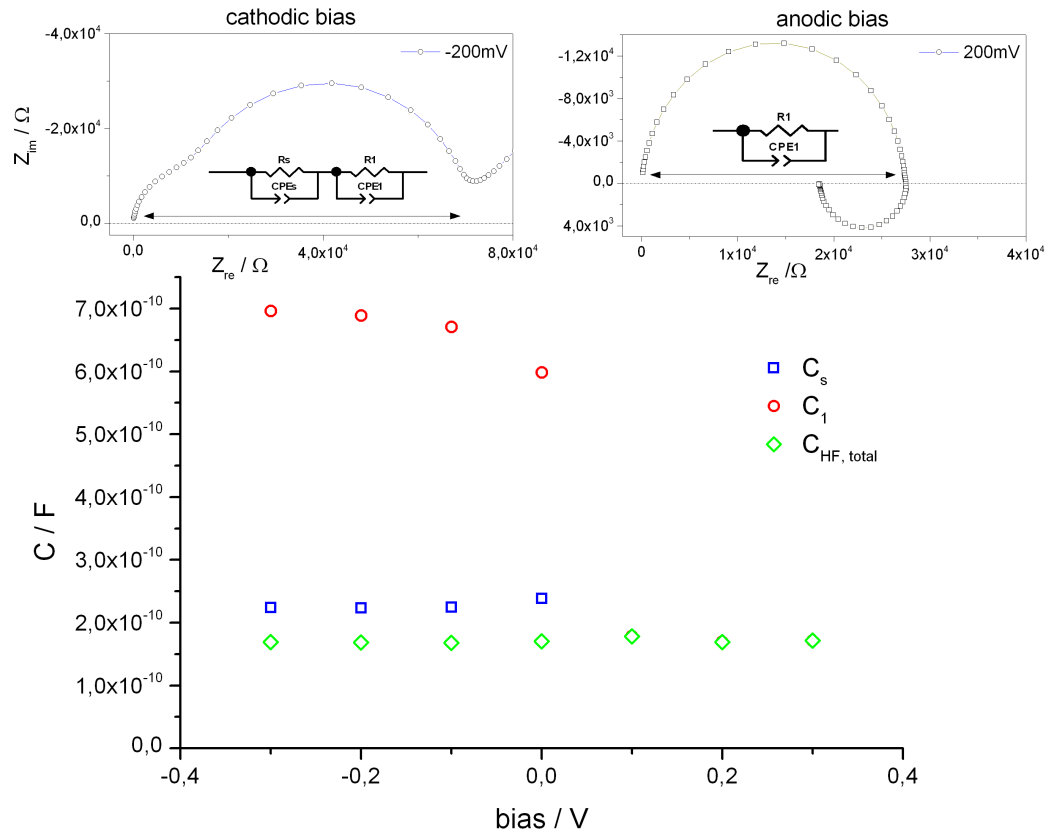


Figure 5.26

Fig. 5.26: A comparative illustration of all analyzed capacitance values for the 413 nm sample. Additionally, exemplary impedance plots for the anodic and the cathodic range as well as the used equivalent circuit should emphasize the observed behavior under applied bias (600°C T_{set}).

The same analysis was performed for two other samples, and qualitatively the same capacitance behavior is observed (see Fig. 5.27). Moreover, on the basis of these 3 layers, a thickness dependent investigation of C_1 and C_S is possible. In the case of the thickest STO layer (413 nm), the capacitance for the shoulder feature makes the bigger contribution to $C_{HF,total}$ (even though its resistance is the smaller one). Thus the increased separation of the high frequency shoulder monitored in impedance spectra is confirmed by the results. With decreasing layer thickness the "importance" of this shoulder with respect to the capacitance slightly vanishes, and for the 125 nm layer C_1 and C_S have more or less the same value, which comes along with a less pronounced separation of these two high frequency fractions in the monitored impedance spectra. The capacitance values at 0 V bias and 50 mV for the 125 nm show

deviations from the trend but this could be due to the almost completely vanished shoulder feature and thus unreliable fits.

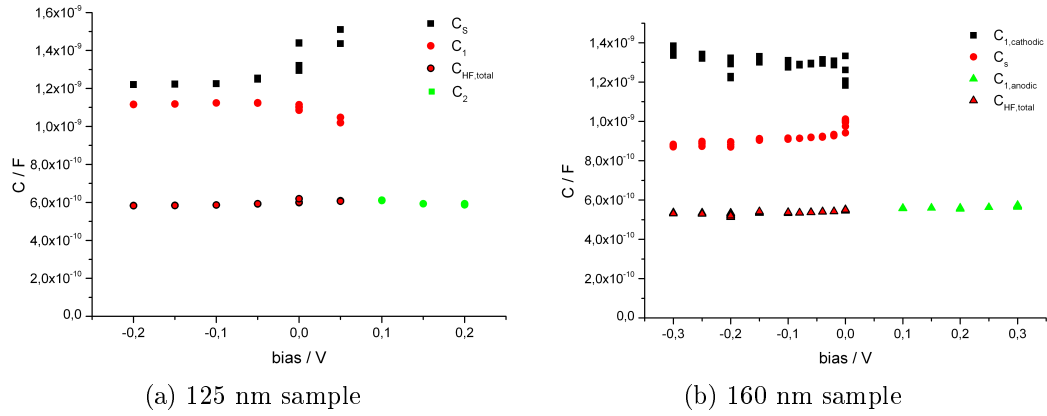


Figure 5.27

Fig. 5.27: Capacitance evaluation over the entire bias range for 2 samples with different thickness ((a) 125 nm (634°C actual temperature) and (b) 160 nm (700°C T_{set})).

As it was already mentioned in Sec. 5.1 the question about the origin for this additional shoulder is still not solved. From the point of the evaluated capacitances C_1 and C_S , it can be completely excluded that the shoulder is the response of a bulk fraction, due to the fact that both values are too large (as is the corresponding resistance).

In addition to the bias analysis the capacitance values of $C_{HF,total}$ were plotted against temperature. The results are depicted in Fig. 5.28, and reveal only a minor temperature dependence of the capacitance for both samples shown and is in accordance with a Curie-Weiss-type behavior. This further supports the mechanistic interpretation of $C_{HF,total}$ as the geometrical capacitance of the deposited STO thin layers.

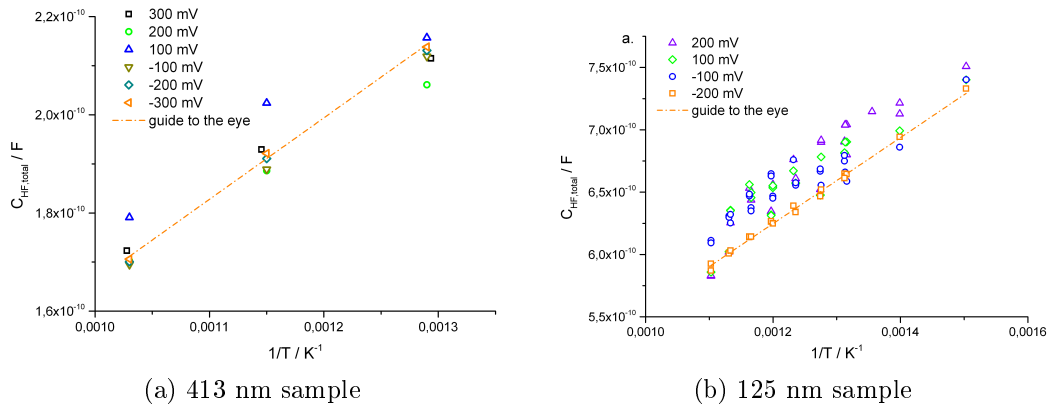


Figure 5.28

Fig. 5.28: Temperature dependence of $C_{HF,total}$ for 2 samples with different thickness ((a) 413 nm and (b) 125 nm).

• Analysis of C₂ for the anodic and cathodic bias regime

Besides the capacitances evaluated for the high frequency, the capacitance of the low frequency arc (semicircle or loop) was analyzed. The obtained capacitance values were more or less 3 orders of magnitude higher than the values of C_{HF,total}. The values obtained for the constant phase element (CPE) were again converted into a capacitance value by using Eq. 5.2 and the evaluated n-values were in the range between 0,7 and 0,85.

Analysis of the capacitance received from the low frequency arc, revealed a distinct bias dependence of C₂ as it is shown in Fig. 5.29, although a monotonous trend can not be always found (see the 160 nm sample). This may be also correlated to the thickness of the investigated layer.

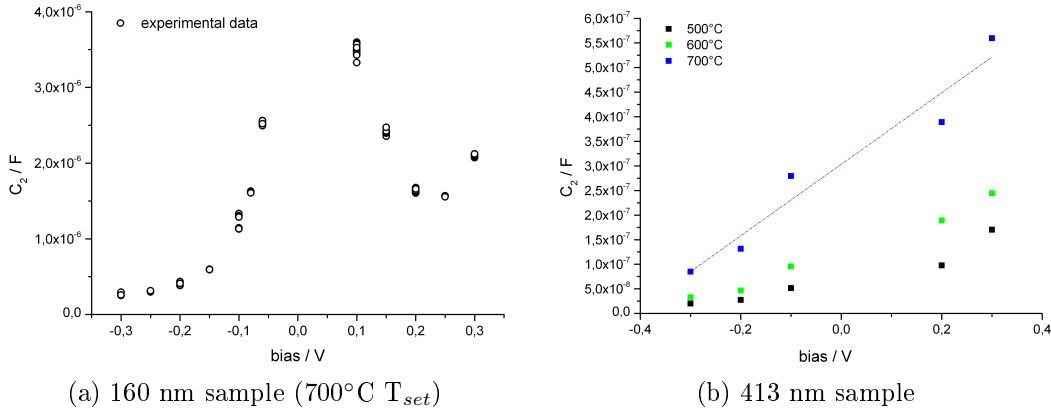


Figure 5.29

Fig. 5.29: Low frequency capacitance C₂ plotted against bias.

Moreover, C₂ shows a dependence on temperature (see Fig. 5.30). However, this is not really surprising, considering the discussion in Sec. 5.2.1. Therein, it was shown, that according to the model R_{ion} and ΔR_{slow} affect C_{1,anodic}. Both are temperature dependent and therefore the low frequency capacitance has to show a dependence on temperature as well, which could be proven by this analysis: It is almost Arrhenius-type with an activation energy of 0.8 eV (125 nm sample) and of around 0.4 eV (413 nm sample).

Nevertheless, as it was already discussed in Sec. 5.2.1, an interpretation of the measured low frequency capacitance is not trivial at all, due to the complex influence of ionic migration under field. Furthermore a capacitance value in the range of 10⁻⁴F/cm² is considerably too high to be caused by a double layer response. According to our model we can at least estimate the ratio of the ionic resistance R_{ion} and ΔR_{slow} for a typical value of C_{el} (≈2·10⁻⁵ F/cm²):

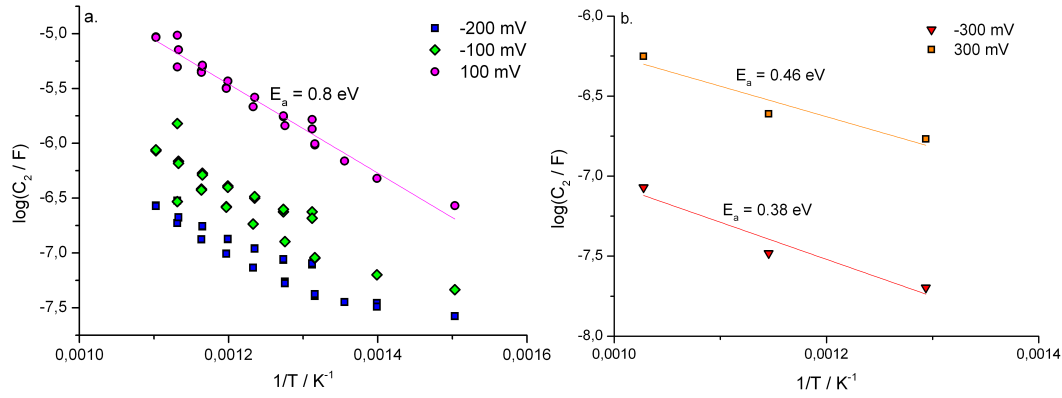


Figure 5.30

Fig. 5.30: C_2 for the 125 nm sample (a) and the 413 nm sample (b) are analyzed in terms of temperature dependence.

R_{ion} is almost two orders of magnitude larger than ΔR_{slow} and since ΔR_{slow} and $R_{STOfilm,fast}$ are in the same order of magnitude also a much larger ionic resistance compared to the electronic one is confirmed (this was an assumption in our model). Since C_2 is proportional to $\frac{R_{ion}}{\Delta R_{slow}}$ its activation energy should be roughly the difference between those of the two resistors. The measured value of 0.8 eV to 0.4 eV for C_2 and 1.6 eV for ΔR_{slow} thus suggests an activation energy of around 0.8 eV to 1.2 eV for R_{ion} which is highly realistic in STO.

5.2.3 Comparison of all observed variations obtained by AC measurements under bias

Although most of the measured samples showed loops in the anodic and second semicircles in the cathodic regime, some samples exhibit deviating characteristics. In this section of the work, we will focus on these variations and discuss the potential reasons.

In Fig. 5.31 impedance data obtained for a 150 nm thin layer are illustrated. This sample shows more than one deviation from the "classical" behavior, and therefore serves as an example to point out possible changes.

One of the most frequently appearing changes could be observed for the cathodic regime. Instead of a second semicircle and an increasing resistance for the high frequency range, a loop was monitored (see Fig. 5.31(c) and (f)). Moreover, in the case of this sample $R_{HF,total}$ untypically decreases with increasing negative bias voltage. The impedance spectra depicted in Fig. 5.31(a) characterizes another variation monitored in rare cases. Up to now loops were found only in the positive and semicircles in the negative bias range. However,

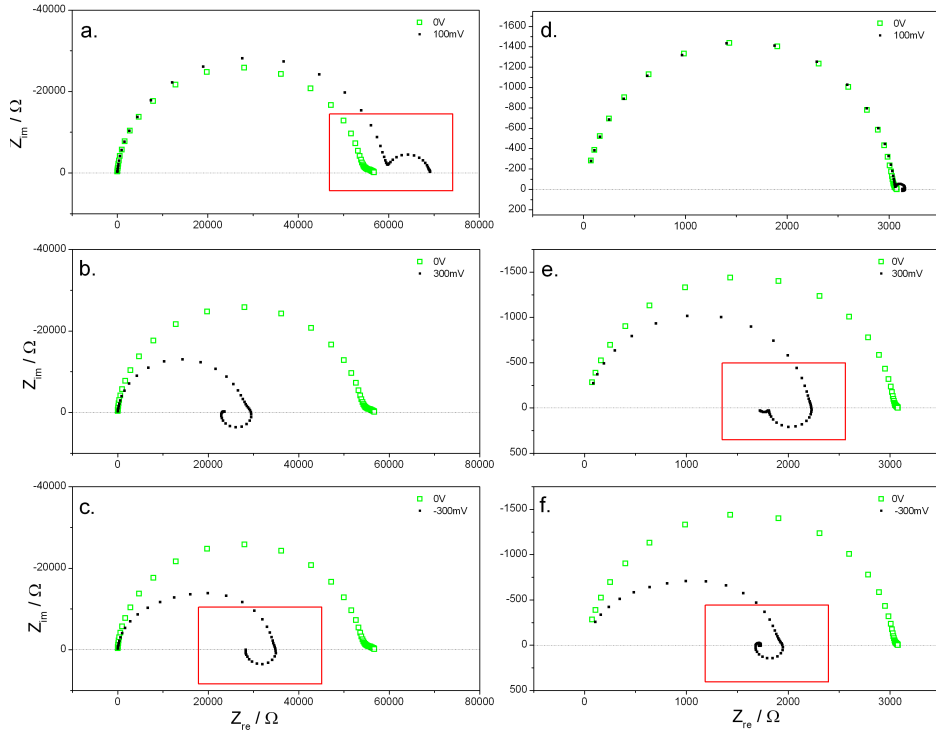


Figure 5.31

Fig. 5.31: Image of impedance spectra of a 150 nm film for two different temperatures and three different bias voltages, in (a–c) impedance data for 556°C are shown, and compared with data monitored at 662°C (d–f).

for some cases a transition between these two features takes place in one and the same bias regime. The same behavior was observed for the 157 nm sample as it is shown in Fig. 5.32(c and d). This shift will be mentioned again in the current-voltage characteristic discussion, because it also manifests itself in the slope of the U-I curves. Comparing the results for the illustrated two temperatures (see again Fig. 5.31(a) and (d)), it has to be noticed that for the higher temperature the semicircle shrivels to a little artifact.

Staying at the same diagram one additional part of the spectra needs to be mentioned. For the 662°C measurement under positive bias a second loop at the last recorded frequency point could be observed. This additional feature was observed in different specification for different samples, e.g. the top spectra in Fig. 5.33. On the other hand, spectra with two features in the high frequency part and a loop in the low frequency part could be found too (see again Fig. 5.33). In this case it has to be pointed out, that the second feature in the high frequency part is not the "classical" shoulder, because it appears in the middle frequency range.

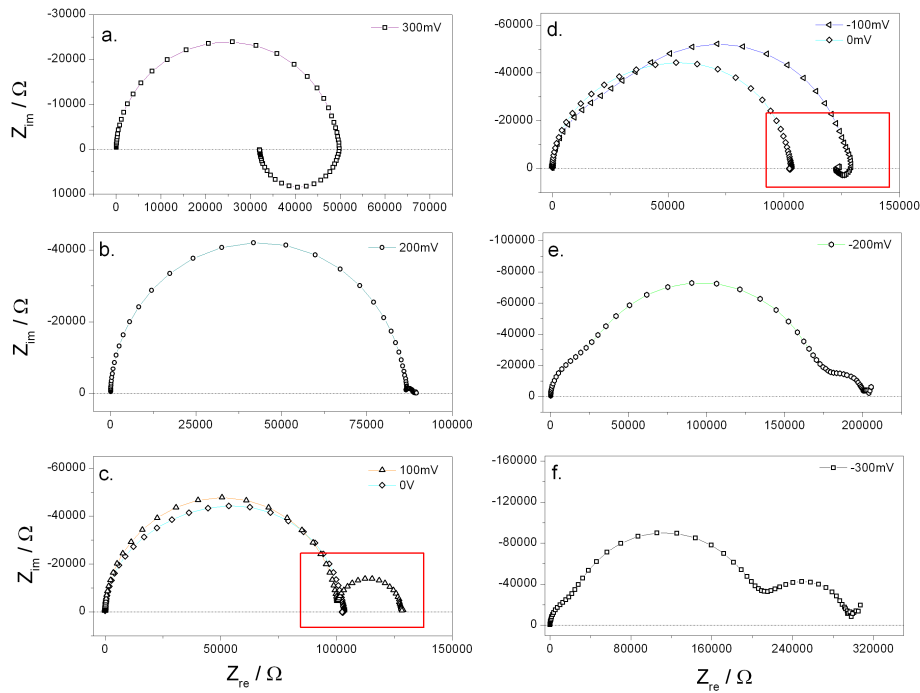


Figure 5.32

Fig. 5.32: Impedance spectra for different bias voltages measured on a 157 nm sample at 600°C (T_{set}). The red rectangles mark the variations observed.

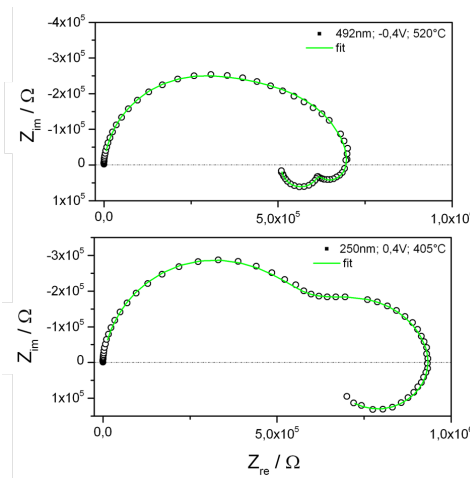


Figure 5.33

Fig. 5.33: Impedance plots for two different layers, which exhibit deviating characteristics under bias.

The variation of layer behavior upon bias was also analyzed in terms of a possible thickness dependence, but the occurrence of the mentioned deviation from "classic" behavior were completely random. We assume that deposition and electrode preparation are subjected to small fluctuations and therefore are the origin for the observed variations.

5.2.4 Kramers-Kronig test of the measured impedance data

Impedance spectroscopy is a strong tool to investigate electrochemical processes in materials like perovskite oxides. However, wrong interpretations due to defective data are certainly possible. To exclude such bad data, the linear Kramers Kronig transform test was applied to the measured impedance data. For testing the data the program KK test version 1.01 by B.A. Boukamp was used.^[101,102] To achieve information about the reliability of measured impedance data the differences ($\Delta_{re,i}$ and $\Delta_{im,i}$ = residuals) between data and its KK compliant fit have to be calculated. The residuals are described as follows, and are plotted against frequency.

$$\Delta_{re,i} = \frac{X_{re,i} - X_{re,(KK)}}{|X_{(KK)}|} \quad \text{and} \quad \Delta_{im,i} = \frac{X_{im,i} - X_{im,(KK)}}{|X_{(KK)}|} \quad (5.10)$$

$X_{re,i}$ and $X_{im,i}$ describe the real and imaginary part of the experimental data, whereas $X_{re,(KK)}$ and $X_{im,(KK)}$ stand for the real and imaginary part of the KK-compliant. $|X_{(KK)}|$ is the magnitude of the Kramers-Kronig transform. The obtained residual distribution around the $\log(f)$ axis gives information about the quality of the data. Randomly spread values are a sign for a good match between experimental data and the KK compliant. On the other hand, systematic deviations indicate that systematic errors, e.g. slow changes in temperature, aging of the sample or variations of the measuring set-up have to be taken into account.

In Fig. 5.34 the investigated polycrystalline bulk sample is compared with data achieved on a thin layer without external applied bias voltage. The residual plot for the thin film shows only slight random scattering within the range of $\pm 0,25\%$. In the range of the onset of the grain boundary arc for the bulk sample the scattering is a little bit more pronounced. This low noise of the data allows the conclusion that systematic errors can be more or less excluded.

Because of the fact, that a considerable part of this thesis is dealing with the investigation of STO films under an applied bias voltage, data obtained from such experiments were also tested by means of Kramers-Kronig. The results are depicted in Fig. 5.35. Data monitored under cathodic bias (-200 mV) and a resulting second semicircle shows again only random noise in the measured

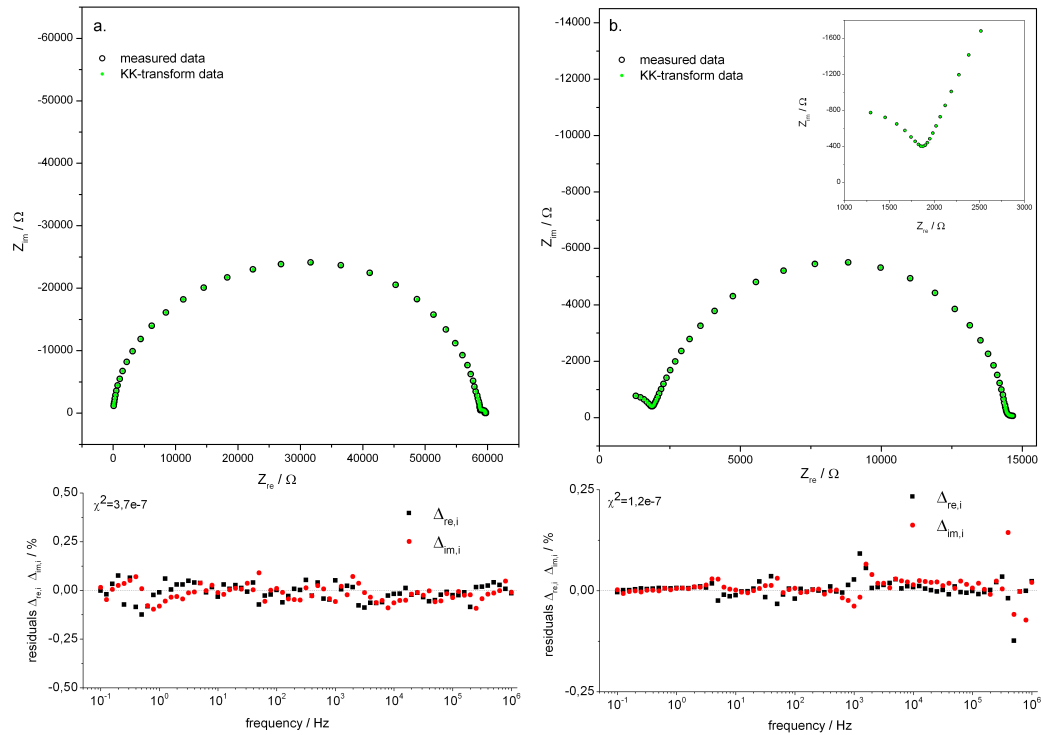


Figure 5.34

Fig. 5.34: Kramers-Kronig analysis for the polycrystalline bulk sample (b) and a thin layer (413 nm) (a) without an external applied bias at 454°C and 700°C (T_{set}), respectively.

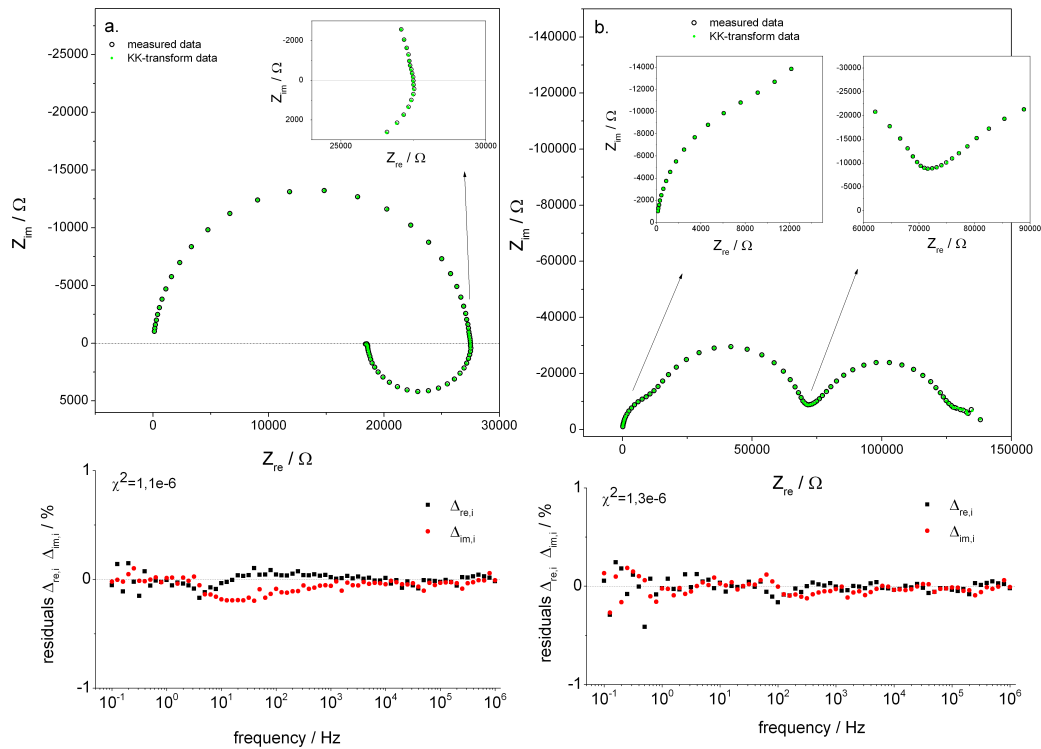


Figure 5.35

Fig. 5.35: Performing the Kramers-Kronig test for a 413 nm sample measured under +200 mV applied bias (a) and -200 mV applied bias (b). Measured at 700°C (T_{set}).

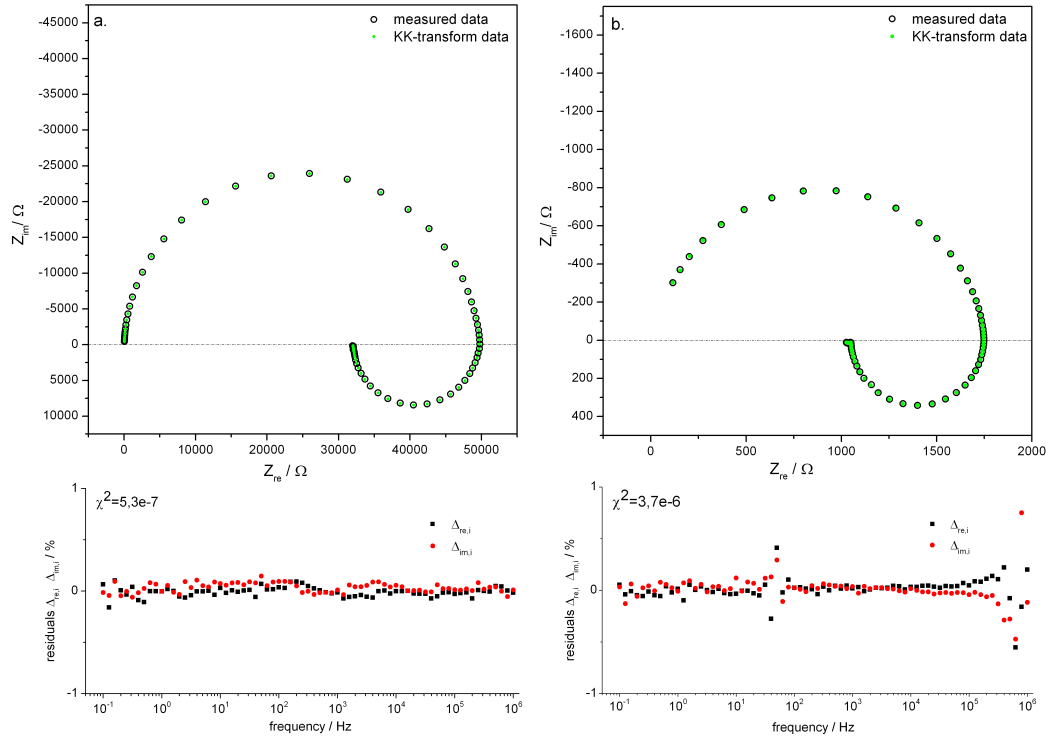


Figure 5.36

Fig. 5.36: Performing the Kramers-Kronig test for a 157 nm sample (600°C, T_{set}) (a) and a 160 nm sample (700°C, T_{set}) (b) measured under +300 mV applied bias.

frequency range. On the other hand, the anodic bias (+200 mV) becomes interesting due to the intersection of the x-axis. Particularly for the 413 nm layer exactly this intersect of the real axis provides non-random deviations in the residuals plot. To check whether this observed feature is always found, two further measurements performed in the anodic range were tested (see Fig. 5.36). The residuals plot for the sample shown in (a) do not show any distinct changes in the randomness of the data set even in the frequency range of the intersection. For the other sample, depicted in (b) the scattering of the residuals becomes slightly more pronounced in the frequency range of interest. Those, however are most probably caused by the very small imaginary part of the impedance in this range. Altogether on the basis of the performed Kramers-Kronig test irreversible changes of the thin films during impedance measurements could be excluded.

Chapter 6

Results and Discussion: Partial Pressure Measurements on Fe-doped SrTiO₃ Thin Films under Oxidizing Conditions

The experiments were performed on two different layers (157 nm and 413 nm) and at three different temperatures (675°C, 560°C and 475°C). The gas composition was changed from 100% oxygen to air and then to 1% oxygen. Because of the large electrical parameter range employed in each case, only a small range of the Brouwer diagram was investigated. To check reproducibility of the relaxation behavior and the equilibrium conditions, measurements consisted of several cycles, as it is illustrated in Fig. 6.1 were performed. The step in time is caused by a stop of the measurement overnight and a new start on a different electrode. Even though a small step in the data occurs after changing the electrode, the changes due to p_{O_2} are completely reproducible and reversible, irrespective of the direction from which the change in the ambient atmosphere was made.

In Fig. 6.2 impedance data are shown for both samples (157 nm and 413 nm), three temperatures (675°C, 560°C and 475°C), and different partial pressures, all without applied bias. It is remarkable that 100% oxygen atmosphere leads to exactly the same feature (shoulder) at the highest frequency points as a negative bias applied to the same sample in air (see below). This suggests that the high frequency shoulder is not an effect of the inhomogeneous vacancy distribution in the sample upon bias, but an effect of a high chemical

potential of oxygen in the entire sample (for 100% oxygen without bias) or at least a part of the sample. Please note again that negative bias is applied to the reversible electrode and thus enhances the chemical potential near to the other electrode. In the lower frequency range the second semicircle, which is observed for negative applied bias is missing in data obtained in pure oxygen. Switching to 1% oxygen, the high frequency semicircle becomes ideal, which resembles the effect of a positive bias voltage. Again no loop or second semicircle was found in the lower frequency part (without bias). This again suggests that the low frequency features are kinetically induced rather than caused by thermodynamic changes, in accordance with the model in Sec. 5.2.

Figure 6.1

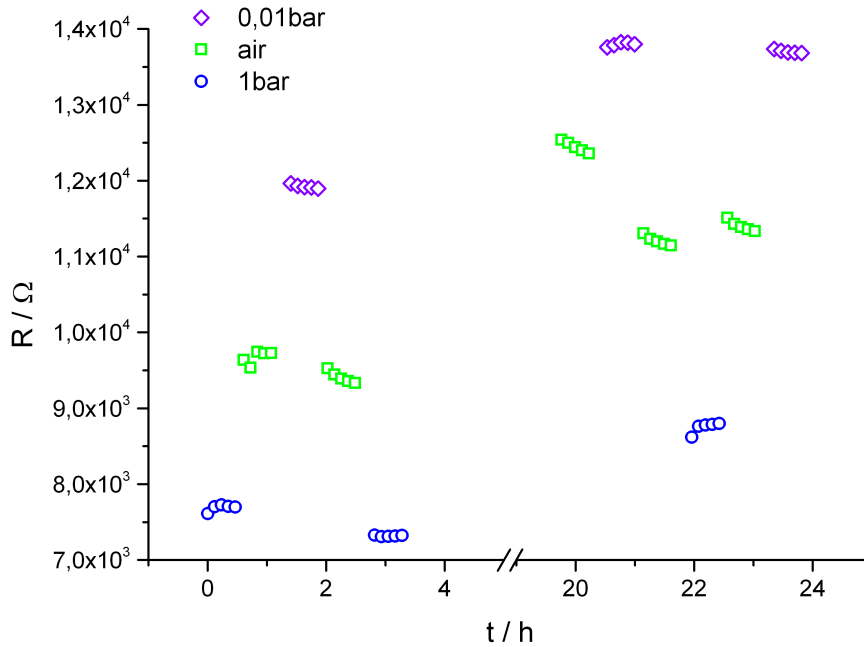


Fig. 6.1: Resistance measured during partial pressure cycles.

From the high frequency arc of the measured impedance spectra, resistances were extracted in the same way as before, i.e. by one or two R-CPE elements. The conductivities determined from $R_{HF,total}$ are shown in Fig. 6.3. From the plotted data in Fig. 6.3 and Fig. 6.4 only a very small slope, if any can be observed (with the exception of the lowest temperature in oxygen, 157 nm layer). This suggests that the material is close to a plateau or the minimum of the conductivity vs. p_{O_2} plot. This is in accordance with a shift of the minimum to higher p_{O_2} in nanocrystalline STO, caused by overlapping space charges^[52]. By taking other literature data into account^[61–63], it would not

be unlikely that with decreasing layer thickness the minimum shifts further to higher p_{O_2} values.

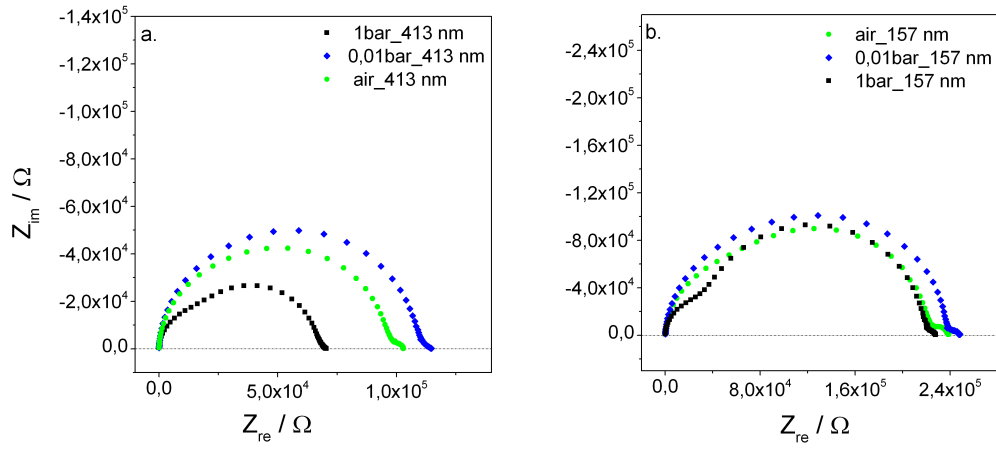


Figure 6.2

Fig. 6.2: Impedance data for the measurements under variable oxygen partial pressure (100% O_2 , air and 1% O_2) for 413 nm sample (a) and 157 nm sample (b) at 600°C (T_{set}).

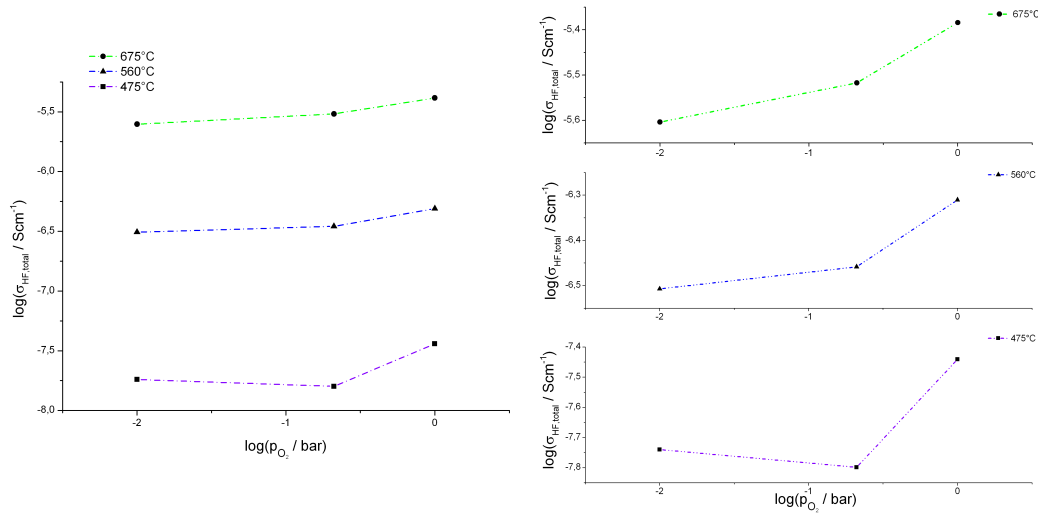


Figure 6.3

Fig. 6.3: Partial pressure dependent conductivities $\sigma_{\text{HF},\text{total}}$ of the 157 nm layer for the three temperatures 675°C , 560°C and 475°C .

In addition to the evaluation of the partial pressure dependency the data was plotted in an Arrhenius-diagram. The activation energy for both samples can be extracted from Fig. 6.5. Compared with data gained from measurements under air, the values for pure oxygen and 1% O_2 deviate only slightly. All calculated activation energies are more in line with literature data of grain boundaries rather than bulk values.

After reaching equilibrium in a new p_{O_2} , measurements under applied bias were performed. Impedance data for the 413 nm sample are shown in Fig. 6.6

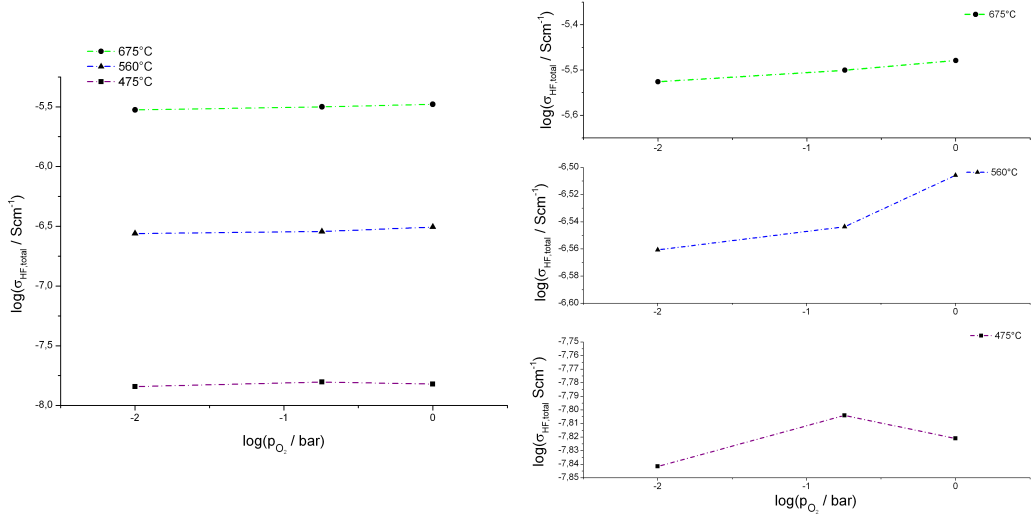


Figure 6.4

Fig. 6.4: Partial pressure dependent conductivities $\sigma_{HF,total}$ of the 413 nm layer again for the three temperatures 675°C, 560°C and 475°C.

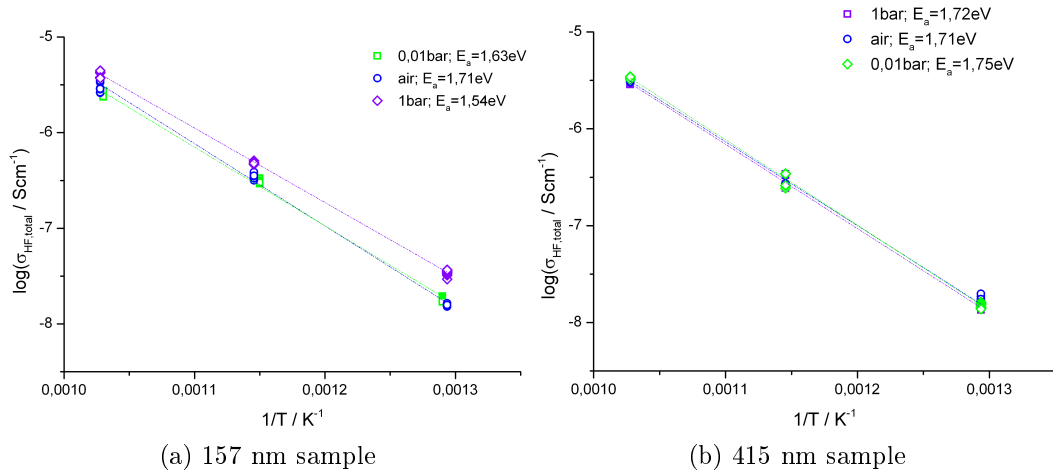


Figure 6.5

Fig. 6.5: Arrhenius plots for a 157 nm sample (a) and a 413 nm sample (b), the results for air, 100% oxygen and 0,1% oxygen are compared.

and the data for the thinner layer is shown in Fig. 6.7. A detailed analysis of these data is not trivial, due to the fact, that we have to deal with a changed partial pressure as well as an additionally applied DC voltage. A look at the spectra for anodic and cathodic bias at 500°C for the 413 nm sample illustrates general trends. Impedance data recorded under 100% O_2 and negative bias have a much more pronounced shoulder (HF range) than the data for 1% O_2 . Moreover, the bias generates the well-known second semicircle at low frequencies, while the loop becomes much less pronounced in 1% O_2 . The resulting data for positive bias and 100% O_2 reveal a distinct loop (LF range). The shoulder, which was observed for the negative bias, is absent in this case. For the thinner layer (157 nm) applying a negative bias voltage in the oxygen

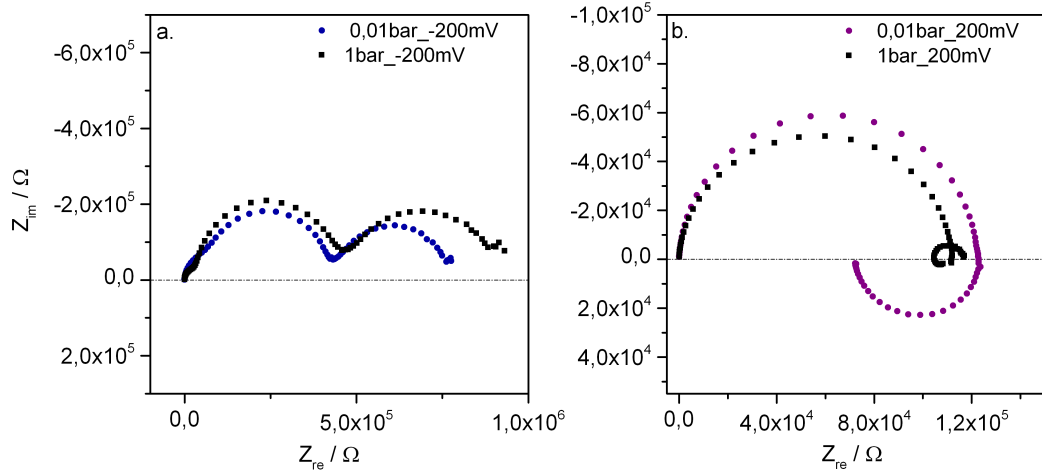


Figure 6.6

Fig. 6.6: Impedance data for the 413 nm layer under different partial pressure (100% O₂ and 1% O₂) and additionally applied bias voltage (−200 mV (a) and +200 mV (b)) at 600°C (T_{set}).

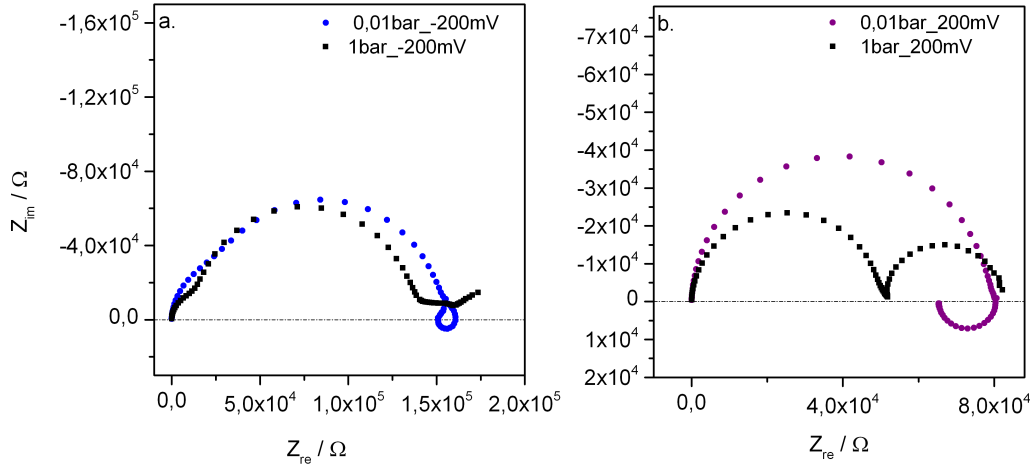


Figure 6.7

Fig. 6.7: Impedance data for the 157 nm layer under 100% O₂ and 1% O₂ with an applied bias voltage of −200 mV (a) and +200 mV (b) at 600°C(T_{set}).

poor atmosphere leads to a small shoulder at high frequencies and a loop in the smaller frequency range. Changing the p_{O₂} to high values causes the appearance of second semicircles. Regarding the positive bias case, the oxygen poor atmosphere leads to a more or less ideal semicircle for the HF range, followed by a loop at low frequencies. On the other hand the oxygen rich situation with positive bias produces a second semicircle instead of the loop.

The data, achieved under 100% O₂ and 1% O₂ was evaluated by comparing the results with measurements performed in air. In Fig. 6.8(a) the bias dependent capacitance for the high frequency regime (C_{HF,total}) is plotted, and it can be seen that there is no dependency upon bias. Further it needs to be emphasized, that the capacitance values do not show any step when switching from negative

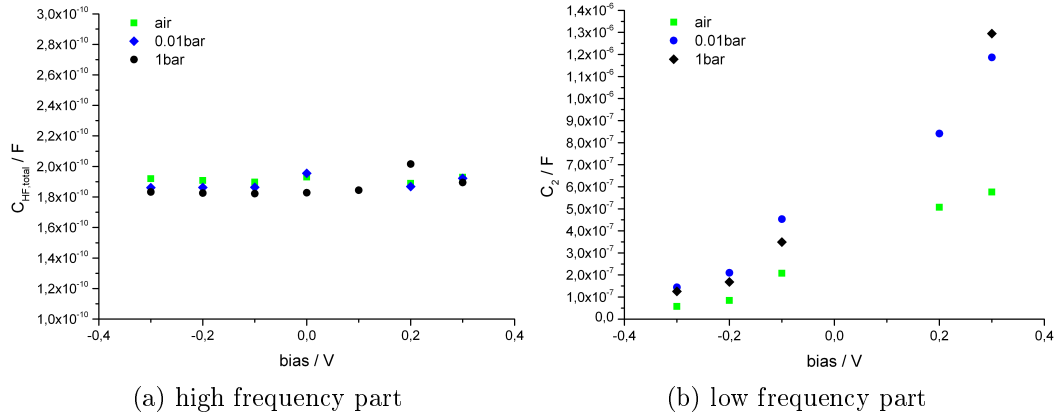


Figure 6.8

Fig. 6.8: Capacitance values of the high (a) frequency part of the spectra and the low (b) frequency part are shown against bias for the thicker sample (413 nm) at 600°C (T_{set}).

Bias voltage [mV]	$\epsilon_{r, air}$	$\epsilon_{r, 100\%O_2}$	$\epsilon_{r, 1\%O_2}$
0	128	121	130
300	128	126	127
-300	128	122	124

Tab. 6.1: ϵ_r values compared for 0 V bias in air with the values obtained for changed partial pressure and applied bias (300 mV and -300 mV respectively)

to positive bias. This is not only the case for the values obtained in air, but is also valid for the two other p_{O_2} situations. These capacitance values were used to calculate the relative dielectric constant (ϵ_r) for the SrTiO₃ thin films, and the results are illustrated in Tab. 6.1. The values are in the range of typical bulk ϵ_r -values and therefore support the assumption that $C_{HF, total}$ reflects the geometrical capacitance of the Fe-doped SrTiO₃ thin films.

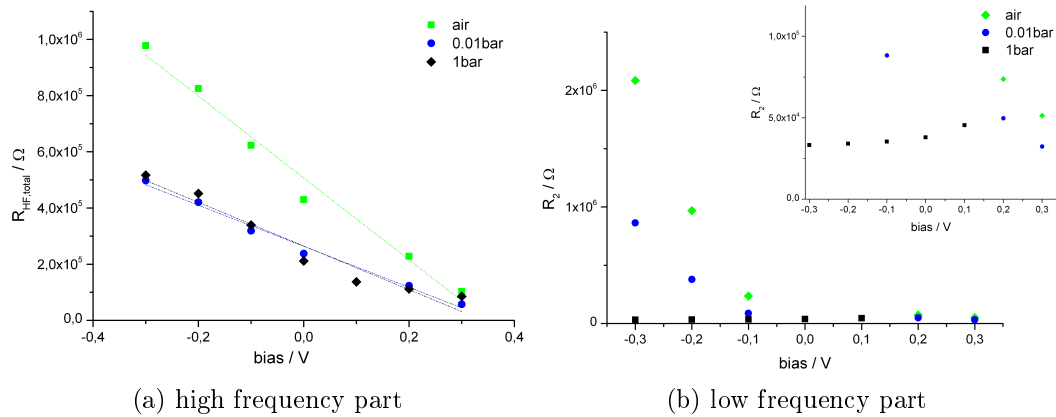


Figure 6.9

Fig. 6.9: The resistance of the 413 nm sample is also evaluated for the high (a) and the low frequency (b) part of the impedance spectra, for three different p_{O_2} (600°C, T_{set}).

In Fig. 6.9 it is shown how the resistance depends on the applied bias. The high frequency resistance $R_{HF,total}$ consists of two fractions (shoulder and semicircle) in the case of negative applied voltage. A clear trend of these values over the investigated bias range can be observed for all three ambient atmospheres. The low frequency resistance R_2 , on the other hand, shows an increase for negative bias when exposed to air or 1% O_2 but little bias dependence in 100% O_2 . However, for final conclusions further dependent p_{O_2} data are required.

Chapter 7

Results and Discussion: Current-Voltage Behavior of Thin Fe-doped SrTiO₃ Films Investigated in Two Different Time Modes

In the present thesis DC measurements were used as a second powerful tool to investigate transport properties of charge carriers in SrTiO₃ thin films. The obtained results are considered in the context of a multitude of other investigations made on single crystalline or polycrystalline STO bulk material by means of DC experiments.^[18,33,36–38,40,41,44,45,47,81] Depending on the investigated sample, set-ups and the applied DC voltages, the range of results which can be found in literature goes from achieving information on the partial ionic conductivity (Wagner-Hebb polarization) to a better understanding of resistance degradation in undoped and acceptor doped SrTiO₃ as it was already mentioned in Chapter 2.3.

Three different approaches were employed to achieve a clearer picture of defect chemical transport and migration processes going on in thin films under an applied electrical field: slowly measured U-I curves, U-I curves with a fast recording rate and time-dependent polarization and relaxation studies. The latter are shown in Chapter 8. The systematic study on Fe-doped SrTiO₃ thin films was performed for a voltage range from -500 mV to $+500$ mV. The two parameters temperature and time were adapted for each experiment. Regarding the parameter time, a clear separation into two types of current-voltage

experiments can be made. As a consequence, the presentation of monitored data and the discussion of obtained results is split into two parts.

"Slow" U-I curves, with the focus on reaching steady state conditions for each measuring point, were performed in a temperature range between 270°C and 650°C. Variations in equilibration time due to temperature changes were taken account of by an appropriate adaption of measuring time. Therefore U-I measurements were conducted within a range of 3 to 12 hours for one U-I cycle.

In the temperature range between 270°C and 425°C **"fast" U-I curves** were also measured, with a recording time in the range of seconds. In contrast to the slow current-voltage measurements, the starting voltage is an essential factor in the case of fast measured U-I curves. Measurements with the starting point at 0 V and ± 400 mV bias voltage were therefore performed.

7.1 U-I characteristics: Slow measurements

The term "slow DC measurements" denotes measurements that were performed on a timescale of hours. This extended procedure ensures that the investigated sample could reach the steady state condition for each measured voltage point. In the case of large (bulk-like) samples the time required to reach steady state may be easily extended up to 10 or even 100 hours^[103], depending on the material, temperature, thickness and the magnitude of voltage investigated. In the case of thin films, the necessary time is drastically decreased due to the considerably reduced volume, and the measuring time of an entire U-I curve with continuously changing bias voltage (between ± 500 mV) was in the range of 3 to 12 hours.

The most important result that could be found for slow U-I curves is exemplarily demonstrated in Fig. 7.1. The starting point for this measurement was set to +500 mV. After applying the appropriate bias, the sample needs an extended time period to adjust to the changed condition. This is indicated by the current increase (in the Fig. indicated in cyan colored symbols). In the following course of the experiment, the slow U-I curve represents a permanently changing steady state charge carrier distribution. The reason why the steady state curve is reached at around 480 mV (valid for this sample under the used

conditions) is the fact that the voltage was continuously changed rather than stepwise. After the initial polarization the curve could be reproducibly cycled, indicating the true steady state character. This approach of the steady state is discussed in detail in Chapter 8.

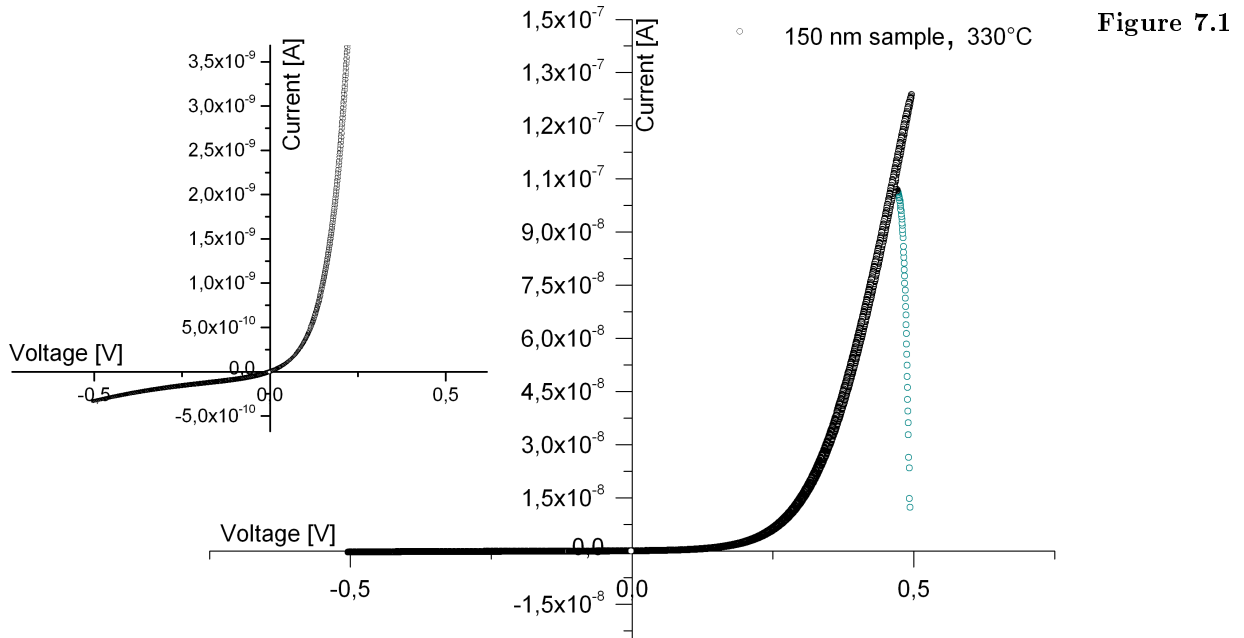


Fig. 7.1: Slow current-voltage curve monitored for a 152 nm at 330°C (true temperature). The measurement was performed in the "Micro-Macro" set-up. The initial change of the current is indicated in cyan colored symbols.

In the anodic range the curve showed a distinct current decrease with decreasing voltage. Furthermore, the curve passes the x-axis according to expectations in the origin of the graph. At first it seems as if the curve in the cathodic range is characterized by a "limiting current" like behavior. A closer look reveals that in the first 150 mV the curve indeed tends to approach constant current values with increasing voltage, but in the range of -300 mV a minor bend can be observed. Beyond this point, the current is again slightly increasing with increasing bias voltage. It should be emphasized that the current measured at -500 mV is 3 orders of magnitude smaller than the appropriate value measured at i.e. $+500$ mV.

Impedance measurements performed in the same temperature regime but on another sample confirmed these strong differences in resistance for positive and negative bias; in Section 5.2 the temperatures were much higher. The spectra are depicted in Fig. 7.2. Because of the tremendously increasing resistance values under cathodic bias it was not always possible to monitor the entire

spectrum in a reasonable time. Still the distinct difference between R(−300 mV) and R(+300 mV) is obvious.

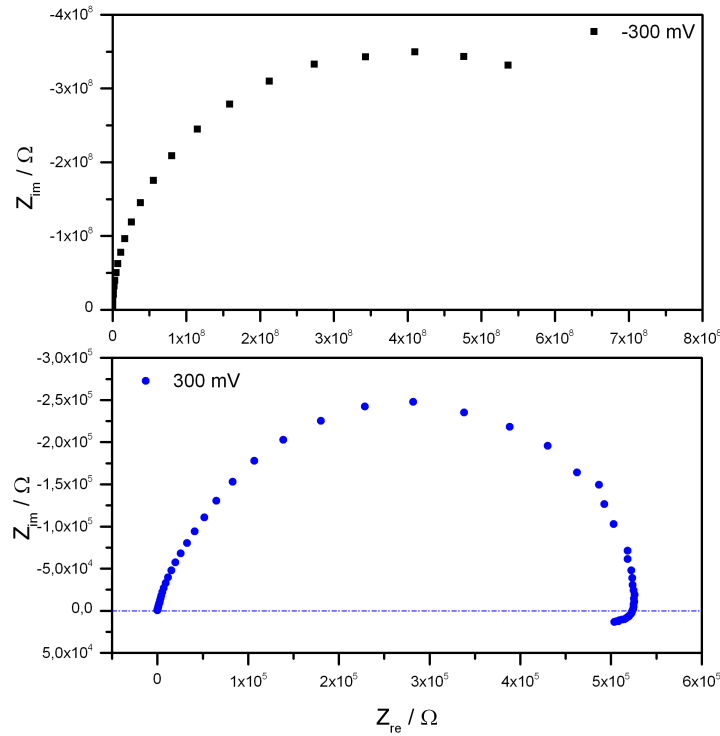


Figure 7.2

Fig. 7.2: Impedance spectra measured at 375°C (set temperature) for a 110 nm sample. Comparison of the spectra monitored under −300 mV and +300 mV, with a difference in resistance values of about 3 orders of magnitude.

In several cases the curve was also started at −500 mV, with the result of an almost complete overlap of the observed data.

In literature^[104] different reasons for the non-linearity of U-I curves measured on SrTiO₃ single crystals are discussed. Besides a redistribution of oxygen vacancies due to an oxygen blocking effect at an interface, a changed performance due to space charge zones is mentioned. Both aspects may also be reasonable explanations for the behavior observed in the investigated thin films.

Redistribution of oxygen vacancies is clearly occurring during the DC measurements. The continuously changing bias voltage consequently also continuously changes the $V_{\text{O}}^{\bullet\bullet}$ distribution (= stoichiometric polarization). By applying +500 mV bias voltage to the sample, the LSC microelectrode becomes the anode and thereby the Nb-doped SrTiO₃ substrate becomes the cathode. This causes an electromigration of oxygen vacancies towards the blocking Nb-STO electrode. For an oxygen blocking LSC electrode it would leave behind a $V_{\text{O}}^{\bullet\bullet}$ depleted region in the vicinity of the anode. For a reversible LSC electrode

the corresponding vacancy concentration would be fixed. Waser *et.al.*^[37,38,38] discussed the blocking electrode case in detail as part of his work on degradation phenomena in SrTiO₃ ceramics and single crystals. During the voltage scanning the oxygen vacancy concentration is "slopping" back and forth in the investigated volume. Because of the fact that enough time is available, the reaction (= charge carrier migration monitored as current) can follow the action (= DC voltage change). This point of view suggests that we can simply consider the thermodynamics of the system, because the adjusting of the local equilibrium in steady state is only determined by the applied voltage U. This measuring mode therefore results in a situation, for which in each voltage point a new thermodynamically determined charge carrier distribution is monitored.

• **Analysis of slow U-I data**

For the analysis of the recorded U-I curves we have to reconsider the used sample set-up. Fe-doped SrTiO₃ is sandwiched between LSC (at least partially reversible for the ionic current) and Nb-doped STO (blocking for the ionic current). In the ideal case of one electrode being blocking for oxygen vacancies and the other side being fully reversible for these charge carriers, the approach made by Wagner (see Eq. 7.1) can be used.

$$i_{eon} = \frac{k_B T}{\alpha e L} \left\{ \sigma_n(0) \left[\exp\left(\frac{\alpha e U}{k_B T}\right) - 1 \right] + \sigma_p(0) \left[1 - \exp\left(-\frac{\alpha e U}{k_B T}\right) \right] \right\} \quad (7.1)$$

$$i_{eon} = j_n(e^{R_n \cdot U} - 1) + j_p(1 - e^{R_p \cdot U}) \quad (7.2)$$

We used an approximation of the Wagner-Hebb equation to fit the measured data. Results obtained for a 152 nm sample at 429°C by using Eq. 7.2 are depicted in Fig. 7.3. R_n and R_p are the abbreviation for $\frac{\alpha_{n,p} e}{k_B T}$ and j_n as well as j_p stands for the prefactor $\sigma_{n,p} \cdot \frac{k_B T}{e L \alpha}$. R_n and R_p are used to accommodate the case that the α -values for the anodic and the cathodic are not equal and not exactly 1, as it is the case for the ideal Wagner-Hebb approach.^[80,81] Because of a changing α -value the prefactor is not clearly defined, thus j_n and j_p are introduced.

Classical Wagner-Hebb behavior, however, can be excluded due to the fact that we are dealing with thin layers instead of bulk material. The electrochemical performance of thin layers differ from results obtained on bulk material, which

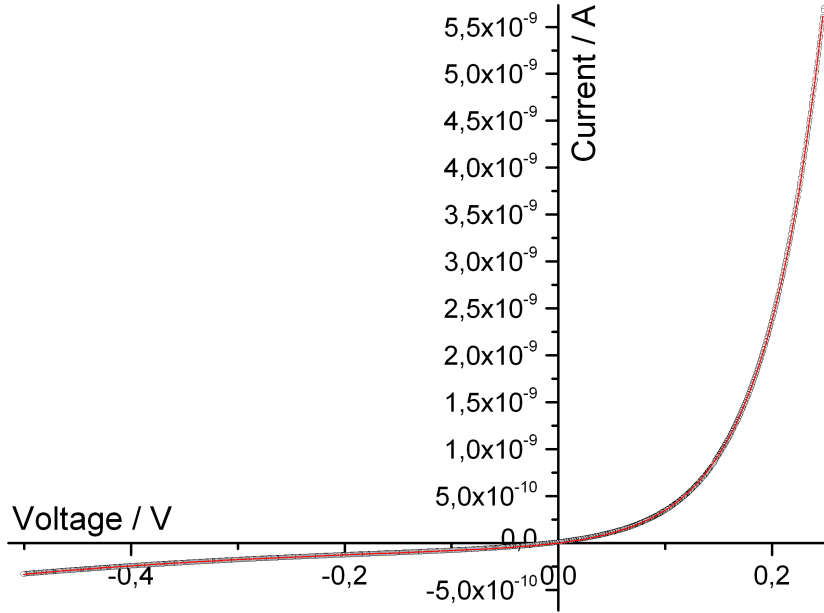


Figure 7.3

Fig. 7.3: Slowly measured U-I curve and the appropriate fit (Eq. 7.2) illustrated for a 152 nm sample at 429°C.

could be confirmed by more or less all performed experiments. As a possible reason the increased density of dislocations was considered. Furthermore, the used electrode material (LSC) deserves closer attention. As it was mentioned above, in the ideal case LSC should be fully reversible for oxygen. Consequently the oxygen chemical potential is pinned at this side of the specimen, due to the small polarization resistance of the nicely ion conducting electrode. However, nonidealities in the electrochemical performance of LSC could appear easily, resulting in a deviation from the pinned oxygen chemical potential at point $x=0$ (see again Sec. 2.3, Fig. 2.11). Thus a modeling of the entire observed U-I behavior of the investigated STO layers becomes complex.

- **Comparison of different STO layers**

Slow U-I characteristics were measured for several samples with varying film thickness. The results obtained for those samples are depicted in Fig. 7.4. Moreover, the evaluated values for $\alpha_{n,p}$ are shown in Tab. 7.1.

From the $\log I$ vs. U plot differences in the anodic as well as in the cathodic range can be observed between the individual samples. The analysis of α -values shows that in the anodic range values close to 1 can be found. This stands in contrast to those values obtained for the cathodic range. For all investigated samples a distinct deviation from $\alpha = 1$ could be found for the negative bias range. It is quite probable that the slow U-I curve represent a sum of several

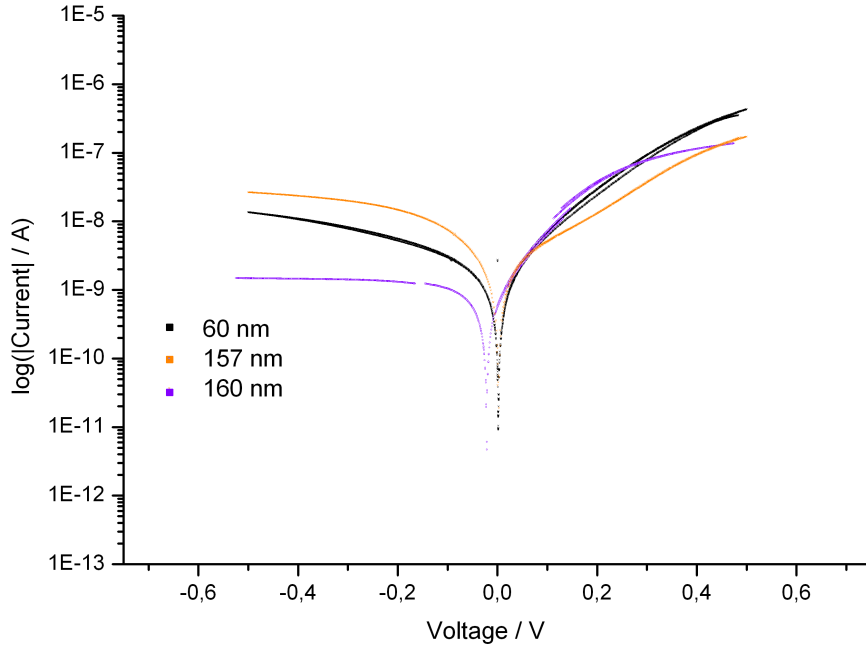


Figure 7.4

Fig. 7.4: Comparison of U-I curves measured for 3 different samples. The temperature used was for all of those samples in the range of 375°C.

processes occurring in parallel. Stoichiometric polarization, as it was already described in literature for single crystalline and polycrystalline bulk material can only partly explain the steady state curves of the investigated thin films.

sample thickness / nm	T / K	α_p (anodic range)	α_n (cathodic range)
60nm	675	0,64*	0,13
230nm	698	0,80	-
230nm	673	0,80	-
110nm	604	0,92*	0,13/0,14
110nm	549	0,84*	0,13/0,12
110m	651	0,88*	0,15/0,16
152nm	676	0,78	0,07
152nm	702	1,09	0,18
152nm	692	0,87*	0,18
152nm	604	0,92*	0,18

Tab. 7.1: Data for α was analyzed for several samples, and was separately evaluated for the anodic as well for the cathodic regime. The results are depicted in this table. Values marked with * \rightarrow fits only up to +250 mV.

7.2 U-I characteristics: Fast measurements

The following section deals with the presentation and discussion of fast measured U-I curves. The starting point –accurately, the starting voltage– splits the performed experiments into three sub-experiments. Besides the starting point at +400 mV (furthermore denoted as **anodic curve**), the opposite value of –400 mV (**cathodic curve**) was used for the experiments conducted. In addition to those starting conditions, the 0 V and 0 A point was chosen as origin for the third "fast" current-voltage curve (**origin curve**). In the case of the two measurements starting at a voltage different from 0 V, it was important to first let the sample reach the steady state condition.

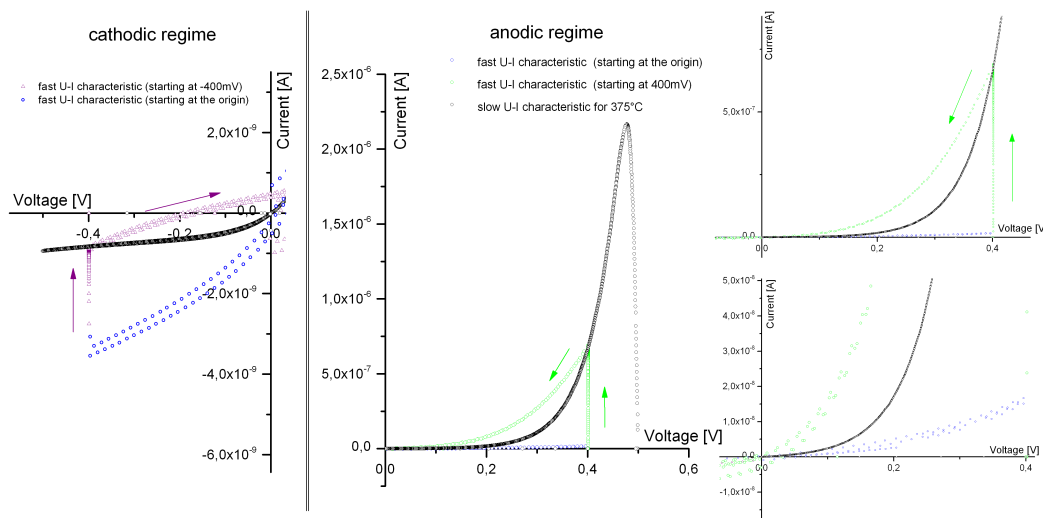


Figure 7.5

Fig. 7.5: U-I characteristics can be measured in different ways, this diagram compares a slowly measured U-I curve (black) with three fast measured curves for a 152 nm at 375°C ("Micro" set-up). The difference between these curves originates in the starting point. The green curve starts at +400 mV, the blue one has its origin at 0 V bias and the purple one represents the curve starting at -400 mV.

Especially at these low experimental temperatures (375°C = set-temperature for the illustrated 152 nm sample, see Fig. 7.5) the sample reacts quite slow on the changing conditions. Hence the appropriate bias voltages were applied for a substantial time (5-10 min.) before the U-I curve was recorded. In Fig. 7.5 this is indicated by the continuous current change at constant bias voltage marked by the green (–400 mV) and pink (400 mV) arrow, respectively. Within this time the current reaches the value of the slowly measured U-I curve and the adjusted steady state serves as a defined starting condition for the subsequent fast measured voltage cycle.

The measured data sets for the fast U-I curves –irrespective of the starting voltage– were measured back and forth in the range between +400 mV and –400 mV to evaluate possible variations of the sample during the experiment. In Fig. 7.6 and Fig. 7.7 the results for the 152 nm sample are separately depicted for the anodic as well as for the cathodic curve.

• Characteristic fast U-I curve – starting voltage +400 mV

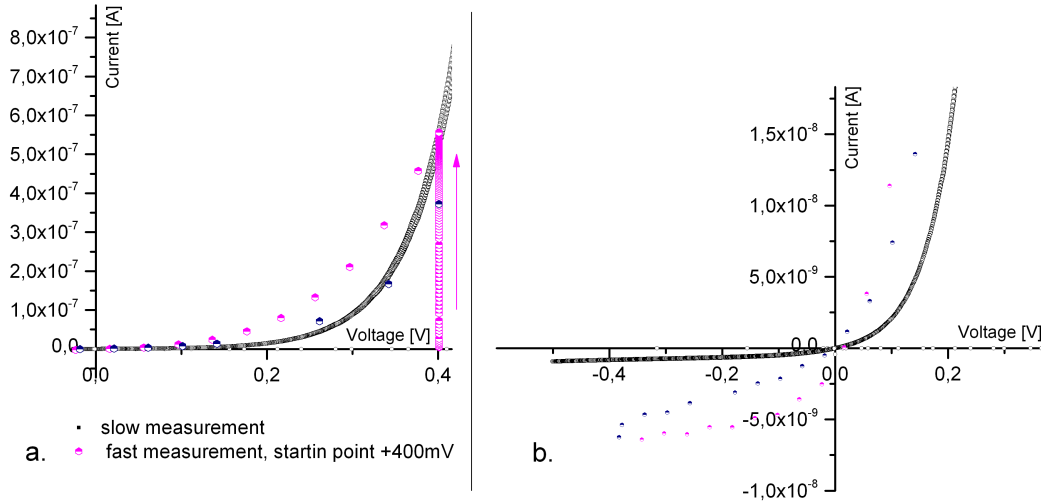


Figure 7.6

Fig. 7.6: Illustration of the fast U-I curve (152 nm sample, 375°C, "Micro" set-up) starting in the anodic range (a), with the continuously changing current, while reaching a steady state in the first 5 minutes, followed by applying a fast voltage change. The measurement was extended into the cathodic range (b), and was performed in the backward direction with the result of achieving a forward and a backward curve.

The U-I curve was measured within a few seconds, therefore the point density is decreased. Nevertheless the shape of the curve can be analyzed. In the anodic regime the fast curve shows a distinctly flatter slope as the slowly measured curve, but does not exhibit a linear behavior. In the cathodic range the curve shows a similar gradient as the slowly measured curve, but the recorded current is substantially increased. The backward monitored curve does not overlap with the forward curve. After switching the voltage scan into the opposite direction the current in the cathodic range is instantly decreased. The backward curve crosses the forward curve in the origin and the last part of the recorded curve back into the anodic range of the curve is located below (smaller current) the forward curve.

• Characteristic fast U-I curve – starting voltage –400 mV

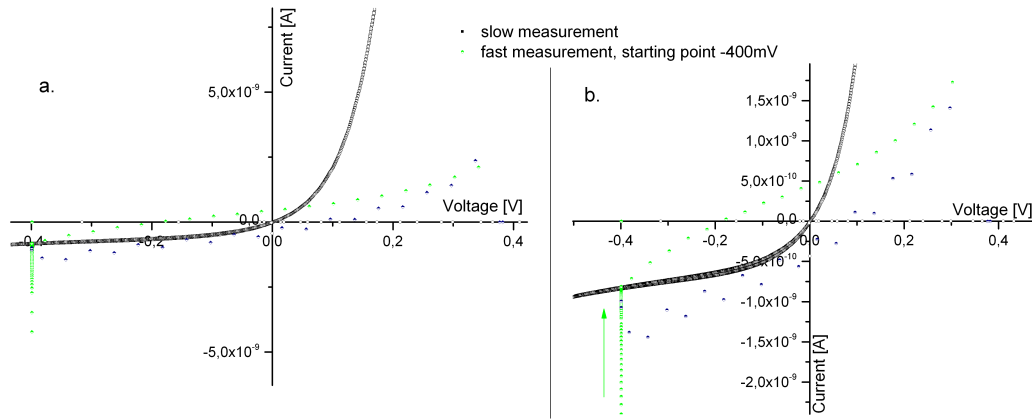


Figure 7.7

Fig. 7.7: The same experiment as it was performed for the anodic curve (see again Fig. 7.6), was executed in the cathodic regime. The observation of shifted forward and backward curves was similar which is indicated in (a) for the complete bias range. In (b) a zoom-in of the cathodic range is depicted

Current-voltage characteristics recorded with the start in the cathodic range show a steeper slope than the slowly measured curve. The intersection with the x-axis can be found for this measurement at -200 mV. The further curve (anodic regime) then shows a much flatter slope compared to the sharp increase of the current with increasing positive voltage monitored for the slowly performed measurement. As it was already mentioned for the anodic curve, a shift between forward and backward curve could be observed. In the case of the cathodic curve this is, however, especially pronounced. The intersection point of the backward curve is even located in the positive voltage range, at about $+100$ mV. Back to the starting point, the measured current is slightly higher than the initial current monitored.

• Characteristic fast U-I curve – starting voltage 0V

Fig. 7.8 displays the fast curve starting at 0V, i.e. without any applied bias. Also here a nonlinear curve results with higher currents in the anodic regime and a certain hysteresis. Currents are larger than for the cathodic curve.

• Evaluation of the correct time for monitoring a fast U-I curve

Based on the chosen starting point and the used temperature, the measuring times had to be adapted for the different samples and conditions. The optimum time for this kind of measurement can be determined from the cor-

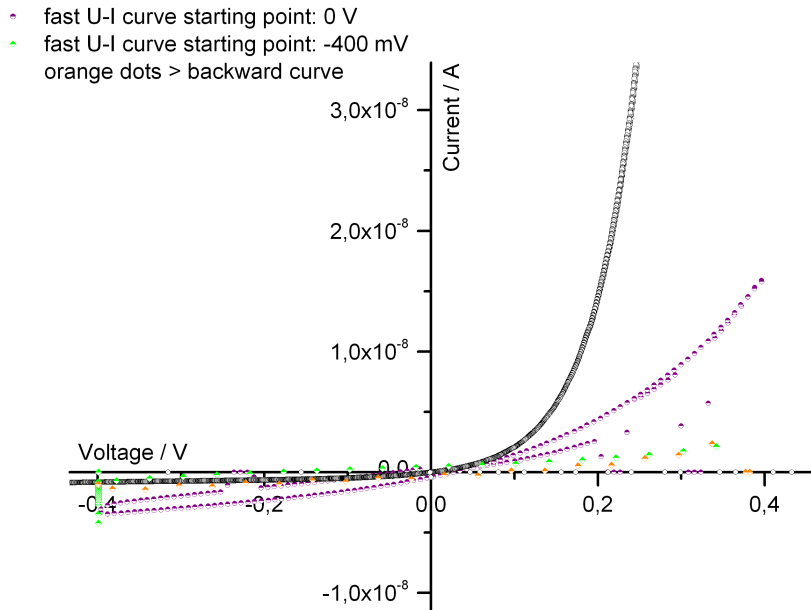


Figure 7.8

Fig. 7.8: Illustration of the fast U-I curve (purple colored circles), with its starting voltage of 0 V. To emphasize that this curve reflects a sample in a very different state, the fast curve starting in the cathodic range is also depicted.

responding impedance measurement: It corresponds to the frequency range that is neither affected by C_1 or C_S nor by the low frequency feature (arc, loop). The frequency point located close to the real axis between high and low frequency range was therefore evaluated for the same or a similar temperature. From this frequency point the required time (= the time regime wherein capacitive and polarization effects –leading to hysteresis in U-I curves– are absent) was determined. This procedure did not pose a problem for the anodic data. Frequency points on the real axis and in the immediate vicinity of this axis could be easily determined due to the occurrence of loops in the anodic range, particularly between 200 mV and 400 mV. On the one hand this crossing of the real axis allowed a straight forward determination of the appropriate time for the "fast" U-I curve. On the other hand, the decreasing resistance values by means of increasing positive bias voltage comes along with an increase of the "crossing" frequency values. Hence, the times to monitor a fast current-voltage curve with the origin in the anodic range, decreased to values below 1 second.

In the cathodic range, the impedance plot does not show any intercept with the x-axis since generally a second semicircle appears in the low frequency range. Despite the fact that for higher temperatures loops could sometimes be reported for the cathodic regime as well, this is not the case for the low

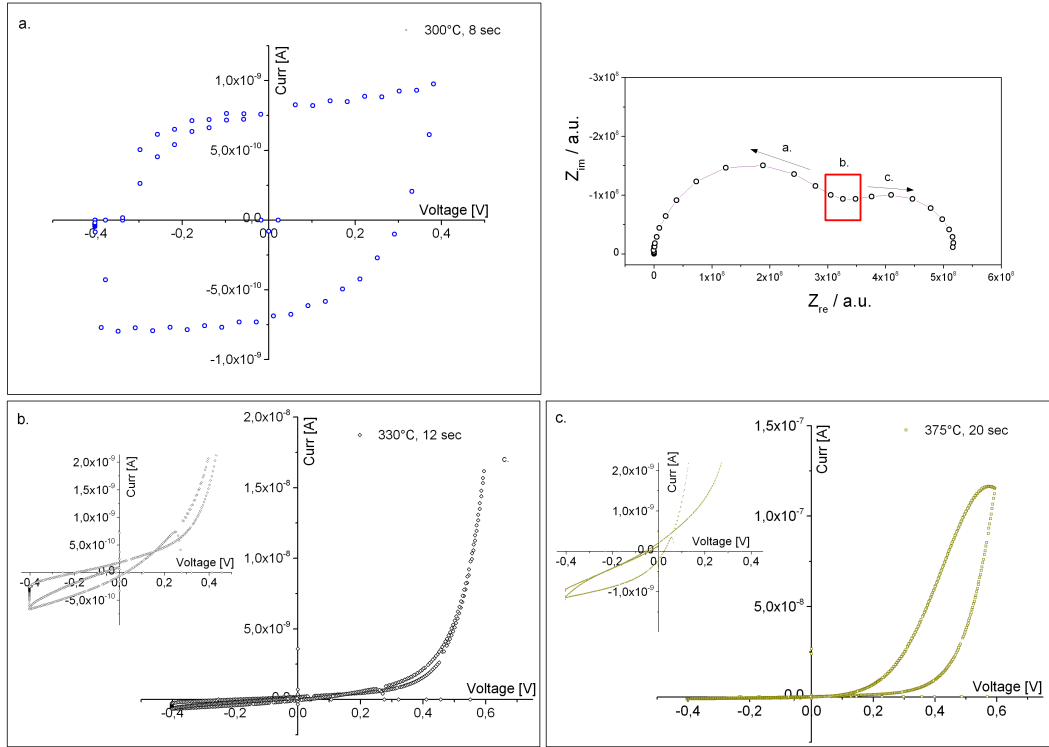


Figure 7.9

Fig. 7.9: The fact that no intercept with the real axis in the cathodic case could be observed, manifests itself in the difficulty of defining an appropriate measuring time. For several thin films the reported data switched either into case (a) (too fast) or case (c) (too slow), both depicted with magnification. In (b) the case of a more or less unperturbed U-I curve is shown.

temperature impedance data. Below 425°C all measured samples showed a second semicircle under cathodic bias as far as those low frequency range could be monitored at all. Hence, it was not possible for any investigated thin STO film to achieve unperturbed fast current-voltage curves for the cathodic case, due to the fact that capacitive effects and thus hysteresis was unavoidable.

In Fig. 7.9 the difficulty of defining a reasonable measuring time for the cathodic curve is exemplarily depicted for a sample at two different temperatures (300°C and 375°C set temperature). Regarding the reference impedance plot (from simulation) in the same figure, the orange marked range denotes the frequency points which would provide the most reasonable cathodic current-voltage curve. Because of the fact that the imaginary part of the impedance is never zero, an ideal measuring time does simply not exist.

A further distortion of the experimental data appears, when the deviation in measuring time is increased either to faster (case (a)) or to slower (case (b)) times (see Fig. 7.9). These changes in measuring time correspond to shifts in the impedance plot. A faster measuring time represents a shift into the

high frequency regime (semicircle_{HF,total}) whereas on the other hand a slower measuring time leads to a shift into the low frequency regime (2nd semicircle). Consequently, the U-I curve which is measured too fast manifests itself in a strong hysteresis loop, as it is depicted in Fig. 7.9 (case (a)). This hysteresis loop exhibits more or less the same voltage offset (≈ 300 mV) for the anodic as for the cathodic range. The development of this hysteresis loop and the already mentioned shift into the high frequency semicircle, indicates that the curve reflects the loading curve of a capacitance.

The second case which is shown in Fig. 7.9(c), deals with the situation of a measuring time which is too slow. After reaching steady state the current-voltage measurement is started from -400 mV bias and shows at first a more or less linear behavior. In the adjacent anodic regime a distinct non-linear behavior appears and furthermore the back and forth measured curves in the anodic range do not coincide. Again a hysteresis curve is formed, as it is shown in the zoom-in (see case (c)). This change of the current-voltage curve with changed measuring time can be attributed to the increasingly dominating effect of the stoichiometric polarization (Wagner-Hebb). This means the longer the measuring time becomes, the more time is provided for oxygen vacancies to move. Consequently, by a further distinct increase of the measuring time one would finally reach steady state conditions in each measuring point, which corresponds to nothing but the slow measured curve. Based on these effects, the measurement of a fast current-voltage curve from a cathodic steady state situation is a non-trivial experiment and accordingly needs to be discussed with caution.

- **Analysis of fast U-I curves performed on several thin films**

Apart from the mentioned difficulties it was still possible to obtain measuring times which provide more or less unperturbed fast cathodic U-I curves, i.e. without hysteresis (see Fig. 7.9(b)). From the depicted zoom a minor deviation of the forward and backward curve can be seen. On the one hand this could stem from the not entirely perfect matching scanning rate. However, it can also not be fully excluded that the samples are slightly changing even under this particularly fast measuring conditions, especially since such small deviations of the recorded backward curves were also be found for the anodic curves.

The obtained cathodic curves are further depicted in the following figures, and are compared with anodic curves. All figures dealing with results for fast U-I curves, emphasize the great influence of the starting voltage (anodic or cathodic) on the resulting current-voltage characteristic. This is not only valid when comparing anodic and cathodic curves (+400 mV and -400 mV), but also for fast U-I curves starting in the origin (0 V, 0 A).

The fast current voltage behavior of a 152 nm layer was investigated at 376°C (T_{real}) for an unannealed and an annealed sample. The recorded data along with the fits are depicted in Fig. 7.10(a) and Fig. 7.11(a). The voltage scanning was proceeded in a range from 400 mV to -400 mV and vice versa. All curves were fitted by using an exponential function: $y=j_0(e^{R_0 \cdot (U-U_0)}-1)$ where R_0 again stands for $\frac{\alpha e}{k_B T}$ and j_0 denotes the prefactor. In case of the fast measured U-I curves an offset U_0 has to be included in the exponential term. From this equation the parameter α was again analyzed for the fast current-voltage curves. As it can be seen from Fig. 7.10(a) the anodic as well as the cathodic range of the anodic curve (= starting from an anodic steady state) for the annealed sample can be fitted quite accurately. In case of the unannealed sample (Fig. 7.11(a)) the fit looks also quite reasonable, even though a closer look at the cathodic regime displays that the fit shows a distinct deviation from the experimental data in cathodic range. The results for the α -values are depicted in Tab. 7.2. The results for the curves starting from the cathodic steady state are depicted in Fig. 7.10(b) and Fig. 7.11(b).

sample thickness / nm	T / K	α (anodic curve)	α (cathodic curve)
230 nm	550	0,62	-
110 nm	549	0,40	0,42
152 nm (annealed)	648	0,49	0,45
152 nm (unannealed)	648	0,49	0,18
157 nm	598	0,20	0,015

Tab. 7.2: Data for α was analyzed for four samples measured in the fast mode.

It needs again to be emphasized that the fast performed measurements do not monitor stoichiometric polarization within the layer. It reflects more or less the charge carrier distribution in one appropriate bias point, and the fast curve monitors the electrochemical behavior of this one particular sample condition. An evaluation of α does therefore not reflect the meaning as for Wagner-Hebb polarization. Rather it includes information on other processes causing non-

linear curves such as pn-junctions or other space charges. The fact that the investigated thin films exhibit different stoichiometric condition, depending on the applied bias voltage, leads to the often very different anodic and cathodic U-I curves.

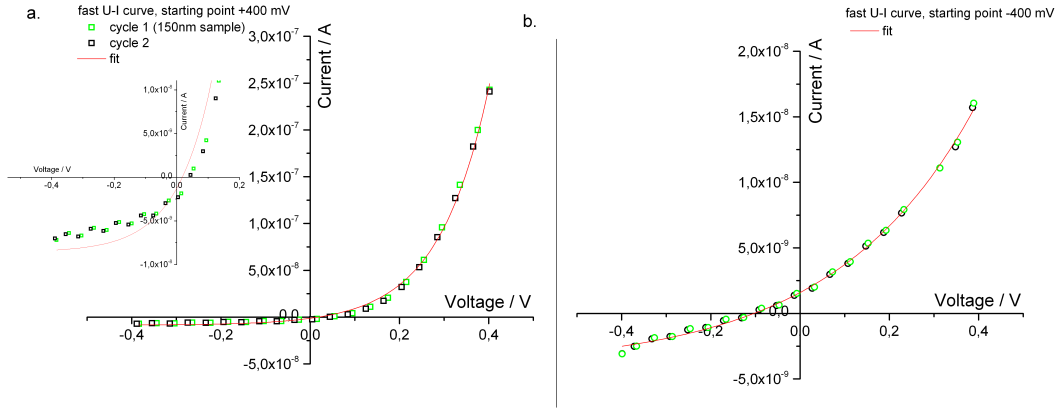


Figure 7.10

Fig. 7.10: Illustration of the fast anodic (a) and cathodic (b) curve for the unannealed 152 nm sample at 376°C (T_{real}).

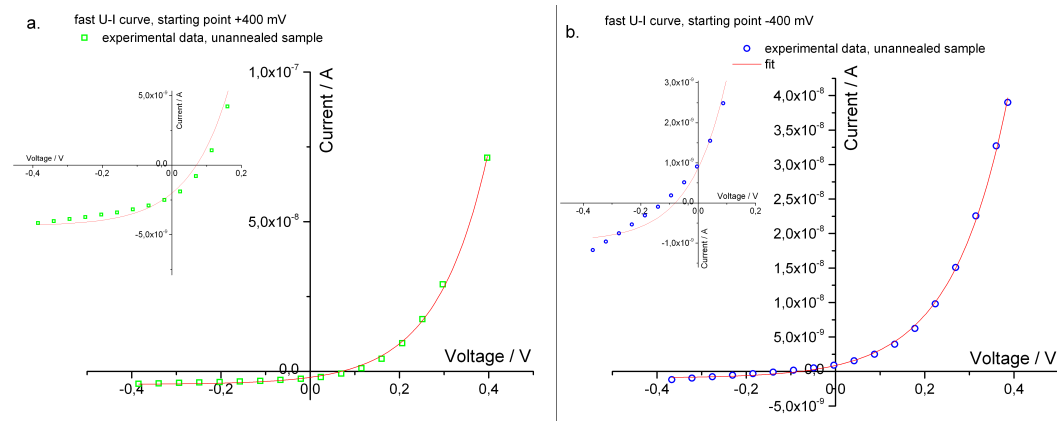


Figure 7.11

Fig. 7.11: In comparison to the annealed sample (Fig. 7.10), fast U-I curves starting in the anodic (a) and the cathodic (b) regime were also measured for the annealed sample at the same temperature.

Stoichiometric polarization occurs due to the sufficiently high electrical field strength (kinetic aspect), thus it is quite probable that a pn-junction appears in the thin films when an anodic bias voltage is applied. This is not a new phenomena occurring in SrTiO₃. Rodewald^[33,34] observed a distinct separation of charge carriers (electrons, holes and oxygen vacancies) under high electrical field strength values which also leads to the generation of a pn-junction in the STO single crystals. The crucial difference can be found in the specimen dimension. In a thin layer of a few nm, an extremely sharp pn-junction appears, which can be experimentally monitored in terms of a diode-like nonlinear be-

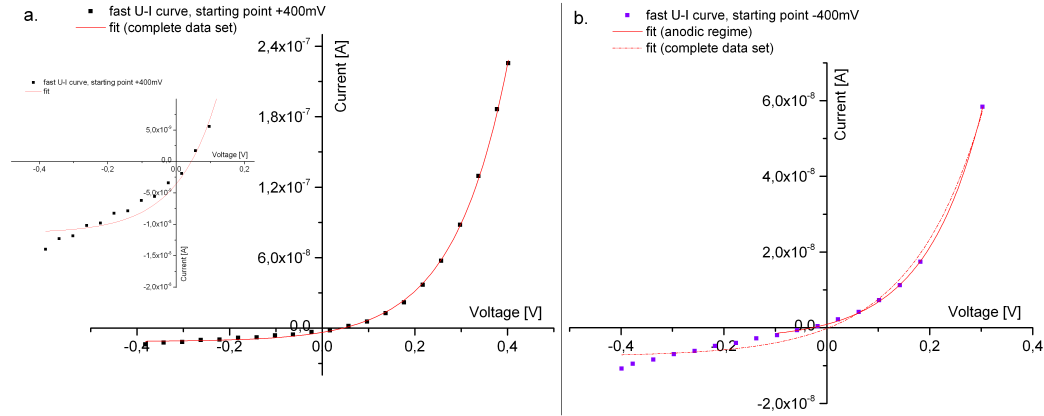


Figure 7.12

Fig. 7.12: Illustration of the fast U-I curves, starting from an anodic (a) and a cathodic (b) bias, for the 110 nm sample at a temperature of 402°C (T_{real}).

havior. In a single crystalline bulk sample on the other hand, the extent of the pn-junction smears over a few μm , and is therefore not measurable as a non-linearity.

With the anode located on the LSC side, the external current opposes the internal potential due to the created pn-junction, as it is for the forward bias case of a diode. In the cathodic regime, the polarity is switched at the electrodes and the pn-junction in the thin layer becomes very blocking. Despite good qualitative agreement of model and experimental curve, the diode-like fit function used here does not fully describe the experimental data. However, in the cathodic regime, despite the fast measuring time, small changes can occur in the charge carrier distribution inside the thin film and consequently may slightly modify the current-voltage curve during recording. The non-linearity of the cathodic curve might be, accordingly, due to a pn-junction. However, as well as the origin curve, it might also be caused by other space charges: Those are present even without the development of a pn-junction, and most probably around dislocations. Their U-I curves, can not simply be described by the used exponential function.

Furthermore, an interesting effect can be seen in the presented fast current-voltage plots. Most fast U-I curves measured in the "Micro-Macro" set-up showed an offset from the origin (0 V and 0 A) which was taken into account by U_0 in the applied fitting routine (see above). This offset could not be simply correlated to a thermo-voltage, as it was the case for the slow current-voltage measurements performed in the asymmetrically heated "Micro" set-up (not shown in this work). However, this offset could not be observed for all

measured samples. Fig. 7.13 depicts a comparison of fast measured curves in the anodic range for two layer with thicknesses of 110 nm and 240 nm, respectively. The 240 nm shows no offset at the origin, and additionally more or less linear behavior in the anodic range. For the fast U-I curve recorded in the "Micro-Macro" set-up an offset of 46 mV for the anodic regime and an offset of -28 mV for the cathodic regime could be observed. Exact reasons for this behavior are not known yet but it cannot be excluded that it reflects the electromotive force in the thin film formed due to bias and non-negligible ionic transference number.

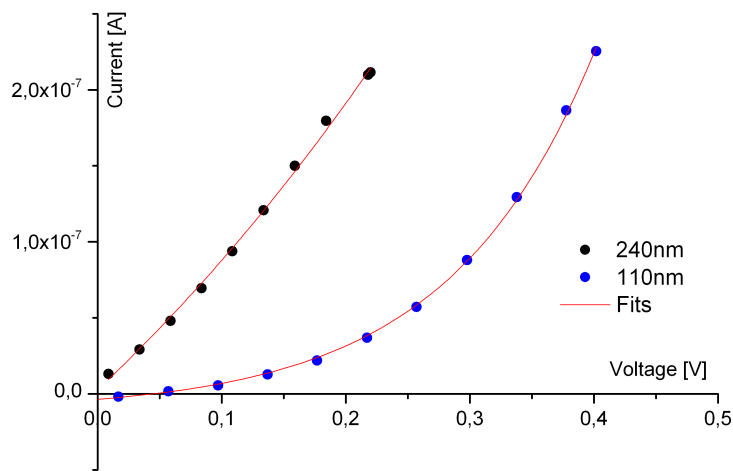


Figure 7.13

Fig. 7.13: Comparison of two fast measured anodic U-I curves at 400°C in the anodic regime for two layers of different thickness (240 nm and 110 nm).

7.3 Current-voltage characteristics compared with impedance data

So far, the two measurement approaches (Impedance spectroscopy and DC measurements) were separately discussed. At this point of the discussion the question arises, if the results from impedance measurements confirm the results from DC measurements, and vice versa. As it was mentioned before, a difference between fast measured curves exists, due to their particular starting point. For the following discussion of clarifying the relationship between impedance data and results from DC measurements, fast U-I curves at the appropriate bias voltage were compared with slowly measured U-I curves and with the corresponding impedance data monitored at the same bias voltage. Considering the temperature, it should be mentioned that the experimental

data from these two experiments were recorded at two different temperatures (Impedance measurements ca. 600°C and DC measurements at ca. 400°C). At one and the same temperature, low frequency features were either at extremely low frequencies and thus not accessible or times required for fast U-I curves were too short.

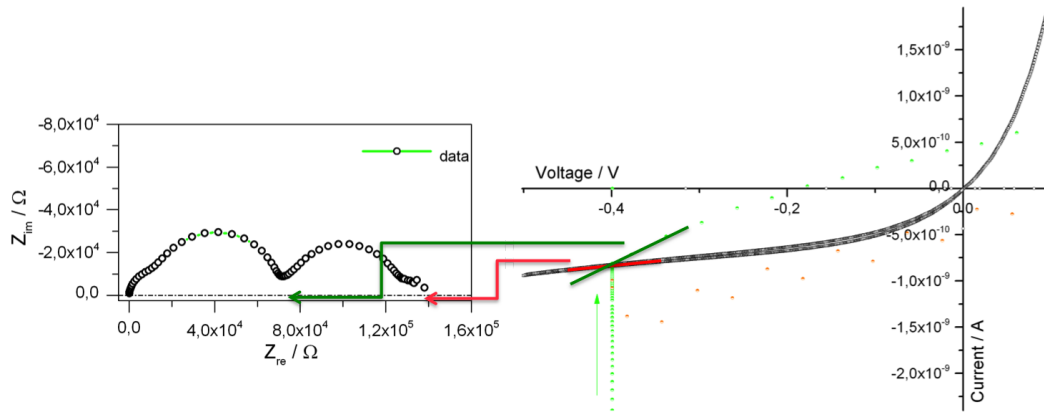


Figure 7.14

Fig. 7.14: U-I curve for the cathodic range compared with impedance data recorded under cathodic bias. Two different temperatures were used for these two experiments. Still this can illustrate the origin of the second semicircle.

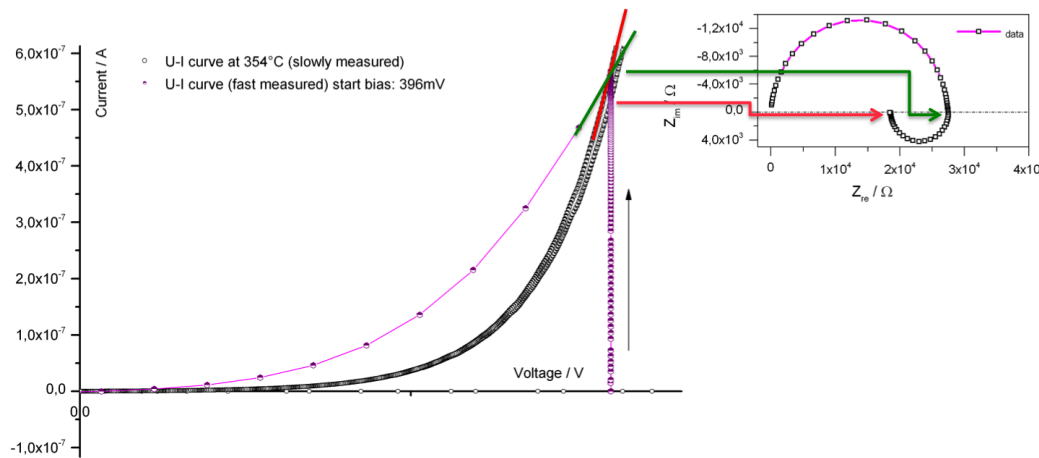


Figure 7.15

Fig. 7.15: Anodic range of the same U-I curve as in Fig. 7.14 compared with anodic impedance data. Again two different temperatures were applied but the reason of the loop becomes very obvious.

Obtained results and their interpretation are illustrated in the following Fig. 7.14 and Fig. 7.15. The slopes of the two U-I curves (slowly and fast) measured were analyzed in the working point (= appropriate bias voltage). The evaluated values are converted into a resistance value. The steeper slope corresponds to the smaller resistance value. The flatter slope on the other hand represents a higher resistance value. In the cathodic regime, the slowly measured U-I curve exhibits the flatter slope compared with the fast U-I curve.

This is consistent with the impedance results, where the total resistance is higher at low frequencies, due to the second semicircle. In Fig. 7.14 this is indicated by the red and green arrows.

In the second case (anodic bias), the slopes of both U-I curves were again analyzed with the result, that the slowly measured curves show the steeper slope, which corresponds to the smaller value for the total resistance. This finds its surprising counterpart in impedance measurements. For the anodic case an additional loop was monitored which indeed decreases the total resistance in contrast to the resistance recorded for the high frequency arc (intersection point with the real axis).

Results and Discussion: DC load and Relaxation Experiments

Applying a DC voltage to a thin STO film results in a current and subsequently in a resistance change of the material. This behavior was already observed in Chapter 7 for the U-I experiments where the continuously applied bias voltage finally led to a steady state. A given steady state was analyzed by the fast U-I measurements and different steady states were further probed by slow current-voltage curves. In the following, the time dependent changes due to an applied bias voltage were systematically investigated by means of DC load and relaxation experiments.

The experiments were performed on several STO films with varying thickness. Different temperatures (425°C - 375°C (set temperature)) and bias voltages (± 100 mV, ± 250 mV, ± 325 mV, ± 400 mV and ± 525 mV) were investigated to achieve meaningful information about ongoing migration and diffusion processes. The relaxation part of the experiment was performed from the anodic as well as from the cathodic range. In the following, the characteristic curves for a sample under DC load (+400 mV and -400 mV) as well as the development of resistance values during relaxation are depicted in Fig. 8.1. As it can be seen from Fig. 8.1, a continuous increase of the resistance for the cathodic and a decrease for the opposite –the anodic– direction can be observed. In that special case the monitored curves for both bias polarities reach new steady state conditions within 100 s, i.e. uniform resistance values are reached under constantly applied bias voltages.

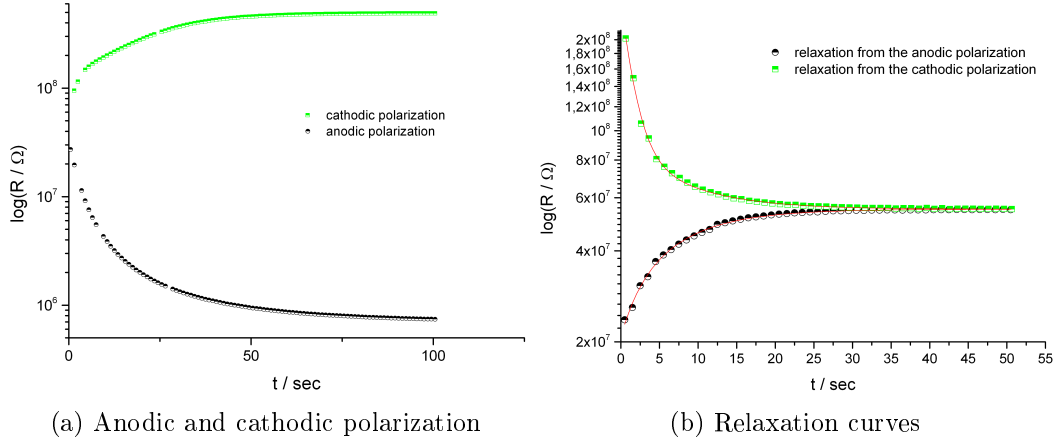


Figure 8.1

Fig. 8.1: Characteristic curves for an anodic (black circles) and a cathodic (green squares) DC load experiment for a 152 nm sample at 354°C (T_{act}) depicted in (a). The relaxation curves starting from both polarities are shown in (b) for the same sample and temperature.

For the relaxation part of the measurements, the resistance value is based on relatively small current values, thus an increasingly noisy data was monitored. The reason for that lies in the small applied voltage values (≈ 0.5 mV) during relaxation. On the one hand, finite values were necessary to gain relaxation data at all, but on the other hand they ensure the absence of distortion due to stoichiometric polarization. The achieved results, depicted in Fig. 8.1 show that also quite nice curves for the relaxation could be measured. The shape of the 2 curves is slightly different, but the resistance value (= new steady state condition) reached, is the same for both relaxation curves.

- **Analysis of the experimental data by means of the characteristic decay time**

Data for the DC stress experiments as well as for the relaxation experiments were quantitatively analyzed by means of the two following exponential equations Eq. 8.1 and Eq. 8.2.

$$R = R_{\infty} + (R_{\infty} - R_0) \exp\left(\frac{-t}{\tau}\right) \quad (8.1)$$

$$R = R_{\infty} + (R_{\infty} - R_0) \exp\left(\frac{-t}{\tau_1}\right) + (R_{\infty} - R_0) \exp\left(\frac{-t}{\tau_2}\right) \quad (8.2)$$

Therein, R_{∞} and R_0 denote the resistance values in the newly adjusted steady state and before DC stress, respectively. The characteristic time constant for

the decay function is defined by the parameter τ . For some special cases a better fit of the monitored data was received by using Eq. 8.2, which contains a second exponential function and consequently a second τ -value (τ_2). With this extended fit function it was possible to also describe the sharp resistance drop in the first seconds of the measurements. For the subsequent comparative analysis τ -values (Eq. 8.1) were related to τ_2 -values from Eq. 8.2. In Fig. 8.2 and Fig. 8.3 we applied these two exponential functions on experimentally recorded data (relaxation and DC load). In the following presentation of results it is not explicitly mentioned whether Eq. 8.1 or Eq. 8.2 is used.

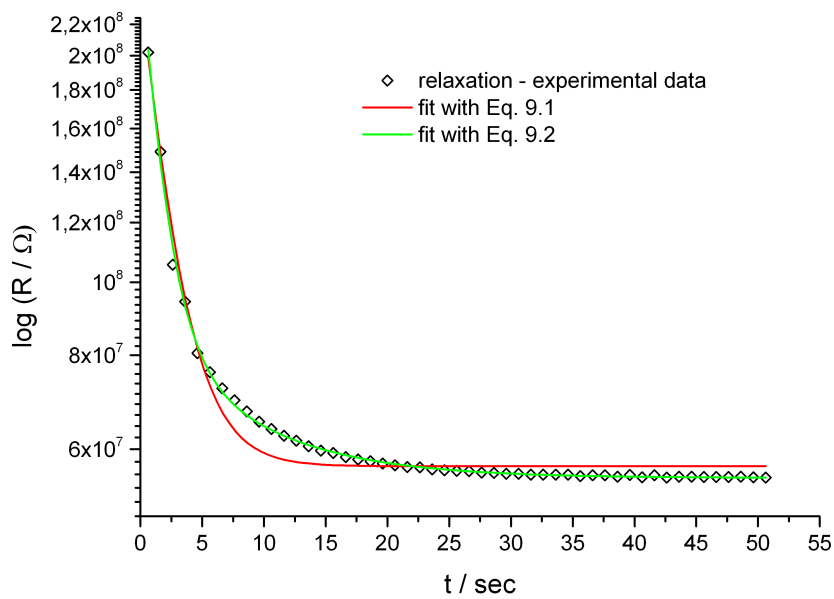


Figure 8.2

Fig. 8.2: Comparison of the fitting results obtained with Eq. 8.1 and Eq. 8.2 for a relaxation experiment. The measurement was performed at 375°C (T_{set}) and the relaxation cycle started at -250 mV.

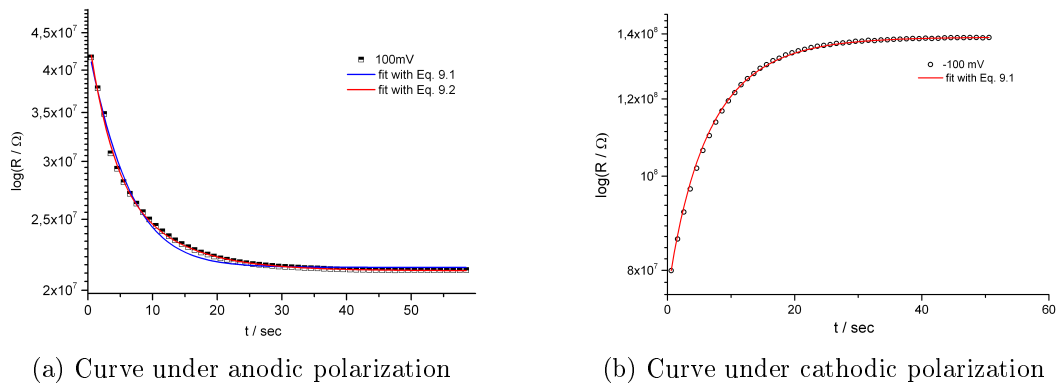


Figure 8.3

Fig. 8.3: Exemplary illustration of the used fitting routine for polarization experiments. The measurements were performed at 375°C (T_{set}). The applied bias voltages were ± 100 mV.

One experiment contained several cycles, which had the advantage to continuously change between the DC load and relaxation part of the experiment. This offered the opportunity to screen the observed behavior on its reproducibility. In Fig. 8.4(c) the excellent reproducibility of the process is shown for a 152 nm thin STO film at 375°C (T_{set}).

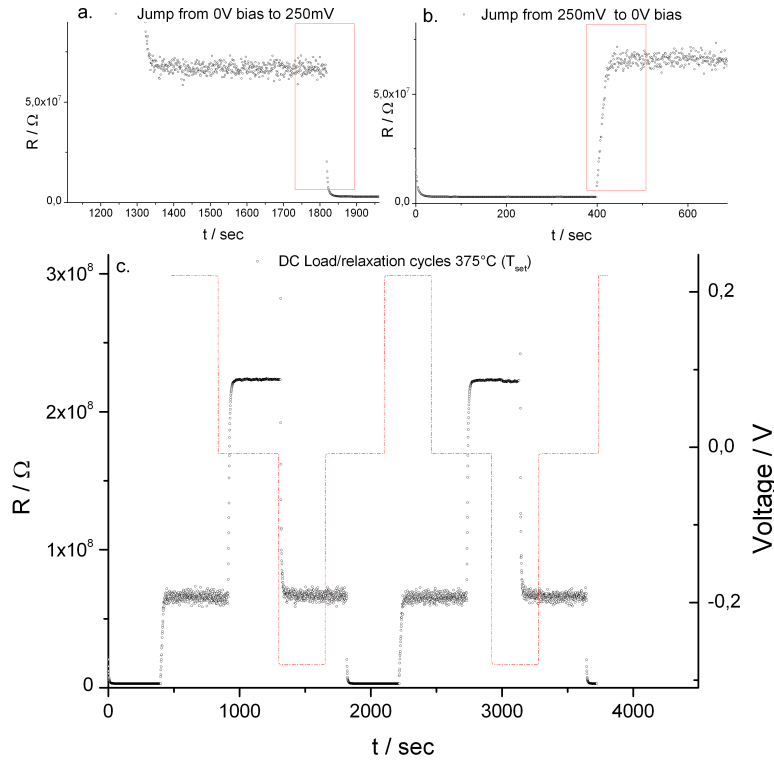


Figure 8.4

Fig. 8.4: Illustration of the excellent reproducibility of the resistance of the thin film under DC stress as well as during relaxation.

- **Analysis of the temperature dependence of τ**

Temperature values were changed in a small interval between 375°C and 425°C (T_{set}). For a 215 nm sample the different temperatures were investigated by applying ± 250 mV on the thin film with relaxation steps in between. The resulting Arrhenius plots for the two relaxation processes are compared in Fig. 8.5 with the data obtained for the anodic and the cathodic DC load experiment. The time for relaxation is essentially independent of the bias direction. Accordingly, the evaluated time constants τ for the anodic and cathodic relaxation provide Arrhenius plots with essentially identical activation energies of 0.94 eV and 0.95 eV, respectively.

For the polarization by cathodic DC stress, only two data points are depicted, due to the fact that for the highest temperature of 425°C (T_{set}) the observed

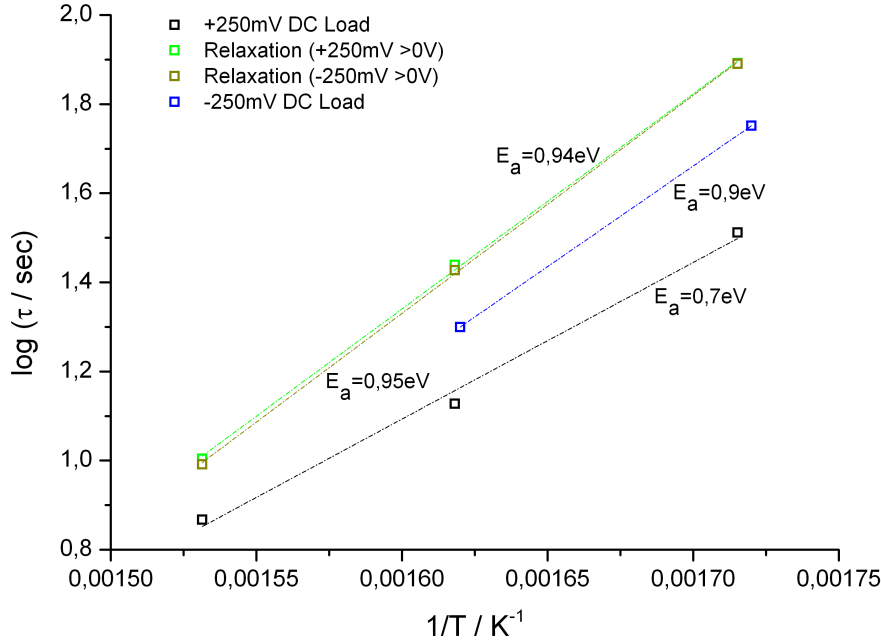


Figure 8.5

Fig. 8.5: Arrhenius plots of the relaxation processes starting in the anodic as well as in the cathodic regime, compared with the curves for the anodic and cathodic DC load (± 250 mV applied DC voltage); 215 nm sample measured in the "Micro-Macro" set-up.

change of the resistance reaches a maximum instead of a resistance plateau. The maximum is subsequently followed by a slow but continuous decrease of the resistance values, thus it is not possible to clearly evaluate the characteristic time for this specific temperature. The time constants for polarization of 2 further samples are depicted in Fig. 8.6.

On the basis of the results a tendency in the polarization behavior can be found. The activation energy for the cathodic polarization was in all cases larger than the activation energy for the anodic polarization. Furthermore, the activation energy of the anodic polarization showed less variation over the different samples (from 0.7 eV to 0.92 eV). Activation energies for the cathodic process range from 0.9 eV to 1.92 eV. The highest activation energy of 1.92 eV was evaluated for the -400 mV DC voltage. To answer the question, if this high value is obtained partly because of the higher applied bias voltage, or if it is only due to the structural differences of the thickest film would need some further experiments. Those slight structural variations occurring by means of preparation could play an important role, especially when different layers with varying thickness are compared.

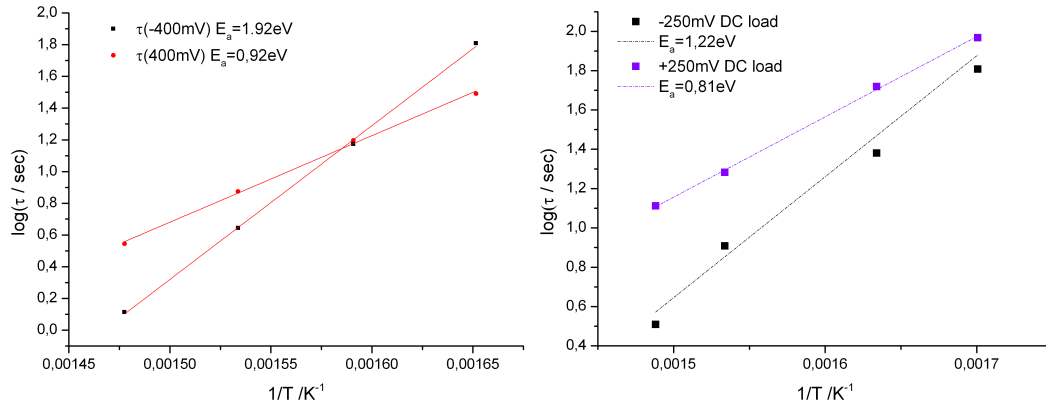


Figure 8.6

(a) Arrhenius plot of τ for the 152 nm sample. (b) Arrhenius plot of τ for the 413 nm sample. Polarization of ± 400 mV. Polarization of ± 250 mV

Fig. 8.6: Analysis of the activation energy of τ for the polarization experiment performed on 2 different samples.

• Analysis of the bias dependence of τ

Besides the investigations on the temperature dependence, the 152 nm sample was investigated by means of changing bias voltage (± 100 mV, ± 250 mV, ± 325 mV, ± 525 mV). For all these measurements a temperature of 375°C (T_{set}) was used. The obtained relaxation results for a 152 nm film are depicted in Fig. 8.7, with separately plotted diagrams for anodic (a) and cathodic (b) polarization. All measured curves could be successfully fitted. In the cathodic regime the same voltage values were analyzed with the exception that the -525 mV curve could not be fitted with the analytical functions for τ . The achieved values for the characteristic time τ are plotted against bias in part (c) of the same figure. The analysis shows that the sample needs more or less the same time to reach the steady state, independent from the starting voltage. This indicates that the chemical diffusion coefficient governing relaxation after stoichiometry polarization is very similar for all non-equilibrium states considered here.

The same experiment was performed for the polarization part. The DC load curves for the same sample are shown in Fig. 8.8. Although an external driving force is responsible for the migration of charge carriers within the sample there is again no distinct dependence on the applied bias. The sample is more or less insensitive on the electrical field strength for both polarities. This, however, is surprising since stoichiometry polarization experiments on bulk samples of SrTiO_3 showed much faster polarization for higher fields^[36]. Exact reasons for this behavior cannot be given yet. Partly, it may also be accidental, since

at least for the extreme voltages of ± 400 mV and ± 250 mV differences were found at certain temperatures (see Fig. 8.6).

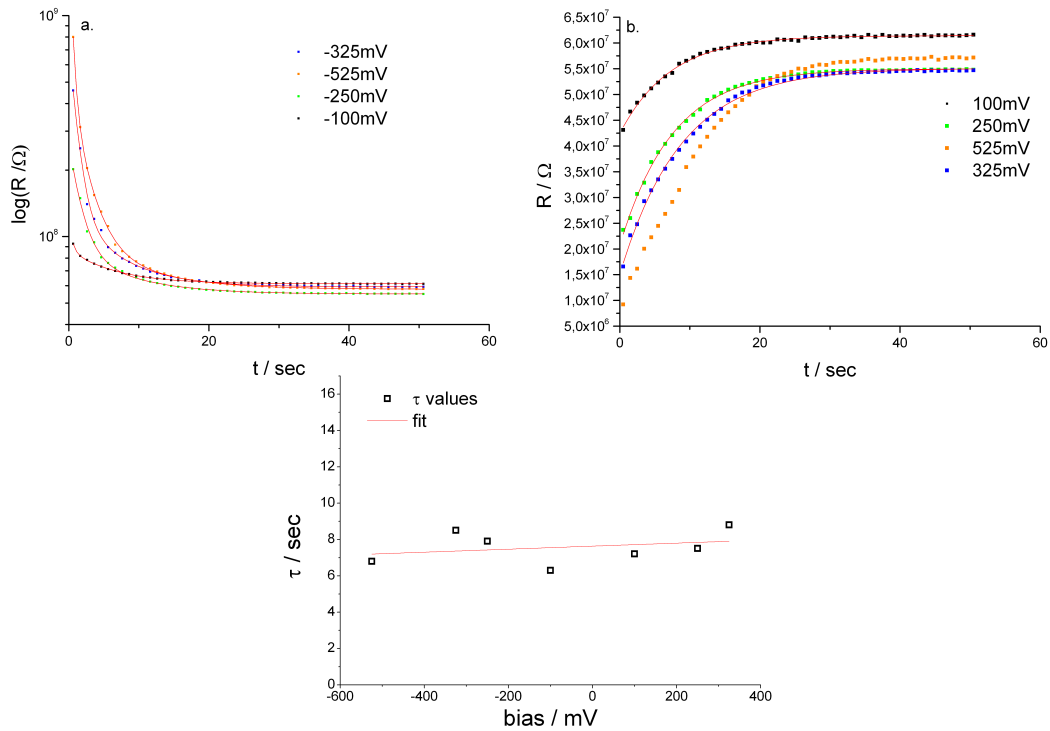


Figure 8.7

Fig. 8.7: Investigation of a 152 nm layer at 375°C (set temperature) as a function of bias voltage for the relaxation process after anodic (a) as well as after cathodic (b) DC load. In addition the evaluated characteristic times for both cases are plotted against bias voltage.

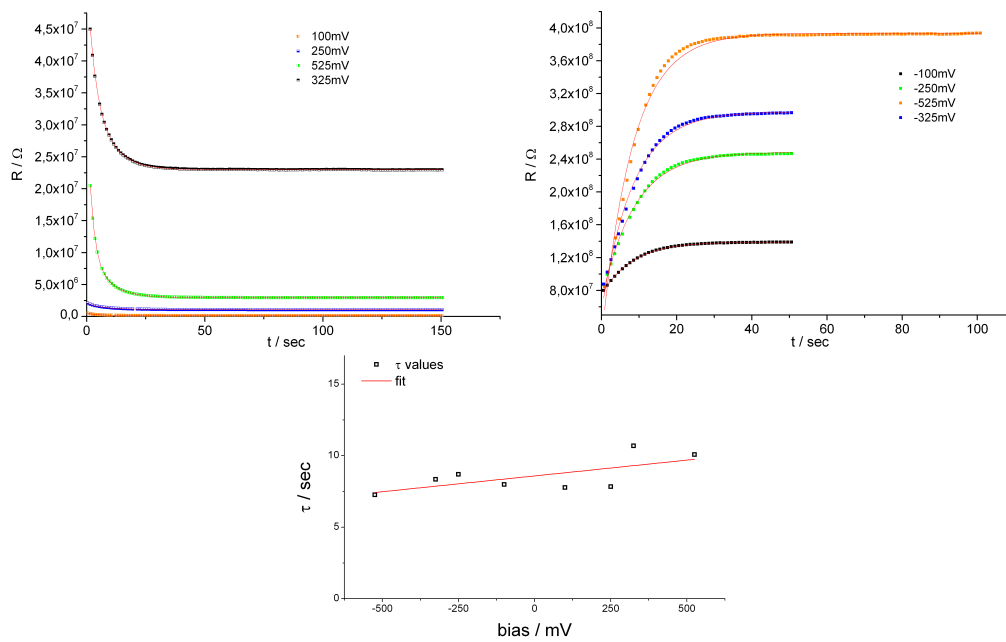


Figure 8.8

Fig. 8.8: Anodic (a) and cathodic (b) DC bias voltage was applied to the sample (152 nm) the relaxation behavior of which is shown in Fig. 8.7. In addition the bias dependence of τ is also depicted for the DC load part of the experiment.

Additional Measurements

9.1 Investigations of SrTiO₃ thin films after an additional annealing step

The biggest part of this work deals with the investigations of "as prepared" SrTiO₃ thin films, deposited on highly electronic conducting Nb-doped SrTiO₃ single crystals. Experimental data and analyzed results were discussed in the light of a high density of randomly located dislocations in the thin STO material. In order to analyze if a supposed change in the dislocation density can affect the electrochemical behavior, some thin films were undertaken an additional preparation step. The samples were cut in pieces and one piece was thermally annealed at 920°C and subsequently investigated with the focus on a changed electrochemical behavior in comparison with results for unannealed samples.

Measurements were again performed by means of impedance spectroscopy, DC measurements and thermally induced ¹⁸O tracer experiments. All comparative impedance measurements were either performed in the "Micro-Macro" or in the "Micro" set-up, within the same temperature range (450°C–700°C) as it was used for the unannealed samples.

- **Impedance measurements without external applied bias voltage**

The measurements were primarily conducted without an external field. Impedance plots for annealed (black) and unannealed (blue) samples with a variation in thickness, at different temperatures are depicted in Fig. 9.1.

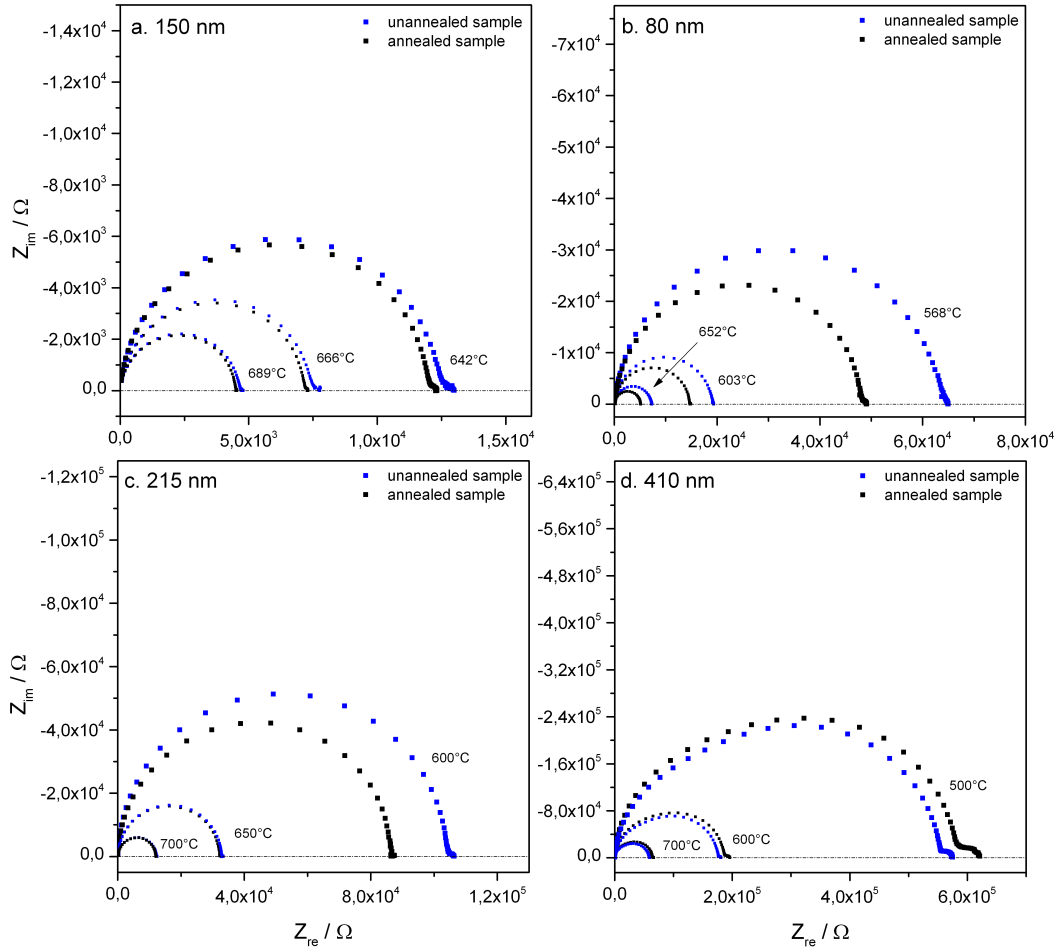


Figure 9.1

Fig. 9.1: 4 different samples (variation in thickness) were additionally annealed and the monitored impedance data is compared with results for the unannealed samples in a temperature range from around 700°C to 450°C.

For the investigated temperature range only slight differences in the measured impedance data can be found for all 4 measured layers. For most of the samples the difference between annealed and unannealed was in the same order of magnitude as the statistical scatter of resistance values measured on different electrodes on one and the same sample.

On the basis of the obtained impedance results it looks as if the annealing step has no distinct influence on the electrochemical behavior of the STO layers. Furthermore, it is definitely possible that the annealing temperature was too low to have a great impact on the reduction of the current dislocation density.

• Impedance measurements with applied bias voltage

The comparison between annealed and unannealed samples is furthermore extended to investigations under bias voltage. The monitored impedance plots measured at 500°C (T_{Set}) and ± 300 mV for a 215 nm and a 413 nm film are

depicted in Fig. 9.2 and Fig. 9.3, respectively. For the thinner layer a low

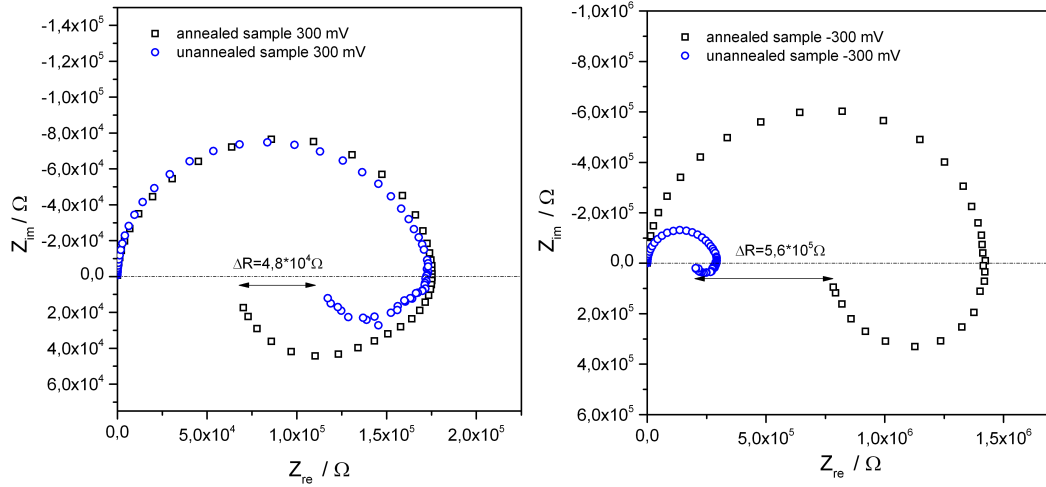


Figure 9.2

Fig. 9.2: Impedance data for the annealed and unannealed 215 nm sample. Measurements were performed at 500°C (T_{Set}) under 300 mV anodic and cathodic bias voltage. The differences in the total resistance are also depicted in these diagrams.

frequency loop was found for both bias cases, whereas the thicker layer shows the loop only in the anodic range. The annealed samples for both layer thicknesses create the same response on the applied bias as the unannealed samples. However, cathodic applied bias consequently leads to a distinct difference in the total resistance in both cases. The ΔR values are shown in the diagrams. Furthermore, in both cases the annealed sample exhibits the higher R_{total} when a cathodic bias voltage is applied.

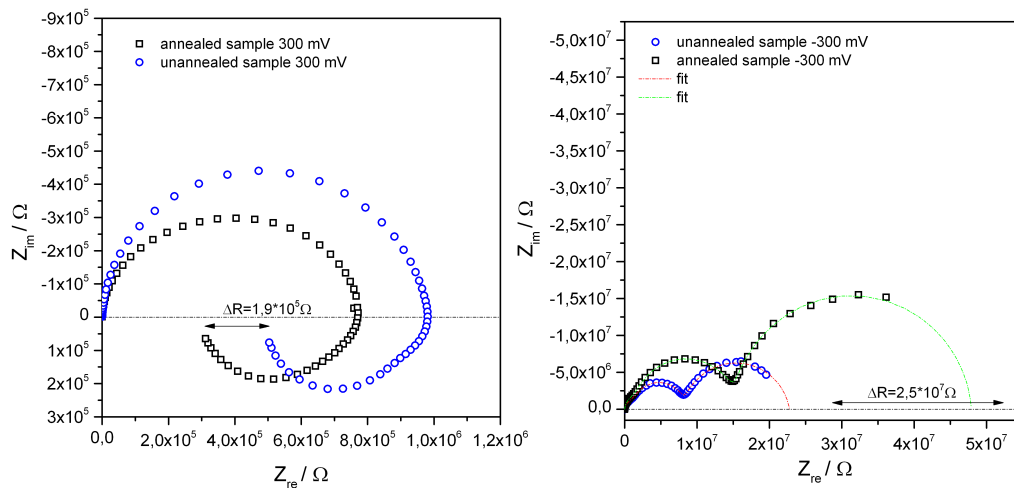


Figure 9.3

Fig. 9.3: The bias investigations were also performed for the 413 nm sample. The measurement parameters temperature and bias voltage were held constant (500°C (T_{Set}) and ± 300 mV bias)

In the anodic case the difference in the resistance is not that pronounced. Under anodic conditions the annealed sample exhibits the lower resistance value than the unannealed sample. For the cathodic case the ratio $\frac{R_2}{R_{total}}$ and for the anodic case the ratio $\frac{R_2}{R_{HF,total}}$ were evaluated, to compare annealed and unannealed samples. Values of 0.46 and 0.3 (cathodic case) as well as values of 0.65 and 0.35 (anodic case) were obtained for the thinner layer. In case of the 413 nm sample the analyzed values were 0.68 and 0.63 (cathodic case) and 0.64 and 0.52 (anodic case). In each case the value mentioned first is the result obtained for the annealed sample. Based on these achieved values, it seems as if the ratio in the annealed case is slightly increased. Also absolute resistance values seem to be more different upon bias compared to the data for the two films without bias (Fig. 9.1). However, since measurements with annealed and unannealed samples were not performed systematically, it is not possible to gain a final conclusion by means of these two samples.

- **Current-voltage characteristics for unannealed and annealed STO samples**

Slow current-voltage measurements were performed for 2 different samples (152 nm and 215 nm) with the focus on comparing the results for unannealed and annealed samples. The obtained U-I curves for the investigated samples are depicted in Fig. 9.4 and Fig. 9.5. For both unannealed samples and the 2 annealed sub-samples the analysis of the differential resistance was performed in the 2 bias points +300 mV and -300 mV (by linearizing in a range of ± 10 mV). The obtained results are shown in Tab. 9.1. The current-voltage curves of both sample pairs emphasize the different slopes in the anodic as well as in the cathodic regime. Interestingly, these 2 sample pairs do not show exactly the same behavior. In the case of the thicker layer, as it can be seen in Fig. 9.4 and Tab. 9.1, the anodic regime shows the smaller slope for the unannealed sample, and consequently the higher resistance. In the cathodic range the opposite behavior is observed. At -300 mV, the annealed sample exhibits the smaller slope, i.e. the higher resistance. The monitored results for the investigated STO film by means of DC measurements are also in accordance with the behavior observed for the impedance measurements in the anodic and cathodic range, respectively (shown in Fig. 9.2 and Fig. 9.3).

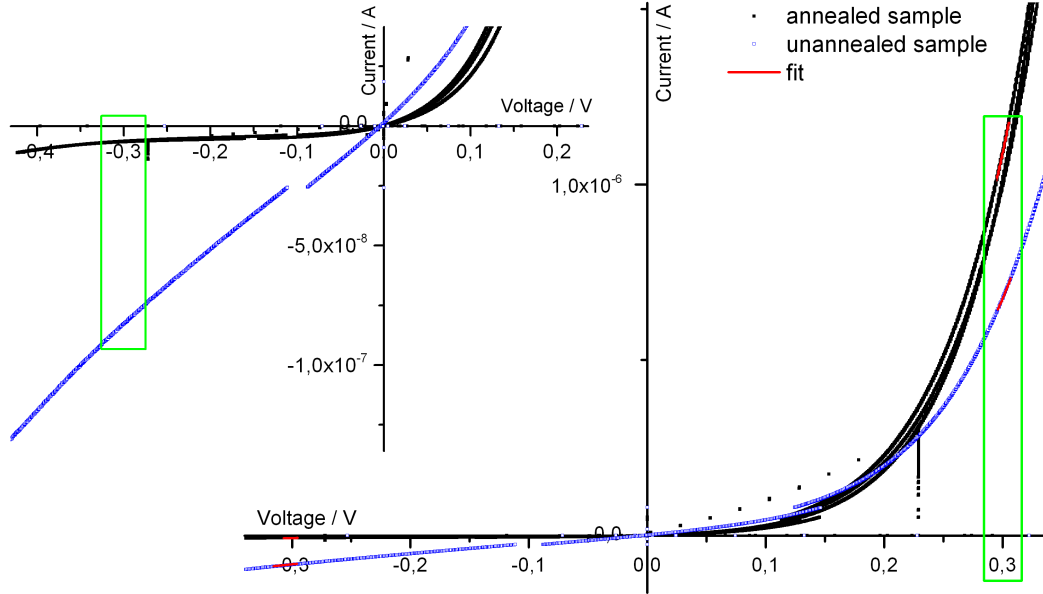


Figure 9.4

Fig. 9.4: Slowly measured current-voltage characteristics of the annealed (black) and unannealed (blue) 215 nm sample at 425°C (T_{Set}). The resistance values were evaluated at $+300$ mV and -300 mV for both U-I curves. The fit indicates the linearized part of the curve (for differential resistance).

In contrast to the 215 nm sample, the thinner sample (152 nm) shows the higher resistance in the unannealed sample, irrespective of polarity (anodic and cathodic). This is again depicted in Tab. 9.1 and Fig. 9.5. The changed behavior in the cathodic range compared with the 215 nm sample is clearly characterized by the significantly steeper curve in this bias range.

	150 nm sample		215 nm sample	
	-300 mV	300 mV	-300 mV	300 mV
unannealed	$4,2 \cdot 10^8 \Omega$	$2,9 \cdot 10^6 \Omega$	$2,96 \cdot 10^6 \Omega$	$1,23 \cdot 10^5 \Omega$
annealed	$1,5 \cdot 10^8 \Omega$	$8,3 \cdot 10^5 \Omega$	$6,33 \cdot 10^7 \Omega$	$6,25 \cdot 10^4 \Omega$

Tab. 9.1: The differential resistances for annealed and unannealed samples (152 and 215 nm) were analyzed in the two voltage points ± 300 mV. Red values are indicating the larger ones.

By a further analysis of the voltage range in the vicinity of 0 V an interesting observation can be made for the 215 nm sample. The shown results deviate from the results depicted in Fig. 9.4 by the fact that these measurements were performed on another electrode. The comparative plot of the current-voltage characteristics show a distinct difference in the bend of the two curves. Interestingly, the impedance spectra measured under unchanged conditions (same temperature, same electrode) at $+100$ mV also differ.

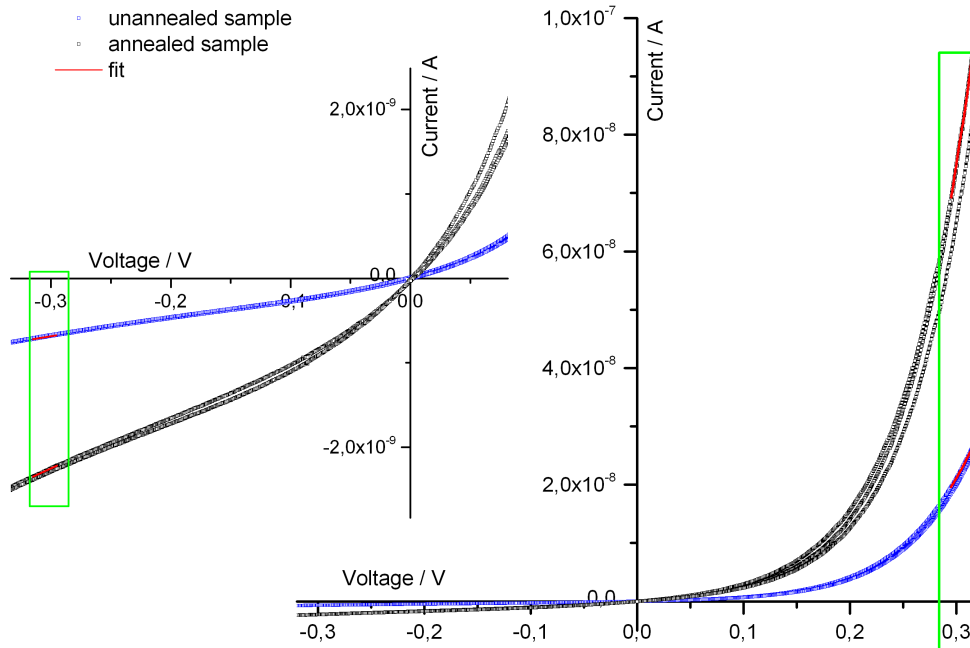


Figure 9.5

Fig. 9.5: Comparison of the slowly measured U-I curves monitored for an unannealed (blue) and an annealed (black) 152 nm sample at 375°C (T_{Set}). The resistance values at -300 mV and 300 mV were evaluated. The annealed sample shows in both bias cases the lower resistance.

Because of the fact that two thin films investigated by means of current-voltage characteristics, exhibit two different curves for the annealed sub-sample do not permit us to give a final explanation of the changed behavior due to the additional thermal preparation. However, the data obtained under applied bias voltage supports first indication that an additional annealing step during the thin layer preparation may have an effect on the material. This effect only becomes visible when applying an external electric field, and this suggests that it can be correlated with the motion of oxygen vacancies in the thin film due to the external driving force.

To further evaluate possible differences between annealed and unannealed samples, **fast current-voltage measurements** were performed at 400°C on a 157 nm sample. The resulting U-I curves are depicted in the following diagrams. For the unannealed sample (see Fig. 9.6) the fast curves strongly depend on the starting voltage. In the same Fig. 9.6 the anodic and the cathodic fast curves of the annealed sample are depicted. In the monitored current range, the curves show hardly any differences in shape. Hence, annealing had a significant consequence on the curves. Interestingly, the curve starting in the cathodic range crosses the x-axis in the origin, in contrast to the fast anodic

curve. Altogether, also these fast measured curves are an indication that the observed behavior is affected by possible structural changes of the layer due to thermal annealing.

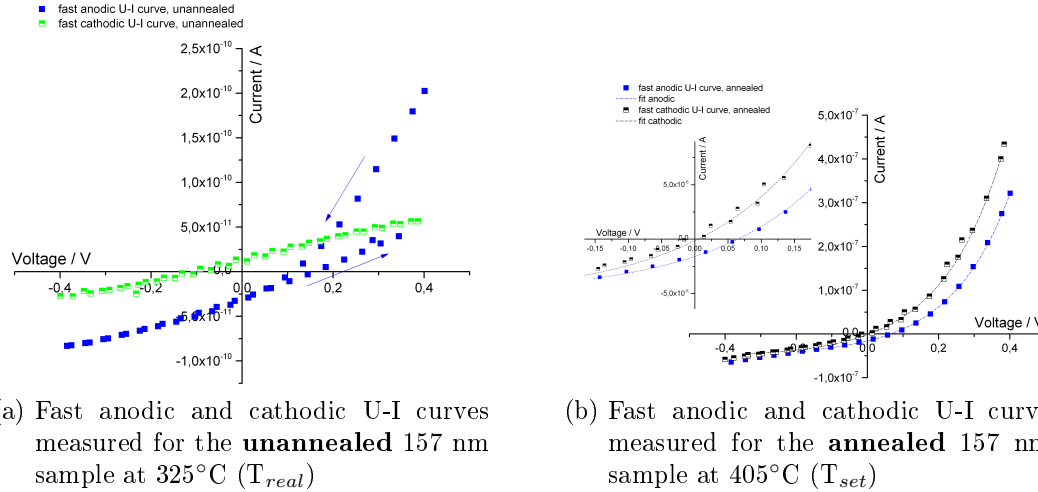


Figure 9.6

Fig. 9.6: Comparison of current-voltage characteristics obtained for an unannealed and an annealed sample (157 nm).

- **¹⁸O tracer experiments and subsequent SIMS analysis performed on unannealed and annealed SrTiO₃ samples**

Because of the fact, that the comparison between unannealed and annealed samples delivered interesting results, the annealed samples were also investigated by means of thermally induced ¹⁸O tracer incorporation and subsequent SIMS analysis. The tracer experiments with the annealed samples were performed together with the corresponding (same deposition procedure but without additional thermal annealing step) unannealed specimen, at 450°C for 30 min and under 200 mbar oxygen partial pressure.

The subsequently performed SIMS analysis provided results that are depicted in Fig. 9.7. The profiles of the ¹⁸O fraction detected within the thin films are plotted against depth. The total sputter crater depth was evaluated by means of DHM (digital holography method). The tracer profile of the unannealed sample is characterized by a sharp drop in the first few nanometers of the layer. Within this extremely short distance the ¹⁸O concentration reaches the natural abundance of 0.21%. No further profile in the cross section image of this sample can be found for the unannealed case.

For the annealed sample a distinctly different result could be monitored. The sharp concentration drop in the first few nm is something both samples have

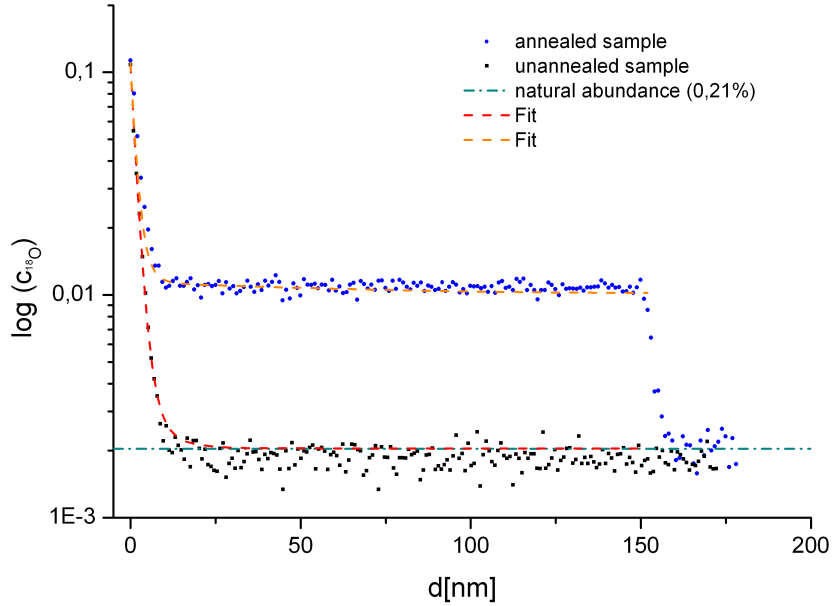


Figure 9.7

Fig. 9.7: ^{18}O tracer profile for an unannealed sample compared with data obtained for an annealed sample (152 nm sample).

in common. However, for the thermally treated sample the ^{18}O concentration does not reach the natural abundance concentration. Moreover, the thin film is constantly filled with an ^{18}O concentration of 1,1%. Because of the ionically blocking Nb-doped SrTiO_3 another sharp drop in the ^{18}O profile occurs at the interface layer|substrate. The concentration of the tracer in the substrate again correspond to the natural abundance.

For the analysis of the obtained ^{18}O profiles the approach of DeSouza *et al.*^[105] was used. Therein the existence of a space charge layer at the interface layer|gaseous surrounding atmosphere is assumed. For an evaluation of the tracer profile occurring in such an oxygen vacancy depleted zone the concentration of oxygen vacancies has to be expressed in terms of the electrical potential. Furthermore the second parameter that is correlated with the electrical potential is the length of the depletion zone. By considering these two parameters the measured tracer profiles were analyzed in terms of the tracer diffusion coefficient D^* and the oxygen exchange coefficient k^* by means of finite element simulation (used program: COMSOL, Comsol Multiphysics 4.2,USA).

With a length of the depletion zone of 22 nm and a total electrical potential difference of 290 mV we obtained a D^* -value of $5e^{-17}\text{m}^2/\text{s}$ and a k^* -value of $9e^{-13}\text{m}/\text{s}$ for the annealed sample. For the unannealed sample the length of

22 nm was held constant. For the electrical potential a value of 150 mV was used, resulting in values for $D^* = 1e^{-19} \text{m}^2/\text{s}$ and $k^* = 1e^{-13} \text{m}/\text{s}$, respectively. Because of the fact that no distinct tracer profiles are visible in both cases, the evaluation of the tracer diffusion coefficient is only a rough approximation. Furthermore, the approach of space charge layers located at the surface needs to be used with caution, because we found no further evidence for such an additionally depleted zone near the electrodes in other performed experiments. However, a difference between annealed and unannealed samples is very obvious and supports the assumption that the annealed layer is changed by the thermal treatment.

Conclusions

In this thesis pulsed laser deposited slightly Fe-doped SrTiO₃ (STO) thin films with a thickness between 60 and 420 nm were investigated by means of electrical impedance spectroscopy, DC measurements as well as DC load and relaxation experiments. The focus was laid on clarifying transport processes of charge carriers (oxygen vacancies, electrons and holes) within such thin MIEC (mixed ionic electronic conductor) layers.

- **Electrical impedance measurements without and with external bias**

Investigations on numerous SrTiO₃ thin films of varying thickness by means of impedance spectroscopy revealed severe differences compared to single crystalline as well as polycrystalline bulk samples. First of all, only one semicircle was generally monitored for the STO layers investigated without external applied bias. This coincides with results for nanocrystalline STO, published by Balaya *et. al.*^[77,78], dealing with the vanishing response of the bulk arc due to a reduced grain size. However, results from TEM investigation of Fe-STO films on Nb-STO exclude the formation of grain boundaries during preparation. The results are therefore discussed in terms of dislocations and surrounding space charge layers.

The analyzed conductivity values for thin STO films investigated in this work are, furthermore, 3 orders of magnitude smaller compared to values of polycrystalline pellet-type samples. The evaluated activation energies for the thin films are in the range of 1.6 eV, which is closer to values generally found for grain boundaries (1.4 – 1.7 eV) than to bulk activation energies (1 eV). This

again supports the interpretation in terms of an overlap of space charge layers due to a high density of dislocations. Consequently, the entire layer would be "homogeneously depleted" of positive charge carriers which explains the overall decreased conductivity while bulk permittivity is still preserved.

In addition, measurements with an external bias voltage of both polarities were performed. In this case, an additional low frequency feature appeared, either a second semicircle (usually under cathodic bias) or a loop (usually under anodic bias). An adapted equivalent circuit was able to describe both features. The high frequency arc, with a partly appearing shoulder, could be attributed to the resistance of the entire layer, connected in parallel to the geometrical capacitance of the layer. The fact that the high frequency arc changes upon bias is correlated with the (overlapping) space charges causing a "homogeneously" depleted situation in the thin STO layers.

The second arc/loop appearing in the impedance spectra under applied bias, was investigated in terms of temperature and bias dependence. It could be associated with a frequency-dependent change of the stoichiometric polarization (approximation of the classical Wagner-Hebb polarization) within the layers. Because of the slow voltage variation of the AC signal in the low frequency range, the oxygen vacancies can redistribute in the layer, together with the charge compensation reaction involving holes and electrons. The changing electronic current contribution is then measured and visible as a second semicircle or loop. Exact conditions which lead to a loop or semicircle are partly changing and most probably depend on the varying preparation conditions of thin films and electrodes (LSC).

- **Partial pressure dependent measurements**

By performing partial pressure variations another external driving force is applied onto the thin films. Measurements between 1% O₂ and 100% O₂ show that the conductivity of the samples only slightly depends on the oxygen partial pressure in this range. Although a plateau due to a dominating ionic conductivity cannot be excluded, it is considered as highly probable that the films are close to their minimum electronic conductivity between electron and hole conduction.

The measurements further showed the repeated occurrence of the high frequency shoulder in 1% O₂ atmosphere.

- **Current-voltage characteristics measured in 2 different time modes**

Two different scanning rates of the voltage range enabled a separation of processes with different characteristic time constants. Both types of experiments led to nonlinear current-voltage curves. However, the non-linearity of these U-I curves originates from two different processes.

The U-I measurements performed within the range of hours cause long range transport of oxygen vacancies and thus stoichiometric polarization within the layers. Hence, the analysis of the obtained results was performed by using the approach of Wagner and Hebb. Since the thin layers distinctly differ from single crystalline bulk material it is not surprising that the monitored current-voltage curves could not be entirely described by the Wagner-Hebb model.

By means of current-voltage measurements that were performed in a time range of seconds, a "pinned" non-stoichiometry distribution in the thin film was probed. Distinct differences in the shape of the curves could be found, depending on the starting voltage (0 V or ± 400 mV), i.e. the originally established steady state. For the anodic curve a pn-junction within the layer is assumed to be responsible for the observed non-linearity. Especially in the cathodic case it was difficult to find an appropriate scanning rate which avoids capacitive contributions.

- **DC load and relaxation experiments**

The time dependence of stoichiometric polarization in the layers was investigated by applying a constant bias voltage. Subsequent relaxation behavior was monitored by applying only a negligibly small bias voltage. The samples were investigated in terms of temperature and bias dependence and voltages of ± 250 mV and ± 400 mV were used in the experiments. Only comparatively small differences in the evaluated time constants could be found for DC load and relaxation experiments. Analysis of the activation energy of the time constants revealed a significant effect of polarity. Anodic DC stress showed in all cases the lower activation energy. In contrast to results obtained for single crystalline as well as polycrystalline STO bulk material, time constants

were only slightly bias dependent. This difference is in line with many other differences found in thin films compared to bulk material.

- **Comparison between unannealed and annealed samples**

Finally, the effect of a thermal annealing step on the transport properties of charge carriers within the layers was investigated. While the results obtained without bias did not show any clear evidence for a structural change, experiments under an external bias voltage revealed clear differences. The differences were especially visible in the slow current-voltage measurements. Additionally performed ^{18}O tracer diffusion experiments supported the assumption that especially oxygen ion transport is modified, leading to an increased tracer diffusion coefficient D^* after annealing.

List of Figures

2.1	Schematic picture of how non-stoichiometry influences the electrical properties in oxides by shifting the material into the n- as well as into the p-conducting regime ^[70]	6
2.2	Brouwer diagram for an undoped MO _X compound ^[2]	7
2.3	The top diagram shows the conductivity characteristics against partial pressure, the Brouwer diagram for the acceptor doped case is illustrated beneath. ^[70]	9
2.4	Charge carrier distribution in the Mott Schottky case.	11
2.5	A sketch of the oxygen vacancy concentration without bias is shown in (a), compared with the situation under applied DC bias (b). ^[72]	13
2.6	Behavior of a bicrystal SrTiO ₃ sample under an applied bias voltage, with a clear dependence of the grain boundaries on bias. ^[29]	13
2.7	Schematic picture of the space charge overlapping effect with decreasing grain size. ^[20]	14
2.8	Shift of the conductivity in the oxygen partial pressure range for single crystal bulk STO ^[16] (a) compared with nanocrystalline SrTiO ₃ (b). ^[52]	15
2.9	Results for locally resolved conductivity measurements after exposing SrTiO ₃ single crystals to a high DC field, compared with simulated data reported by Rodewald <i>et. al.</i> ^[33,34,67,68,79]	17

2.10	(a) Picture of a polarization cell with STO sandwiched between a blocking electrode and a reversible electrode, with the advantage of a self-sealed free STO surface ^[48] , (b) Schematic picture of the occurring electromigration process of oxygen vacancies due to field stress.	18
2.11	Concentration gradient of oxygen vacancies build up during a polarization experiment. In (a) the situation with one blocking electrode and in (b) with two blocking electrodes is illustrated. ^[2]	19
2.12	Simulation of the Wagner-Hebb case ($\alpha = 1$) for i_n , i_p as well as for i_{con} with $\sigma_p(0) = 3\sigma_n(0)$ (depicted in a) and $\sigma_p(0) = 10\sigma_n(0)$ (shown in b).	20
2.13	Process steps of forming a conductive Ag-filament (ON state) in one bias direction and after switching polarization reaching again the OFF state by dissolving the filament. ^[39]	21
2.14	In (a) the chemically etched surface of a (100) SrTiO ₃ sample is shown ^[85] ; the dark dots indicate dislocations. In (b) the spatial distribution of dislocations in a bulk SrTiO ₃ sample is illustrated. ^[86]	22
3.1	Schematic picture of the pulsed laser deposition set-up and photos of the entire set-up (without laser) and the plasma plume during deposition.	25
3.2	Spin coating of the photoresist on top of the LSC and subsequent heating \rightarrow exposure to UV light leads to a polymerization of the unprotected photoresist \rightarrow removal of the non-exposed photoresist \rightarrow etching away the uncoated LSC areas with diluted HCl \rightarrow removing the protective photoresist layer with acetone.	26
3.3	"Micro" set-up: heating stage, entire set-up and a schematic picture of the contacted sample situation.	27
3.4	Comparison between impedance data recorded within the "Micro" set-up and data obtained by using the "Micro-Macro" set-up for a 300 μm electrode prepared from a 180 nm LSC thin film on a 250 nm STO film, gives clear evidence of the cooling effect by the contacting needle. ^[90]	28
3.5	Drawing of the "Micro-Macro" test rod.	29

4.1	AFM images for Fe-doped SrTiO ₃ layers deposited on (a) Al ₂ O ₃ , (b) LaAlO ₃ and (c) Nb-SrTiO ₃ , exhibiting columnar layer growth due to deviating lattice parameters for (a) and (b) and planar layer growth for (c). In (d) layers deposited on differently orientated (100, 110 and 111) undoped STO substrates are compared.	33
4.2	TEM results for Fe-SrTiO ₃ thin films on (a) Al ₂ O ₃ , (b) LaAlO ₃ and (c) Nb-SrTiO ₃	34
5.1	Impedance data (Nyquist plot shown in (a) and (c), Modulus plot shown in (b) and (d)) for a 100 nm sample at 600°C and a 314 nm sample at 620°C, measured without applied bias voltage. In (a) and (c) the used equivalent circuits and the fits –in red and green– are also depicted in this illustration.	38
5.2	In (a) the resistance and in (b) the capacitance is plotted against the layer thickness for 500°C.	40
5.3	The shown Arrhenius plot contains the measured data for the thin layer samples, further grain and grain boundary data and literature data ^[33] are shown.	41
5.4	Nyquist plot (a) and Modulus plot (b) for the polycrystalline bulk sample of Fe-SrTiO ₃ at 454°C, measured in the "Micro-Macro" setup.	41
5.5	Representation of a bias cycle performed for the 413 nm sample at 700°C (T_{set}) in the "Micro" set-up, where the negative bias range is shown in (a) with an additional zoom in of the high frequency feature (b). The negative bias range with its appearing loop is shown in (c).	43
5.6	Results for checking whether the ongoing processes are fully reversible. The diagram in (a) shows a complete measurement series with all changes in temperature as well in bias. In (b) one cycle is emphasized and in (c) two cycles at the same temperature with more than 10 hours between these two cycles are compared.	44

5.7	In (a) the first approximation of an equivalent circuit is shown, which was adapted to the equivalent circuit depicted in (b). This is the equivalent circuit which was used to fit all the measured data.	44
5.8	Simulation of an impedance spectrum with a positive ΔR_{slow} , resulting in a second semicircle in the lower frequency part. . . .	47
5.9	Impedance spectrum containing a loop which results for a negative parameter ΔR_{slow}	47
5.10	Fitting results obtained from the given equivalent circuit for measurements on a 413 nm sample for different bias voltages (+200 mV (a) and -200 mV (b)) at 600°C. In (a) and (b) the data is plotted in the Nyquist plot. In (c) both spectra are compared in the Modulus plot.	48
5.11	Comparison of high frequency impedance arcs measured without an external applied bias for 4 layers with varying layer thickness. Measurements were performed on 300 μm electrodes using the "Micro" as well as the "Micro-Macro" set-up at around 615°C. . .	49
5.12	For the 125 nm sample despite the minor high frequency feature in the Nyquist plot (a) a distinct difference between spectra recorded at +200 mV and -200 mV can be found by illustrating the data in the Modulus plot (b).	49
5.13	Analysis of the high frequency response of a 125 nm layer at 540°C ("Micro-Macro" set-up), impedance spectra measured with different values of cathodic bias show only a minor development of a shoulder response. An evaluation of R_S , R_1 is still possible and the results are plotted together with $R_{HF,total}$	50
5.14	High frequency part of the impedance spectra (measured on a 413 nm sample) compared for different bias voltages (left hand side) and resistance values plotted against bias for the cathodic range (right hand side).	50
5.15	Analysis of the $R_{HF,total}$ part for a 157 nm sample at 600°C (T_{set}) investigated in the "Micro" set-up.	51
5.16	Analysis of the high frequency shoulder feature monitored for negative bias voltages for a 160 nm sample.	51

5.17	Illustration of the bias dependency of the conductivity for the HF–semicircle of the 413 nm sample (conductivity evaluated from $R_{HF,total}$ (a). Arrhenius plot for the complete applied voltage range (b).	53
5.18	Behavior of the high frequency part of the impedance measurement, performed on a 125 nm sample under different temperature over a bias range from -200 mV to $+200$ mV.	53
5.19	Evaluation of the thickness dependence of $R_{HF,total} \cdot A$ for ± 200 mV, measured at a temperature of around 600°C	54
5.20	Impedance plots of a 413 nm sample for the anodic (a) and the cathodic (b) range recorded at 700° (T_{set}). 3 different bias voltages are depicted and compared with the plot measured at 0 V bias.	54
5.21	Impedance plots of a 161 nm sample. The anodic (a) and the cathodic (b) range are separately depicted (700°C (T_{set})).	55
5.22	R_2 is plotted against bias for two different samples (125 and 161 nm). (Logarithmic plot shown in (a) and in (b) the linear plot is depicted.) In the cathodic range a distinct change in the resistance can be observed. In the anodic range only slight variations can be seen.	56
5.23	The ratio $\frac{R_2}{R_{HF,total}}$ is plotted against bias. 4 samples with varying thickness are compared. The low frequency features become in both cases increasingly important with increasing anodic as well as cathodic bias. (600°C actual temperature)	56
5.24	Arrhenius plot for the 413 nm sample. Analysis of a possible change in the activation energy of the low frequency process under different bias voltages.	57
5.25	Plot of low frequency resistance at $+300$ mV and -300 mV bias against layer thickness with an obvious bias dependence for resulting resistance in both bias regimes (600°C T_{set}).	57
5.26	A comparative illustration of all analyzed capacitance values for the 413 nm sample. Additionally, exemplary impedance plots for the anodic and the cathodic range as well as the used equivalent circuit should emphasize the observed behavior under applied bias (600°C T_{set}).	59

5.27	Capacitance evaluation over the entire bias range for 2 samples with different thickness ((a) 125 nm (634°C actual temperature) and (b) 160 nm (700°C T_{set})).	60
5.28	Temperature dependence of $C_{HF,total}$ for 2 samples with different thickness ((a) 413 nm and (b) 125 nm).	60
5.29	Low frequency capacitance C_2 plotted against bias.	61
5.30	C_2 for the 125 nm sample (a) and the 413 nm sample (b) are analyzed in terms of temperature dependence.	62
5.31	Image of impedance spectra of a 150 nm film for two different temperatures and three different bias voltages, in (a–c) impedance data for 556°C are shown, and compared with data monitored at 662°C (d–f).	63
5.32	Impedance spectra for different bias voltages measured on a 157 nm sample at 600°C (T_{set}). The red rectangles mark the variations observed.	64
5.33	Impedance plots for two different layers, which exhibit deviating characteristics under bias.	64
5.34	Kramers-Kronig analysis for the polycrystalline bulk sample (b) and a thin layer (413 nm) (a) without an external applied bias at 454°C and 700°C (T_{set}), respectively.	66
5.35	Performing the Kramers-Kronig test for a 413 nm sample measured under +200 mV applied bias (a) and –200 mV applied bias (b). Measured at 700°C (T_{set}).	66
5.36	Performing the Kramers-Kronig test for a 157 nm sample (600°C, T_{set}) (a) and a 160 nm sample (700°C, T_{set}) (b) measured under +300 mV applied bias.	67
6.1	Resistance measured during partial pressure cycles.	69
6.2	Impedance data for the measurements under variable oxygen partial pressure (100% O ₂ , air and 1% O ₂) for 413 nm sample (a) and 157 nm sample (b) at 600°C (T_{set}).	70
6.3	Partial pressure dependent conductivities $\sigma_{HF,total}$ of the 157 nm layer for the three temperatures 675°C, 560°C and 475°C.	70
6.4	Partial pressure dependent conductivities $\sigma_{HF,total}$ of the 413 nm layer again for the three temperatures 675°C, 560°C and 475°C.	71

6.5	Arrhenius plots for a 157 nm sample (a) and a 413 nm sample (b), the results for air, 100% oxygen and 0,1% oxygen are compared.	71
6.6	Impedance data for the 413 nm layer under different partial pressure (100% O ₂ and 1% O ₂) and additionally applied bias voltage (−200 mV (a) and +200 mV (b)) at 600°C (T _{set}).	72
6.7	Impedance data for the 157 nm layer under 100% O ₂ and 1% O ₂ with an applied bias voltage of −200 mV (a) and +200 mV (b) at 600°C(T _{set}).	72
6.8	Capacitance values of the high (a) frequency part of the spectra and the low (b) frequency part are shown against bias for the thicker sample (413 nm) at 600°C (T _{set}).	73
6.9	The resistance of the 413 nm sample is also evaluated for the high (a) and the low frequency (b) part of the impedance spectra, for three different p _{O₂} (600°C, T _{set}).	73
7.1	Slow current-voltage curve monitored for a 152 nm at 330°C (true temperature). The measurement was performed in the "Micro-Macro" set-up. The initial change of the current is indicated in cyan colored symbols.	77
7.2	Impedance spectra measured at 375°C (set temperature) for a 110 nm sample. Comparison of the spectra monitored under −300 mV and +300 mV, with a difference in resistance values of about 3 orders of magnitude.	78
7.3	Slowly measured U-I curve and the appropriate fit (Eq. 7.2) illustrated for a 152 nm sample at 429°C.	80
7.4	Comparison of U-I curves measured for 3 different samples. The temperature used was for all of those samples in the range of 375°C.	81

-
- 7.5 U-I characteristics can be measured in different ways, this diagram compares a slowly measured U-I curve (black) with three fast measured curves for a 152 nm at 375°C ("Micro" set-up). The difference between these curves originates in the starting point. The green curve starts at +400 mV, the blue one has its origin at 0 V bias and the purple one represents the curve starting at -400 mV. 82
- 7.6 Illustration of the fast U-I curve (152 nm sample, 375°C, "Micro" set-up) starting in the anodic range (a), with the continuously changing current, while reaching a steady state in the first 5 minutes, followed by applying a fast voltage change. The measurement was extended into the cathodic range (b), and was performed in the backward direction with the result of achieving a forward and a backward curve. 83
- 7.7 The same experiment as it was performed for the anodic curve (see again Fig. 7.6), was executed in the cathodic regime. The observation of shifted forward and backward curves was similar which is indicated in (a) for the complete bias range. In (b) a zoom-in of the cathodic range is depicted 84
- 7.8 Illustration of the fast U-I curve (purple colored circles), with its starting voltage of 0 V. To emphasize that this curve reflects a sample in a very different state, the fast curve starting in the cathodic range is also depicted. 85
- 7.9 The fact that no intercept with the real axis in the cathodic case could be observed, manifests itself in the difficulty of defining an appropriate measuring time. For several thin films the reported data switched either into case (a) (too fast) or case (c) (too slow), both depicted with magnification. In (b) the case of a more or less unperturbed U-I curve is shown. 86
- 7.10 Illustration of the fast anodic (a) and cathodic (b) curve for the unannealed 152 nm sample at 376°C (T_{real}). 89
- 7.11 In comparison to the annealed sample (Fig. 7.10), fast U-I curves starting in the anodic (a) and the cathodic (b) regime were also measured for the annealed sample at the same temperature. 89

7.12	Illustration of the fast U-I curves, starting from an anodic (a) and a cathodic (b) bias, for the 110 nm sample at a temperature of 402°C (T_{real}).	90
7.13	Comparison of two fast measured anodic U-I curves at 400°C in the anodic regime for two layers of different thickness (240 nm and 110 nm).	91
7.14	U-I curve for the cathodic range compared with impedance data recorded under cathodic bias. Two different temperatures were used for these two experiments. Still this can illustrate the origin of the second semicircle.	92
7.15	Anodic range of the same U-I curve as in Fig. 7.14 compared with anodic impedance data. Again two different temperatures were applied but the reason of the loop becomes very obvious.	92
8.1	Characteristic curves for an anodic (black circles) and a cathodic (green squares) DC load experiment for a 152 nm sample at 354°C (T_{act}) depicted in (a). The relaxation curves starting from both polarities are shown in (b) for the same sample and temperature.	95
8.2	Comparison of the fitting results obtained with Eq. 8.1 and Eq. 8.2 for a relaxation experiment. The measurement was performed at 375°C (T_{set}) and the relaxation cycle started at -250 mV.	96
8.3	Exemplary illustration of the used fitting routine for polarization experiments. The measurements were performed at 375°C (T_{set}). The applied bias voltages were ± 100 mV.	96
8.4	Illustration of the excellent reproducibility of the resistance of the thin film under DC stress as well as during relaxation.	97
8.5	Arrhenius plots of the relaxation processes starting in the anodic as well as in the cathodic regime, compared with the curves for the anodic and cathodic DC load (± 250 mV applied DC voltage); 215 nm sample measured in the "Micro-Macro" set-up.	98
8.6	Analysis of the activation energy of τ for the polarization experiment performed on 2 different samples.	99

8.7	Investigation of a 152 nm layer at 375°C (set temperature) as a function of bias voltage for the relaxation process after anodic (a) as well as after cathodic (b) DC load. In addition the evaluated characteristic times for both cases are plotted against bias voltage.	100
8.8	Anodic (a) and cathodic (b) DC bias voltage was applied to the sample (152 nm) the relaxation behavior of which is shown in Fig. 8.7. In addition the bias dependence of τ is also depicted for the DC load part of the experiment.	100
9.1	4 different samples (variation in thickness) were additionally annealed and the monitored impedance data is compared with results for the unannealed samples in a temperature range from around 700°C to 450°C.	102
9.2	Impedance data for the annealed and unannealed 215 nm sample. Measurements were performed at 500°C (T_{Set}) under 300 mV anodic and cathodic bias voltage. The differences in the total resistance are also depicted in these diagrams.	103
9.3	The bias investigations were also performed for the 413 nm sample. The measurement parameters temperature and bias voltage were held constant (500°C (T_{Set}) and ± 300 mV bias)	103
9.4	Slowly measured current-voltage characteristics of the annealed (black) and unannealed (blue) 215 nm sample at 425°C (T_{Set}). The resistance values were evaluated at +300 mV and -300 mV for both U-I curves. The fit indicates the linearized part of the curve (for differential resistance).	105
9.5	Comparison of the slowly measured U-I curves monitored for an unannealed (blue) and an annealed (black) 152 nm sample at 375°C (T_{Set}). The resistance values at -300 mV and 300 mV were evaluated. The annealed sample shows in both bias cases the lower resistance.	106
9.6	Comparison of current-voltage characteristics obtained for an unannealed and an annealed sample (157 nm).	107
9.7	^{18}O tracer profile for an unannealed sample compared with data obtained for an annealed sample (152 nm sample).	108

Bibliography

- [1] R. Waser. Electronic properties of grain boundaries in SrTiO₃ and BaTiO₃ ceramics. *Solid State Ionics*, 75:89–99, 1995.
- [2] J. Maier. *Festkörper - Fehler und Funktion (Prinzipien der Physikalischen Festkörperchemie)*. Teubner Studienbücher, 2000.
- [3] R. Waser. Bulk conductivity and defect chemistry of acceptor-doped strontium titanate in the quenched state. *Journal of the American Ceramic Society*, 74:1934–1940, 1991.
- [4] J. Daniels and K.H. Haerdtl. Defect chemistry and electrical conductivity of doped barium titanate ceramics Part I. Electrical conductivity at high temperatures of donor doped barium titanate. *Philips Research Reports*, 31:489–504, 1976.
- [5] J. Daniels. Defect chemistry and electrical conductivity of doped barium titanate ceramics part II. Defect equilibria in acceptor doped barium titanate. *Philips Research Reports*, 31:505–515, 1976.
- [6] J. Maier. Ionic transport in nano-sized systems. *Solid State Ionics*, 175:7–12, 2004.
- [7] D. Hennings. Defect chemistry and electrical conductivity of doped barium titanate ceramics part III. Thermogravimetric investigations. *Philips Research Reports*, 31:516–525, 1976.
- [8] R. Wernicke. Defect chemistry and electrical conductivity of doped barium titanate ceramics part IV. The kinetics of equilibrium restoration in barium titanate ceramics. *Philips Research Reports*, 31:526–543, 1976.

-
- [9] R. Wernicke. *Die Diffusion von Sauerstoffleerstellen und die Kinetik von Fehlordnungsprozessen in Bariumtitanat und Strontiumtitanat*. PhD thesis, Rheinisch-Westfaelische Technische Hochschule Aachen, 1975.
- [10] M.V. Raymond and D.M. Smyth. Defect chemistry and transport properties of $\text{Pb}(\text{Zr}_{0.5}\text{Ti}_{0.5})\text{O}_3$. *Integrated Ferroelectrics*, 4:145–154, 1994.
- [11] M.V. Raymond and D.M. Smyth. Defects and charge transport in perovskite ferroelectrics. *Journal of Physics and Chemistry of Solids*, 57:1507–1511, 1996.
- [12] D.M. Smyth. Defect structure in perovskite titanates. *Current Opinion in Solid State and Materials Science*, 1:692–697, 1996.
- [13] Y.S. Lee and H.I. Yoo. Current voltage characteristic of BaTiO_{3-z} in its mixed n/p regime under oxygen potential gradients. *Solid State Ionics*, 150:373–382, 2002.
- [14] F. Noll, W. Muench, I. Denk, and J. Maier. SrTiO_3 as a prototype of a mixed conductor: Conductivities, oxygen diffusion and boundary effects. *Solid State Ionics*, 86, Part 2:711 – 717, 1996.
- [15] R. Merkle and J. Maier. Oxygen incorporation into Fe-doped SrTiO_3 : Mechanistic interpretation of the surface reaction. *Physical Chemistry Chemical Physics*, 4:4140–4148, 2002.
- [16] R. Merkle and J. Maier. How is oxygen incorporated into oxides? A comprehensive kinetic study of a simple solid-state reaction with SrTiO_3 as a model material. *Angewandte Chemie - International Edition*, 47:3874–3894, 2008.
- [17] P.C. McIntyre. Point defect equilibrium in strontium titanate thin films. *Journal of Applied Physics*, 89:8074–8084, 2001.
- [18] I. Denk, W. Muench, and J. Maier. Partial conductivities in SrTiO_3 : bulk polarization experiments, oxygen concentration cell measurements, and defect-chemical modeling. *Journal of the American Ceramic Society*, 78:3265–3272, 1995.

-
- [19] J. Claus, M. Leonhardt, and J. Maier. Tracer diffusion and chemical diffusion of oxygen in acceptor doped SrTiO₃. *Journal of Physics and Chemistry of Solids*, 61:1199–1207, 2000.
- [20] J. Maier. Defect chemistry and ionic conductivity in thin films. *Solid State Ionics*, 23:59–67, 1987.
- [21] R.A. DeSouza and J. Fleig. SrTiO₃: A model electroceramic. *Zeitschrift für Metallkunde*, 3:218–225, 2003.
- [22] J. Abrantes, A. Ferreira, J. Labrincha, and J. Frade. Electrical conductivity of Sr_{1-x}TiO_{3-z} materials. *Ionics*, 3:436–441, 1997.
- [23] R. Moos and K.H. Hardtl. Defect Chemistry of Donor-Doped and Undoped Strontium Titanate Ceramics between 1000°C and 1400°C. *Journal of the American Ceramic Society*, 80:2549–2562, 1997.
- [24] S.K. Rout and J. Bera. Grain and Grain-Boundary Study of Acceptor Doped SrTiO₃ Ceramics Using Impedance Spectroscopy. *Ferroelectrics*, 323:79–84, 2005.
- [25] R.A. De Souza, J. Fleig, J. Maier, O. Kienzle, Z. Zhang, W. Sigle, and M. Rühle. Electrical and Structural Characterization of a Low-Angle Tilt Grain Boundary in Iron-Doped Strontium Titanate. *Journal of the American Ceramic Society*, 86:922–928, 2003.
- [26] R.A. De Souza, V. Metlenko, D. Park, and T.E. Weirich. Behavior of oxygen vacancies in single-crystal SrTiO₃: Equilibrium distribution and diffusion kinetics. *Physical Review B*, 85:174109, 2012.
- [27] R. Hagenbeck and R. Waser. Influence of temperature and interface charge on the grain-boundary conductivity in acceptor-doped SrTiO₃ ceramics. *Journal of Applied Physics*, 83:2083–2092, 1998.
- [28] I. Denk, F. Noll, and J. Maier. In situ Profiles of Oxygen Diffusion in SrTiO₃: Bulk Behavior and Boundary Effects. *Journal of the American Ceramic Society*, 80:279–285, 1997.
- [29] I. Denk, J. Claus, and J. Maier. Electrochemical investigations of SrTiO₃ boundaries. *Journal of the Electrochemical Society*, 144:3526–3536, 1997.

-
- [30] A.A.L. Ferreira, J.C.C. Abrantes, J.R. Jurado, and J.R. Frade. Oxygen stoichiometry of $\text{Sr}_{0.97}(\text{Ti}, \text{Fe})\text{O}_{3-z}$ materials. *Solid State Ionics*, 135:761–764, 2000.
- [31] W. Liu and C.A. Randall. Thermally Stimulated Relaxation in Fe-Doped SrTiO_3 Systems: I. Single Crystals. *Journal of the American Ceramic Society*, 91:3245–3250, 2008.
- [32] W. Liu and C.A. Randall. Thermally Stimulated Relaxation in Fe-Doped SrTiO_3 Systems: II. Degradation of SrTiO_3 Dielectrics. *Journal of the American Ceramic Society*, 91:3251–3257, 2008.
- [33] S. Rodewald. *Lokale elektrochemische Charakterisierung von Leitfähigkeitsinhomogenitäten in Fe dotiertem SrTiO_3* . PhD thesis, Max-Planck Institut für Festkörperforschung, 1999.
- [34] S. Rodewald and J. Fleig, J. and Maier. Resistance degradation of iron-doped strontium titanate investigated by spatially resolved conductivity measurements. *Journal of the American Ceramic Society*, 83:1969–1976, 2000.
- [35] S.V. Kalinin and D.A. Bonnell. Local electronic transport at grain boundaries in Nb-doped SrTiO_3 . *Physical Review B - Condensed Matter and Materials Physics*, 70:1–10, 2004.
- [36] R. Waser, T. Baiatu, and K.H. Härdtl. dc Electrical Degradation of Perovskite-Type Titanates: I, Ceramics. *Journal of the American Ceramic Society*, 73:1645–1653, 1990.
- [37] R. Waser, T. Baiatu, and K.H. Härdtl. dc Electrical Degradation of Perovskite-Type Titanates: II, Single Crystals. *Journal of the American Ceramic Society*, 73:1654–1662, 1990.
- [38] T. Baiatu, R. Waser, and K.H. Härdtl. dc Electrical Degradation of Perovskite-Type Titanates: III, A Model of the Mechanism. *Journal of the American Ceramic Society*, 73:1663–1673, 1990.
- [39] R. Waser, R. Dittmann, C. Staikov, and K. Szot. Redox-based resistive switching memories nanoionic mechanisms, prospects, and challenges. *Advanced Materials*, 21:2632–2663, 2009.

-
- [40] K. Szot, W. Speier, G. Bihlmayer, and R. Waser. Switching the electrical resistance of individual dislocations in single-crystalline SrTiO₃. *Nature Materials*, 5:312–320, 2006.
- [41] K. Szot, R. Dittmann, W. Speier, and R. Waser. Nanoscale resistive switching in SrTiO₃ thin films. *Physica Status Solidi - Rapid Research Letters*, 1:R86–R88, 2007.
- [42] I. Riess. Measurement of ionic conductivity in semiconductors and metals. *Solid State Ionics*, 44:199–205, 1991.
- [43] I. Riess. Measurements of electronic and ionic partial conductivities in mixed conductors, without the use of blocking electrodes. *Solid State Ionics*, 44:207–214, 1991.
- [44] I. Riess. Four point hebb-wagner polarization method for determining the electronic conductivity in mixed ionic-electronic conductors. *Solid State Ionics*, 51:219–229, 1992.
- [45] I. Riess. Analysis of hebb-wagner polarization measurements under relatively high applied voltages. *Solid State Ionics*, 66:331–336, 1993.
- [46] R. Muenstermann, T. Menke, R. Dittmann, S. Mi, C.-L. Jia, D. Park, and J. Mayer. Correlation between growth kinetics and nanoscale resistive switching properties of SrTiO₃ thin films. *Journal of Applied Physics*, 108, 2010.
- [47] R. Muenstermann, T. Menke, R. Dittmann, and R. Waser. Coexistence of filamentary and homogeneous resistive switching in Fe-doped SrTiO₃ thin-film memristive devices. *Advanced Materials*, 22:4819–4822, 2010.
- [48] X Guo and J Maier. On the Hebb–Wagner polarisation of SrTiO₃ doped with redox-active ions. *Solid State Ionics*, 130:267–280, 2000.
- [49] M. Vollmann and R. Waser. Grain boundary defect chemistry of acceptor-doped titanates: space charge layer width. *Journal of the American Ceramic Society*, 77:235–243, 1994.
- [50] M. Vollmann, R. Hagenbeck, and R. Waser. Grain-boundary defect chemistry of acceptor-doped titanates: Inversion layer and low-field conduction. *Journal of the American Ceramic Society*, 80:2301–2314, 1997.

-
- [51] K. Takehara, Y. Sato, T. Tohei, N. Shibata, and Y. Ikuhara. Titanium enrichment and strontium depletion near edge dislocation in strontium titanate (001)/(110) low-angle tilt grain boundary. *Journal of Materials Science*, 49:3962–3969, 2014.
- [52] P. Lupetin, G. Gregori, and J. Maier. Mesoscopic charge carriers chemistry in nanocrystalline SrTiO₃. *Angewandte Chemie - International Edition*, 49:10123–10126, 2010.
- [53] J. Fleig, S. Rodewald, and J. Maier. Microcontact impedance measurements of individual highly resistive grain boundaries: General aspects and application to acceptor-doped SrTiO₃. *Journal of Applied Physics*, 87:2372–2381, 2000.
- [54] R. Hagenbeck and R. Waser. Detailed temperature dependence of the space charge layer width at grain boundaries in acceptor-doped SrTiO₃-ceramics. *Journal of the European Ceramic Society*, 19:683–686, 1999.
- [55] N.D. Browning, J.P. Buban, H.O. Moltaji, S.J. Pennycook, G. Duscher, K.D. Johnson, R.P. Rodrigues, and V.P. Dravid. The influence of atomic structure on the formation of electrical barriers at grain boundaries in SrTiO₃. *Applied Physics Letters*, 74:2638–2640, 1999.
- [56] G. Gregori, P. Lupetin, and J. Maier. Huge electrical conductivity changes in SrTiO₃ upon reduction of the grain size to the nanoscale. volume 45, pages 19–24, 2012.
- [57] R.A. De Souza. The formation of equilibrium space-charge zones at grain boundaries in the perovskite oxide SrTiO₃. *Physical Chemistry and Chemical Physics*, 11:9939–9969, 2009.
- [58] J. Szade, K. Szot, M. Kulpa, Ch. Kubacki, J. and Lenser, R. Dittmann, and R. Waser. Electronic structure of epitaxial Fe-doped SrTiO₃ thin films. *Phase Transitions*, 84:489–500, 2011.
- [59] J.L.M. Rupp, P. Reinhard, D. Pergolesi, T. Ryll, R. Toelke, and E. Traversa. Electric-field-induced current-voltage characteristics in electronic conducting perovskite thin films. *Applied Physics Letters*, 100, 2012.

-
- [60] Y.L. Qin, C.L. Jia, K. Urban, J.H. Hao, and X.X. Xi. Dislocations in SrTiO₃ thin films grown on LaAlO₃ substrates. *Journal of Materials Research*, 17:3117–3126, 12 2002.
- [61] C. Ohly, S. Hoffmann-Eifert, K. Szot, and R. Waser. Electrical conductivity and segregation effects of doped SrTiO₃ thin films. *Journal of the European Ceramic Society*, 21:1673 – 1676, 2001.
- [62] C. Ohly, S. Hoffmann, K. Szot, and R. Waser. High temperature conductivity behavior of doped SrTiO₃ thin films. *Integrated Ferroelectrics*, 33:363–372, 2001.
- [63] C. Ohly, S. Hoffmann-Eifert, X. Guo, J. Schubert, and R. Waser. Electrical Conductivity of Epitaxial SrTiO₃ Thin Films as a Function of Oxygen Partial Pressure and Temperature. *Journal of the American Ceramic Society*, 89:2845–2852, 2006.
- [64] D. Kajewski, J. Szade, J. Kubacki, K. Szot, A. Koehl, Ch. Lenser, and R. Dittmann. Fe valence determination in doped SrTiO₃ epitaxial films. 2012.
- [65] J.C.C. Abrantes, J.A. Labrincha, and J.R. Frade. Applicability of the brick layer model to describe the grain boundary properties of strontium titanate ceramics. *Journal of the European Ceramic Society*, 20:1603–1609, 2000.
- [66] J.C.C. Abrantes, J.A. Labrincha, and J.R. Frade. Representations of impedance spectra of ceramics: Part II. spectra of polycrystalline SrTiO₃. *Materials Research Bulletin*, 35:965–976, 2000.
- [67] S. Rodewald, N. Sakai, K. Yamaji, H. Yokokawa, J. Fleig, and J. Maier. The Effect of the Oxygen Exchange at Electrodes on the High-Voltage Electrocoloration of Fe-Doped SrTiO₃ Single Crystals: A Combined SIMS and Microelectrode Impedance Study. *Journal of Electroceramics*, 7:95–105, 2001.
- [68] S. Rodewald, J. Fleig, and J. Maier. Microcontact Impedance Spectroscopy at Single Grain Boundaries in Fe-Doped SrTiO₃ Polycrystals. *Journal of the American Ceramic Society*, 84:521–530, 2001.

-
- [69] F.A. Kröger and H.J. Vink. Relations between the concentrations of imperfections in crystalline solids. *Solid State Physics*, 3:307–435, 1956.
- [70] R.J.D. Tilley. *Defects in Solids*. Wiley, 2008.
- [71] S. Kim, J. Fleig, and J. Maier. Space charge conduction: Simple analytical solutions for ionic and mixed conductors and application to nanocrystalline ceria. *Physical Chemistry Chemical Physics*, 5:2268–2273, 2003.
- [72] X. Guo, J. Fleig, and J. Maier. Determination of electronic and ionic partial conductivities of a grain boundary: method and application to acceptor-doped SrTiO₃. *Solid State Ionics*, 154 and 155:563–569, 2002.
- [73] X. Guo, S. Mi, and R. Waser. Nonlinear Electrical Properties of Grain Boundaries in Oxygen Ion Conductors: Acceptor-Doped Ceria. *Electrochemical and Solid-State Letters*, 8:J1–J3, 2005.
- [74] X. Guo and R. Waser. Electrical properties of the grain boundaries of oxygen ion conductors: Acceptor-doped zirconia and ceria. *Progress in Materials Science*, 51:151–210, 2006.
- [75] R.A. De Souza and J. Maier. Capacitance of single crystal and low-angle tilt bicrystals of Fe-doped SrTiO₃. *Faraday Discussions*, 134:235–245, 2007.
- [76] H.L. Tuller. Ionic conduction in nanocrystalline materials. *Solid State Ionics*, 131:143–157, 2000.
- [77] P. Balaya, J. Jamnik, J. Fleig, and J. Maier. Mesoscopic electrical conduction in nanocrystalline SrTiO₃. *Applied Physics Letters*, 88:062109, 2006.
- [78] P. Balaya, J. Jamnik, J. Fleig, and J. Maier. Mesoscopic Hole Conduction in Nanocrystalline SrTiO₃. *Journal of The Electrochemical Society*, 154:P69–P76, 2007.
- [79] S. Rodewald, J. Fleig, and J. Maier. Measurement of conductivity profiles in acceptor-doped strontium titanate. *Journal of the European Ceramic Society*, 19:797–801, 1999.

-
- [80] M.H. Hebb. Electrical conductivity of silver sulfide. *Journal of Chemical Physics*, 20:185, 1952.
- [81] C. Wagner. Galvanic cells with solid electrolytes involving ionic and electronic conduction. *Proc. 7th Meeting of Int. Comm. on Electrochemical Thermodynamics and Kinetics, Lindau*, page 361, 1957.
- [82] C.L. Jia, A. Thust, and K. Urban. Atomic-scale analysis of the oxygen configuration at a SrTiO₃ dislocation core. *Physical Review Letters*, 95, 2005.
- [83] C.L. Jia, L. Houben, and K. Urban. Atom vacancies at a screw dislocation core in SrTiO₃. *Philosophical Magazine Letters*, 86:683–690, 2006.
- [84] L. Jin, X. Guo, and C.L. Jia. Tem study of 110-type 35.26° dislocations specially induced by polishing of srtio₃ single crystals. *Ultramicroscopy*, 134:77–85, 2013.
- [85] K. Szot, W. Speier, R. Carius, U. Zastrow, and W. Beyer. Localized metallic conductivity and self-healing during thermal reduction of SrTiO₃. *Physical Review Letters*, 88:755081–755084, 2002.
- [86] R. Wang, Y. Zhu, and S.M. Shapiro. Structural Defects and the Origin of the Second Length Scale in SrTiO₃. *Physical Review Letters*, 80:2370–2373, 1998.
- [87] A. Sawa. Resistive switching in transition metal oxides. *Materials Today*, 11:28–36, 2008.
- [88] A. Baikalov, Y.Q. Wang, B. Shen, B. Lorenz, S. Tsui, Y Y. Sun, Y.Y. Xue, and C.W. Chu. Field-driven hysteretic and reversible resistive switch at the AgPr_{0.7}Ca_{0.3}MnO₃ interface. *Applied Physics Letters*, 83:957–959, 2003.
- [89] J. Januschewsky, M. Stoeger-Pollach, F. Kubel, G. Friedbacher, and J. Fleig. La_{0.6}Sr_{0.4}CoO_{3-z} (LSC) thin film electrodes with very fast oxygen reduction kinetics prepared by a sol-Gel route. *Zeitschrift fur Physikalische Chemie*, 226:889–899, 2012.
- [90] T. Huber. in preparation.

-
- [91] M. Kubicek, G. Holzlechner, A. K. Opitz, S. Larisegger, H. Hutter, and J. Fleig. A novel ToF-SIMS operation mode for sub 100nm lateral resolution: Application and performance. *Applied Surface Science*, 289:407–416, 2014.
- [92] G. Holzlechner, M. Kubicek, H. Hutter, and J. Fleig. A novel ToF-SIMS operation mode for improved accuracy and lateral resolution of oxygen isotope measurements on oxides. *Journal of Analytical Atomic Spectrometry*, 28:1080–1089, 2013.
- [93] J. Fleig. The grain boundary impedance of random microstructures: numerical simulations and implications for the analysis of experimental data. *Solid State Ionics*, 150:181–193, 2002.
- [94] H.E. Weaver. Dielectric Properties of Single Crystals of SrTiO₃ at Low Temperatures. *Journal of Physical Chemistry*, 11:274–77, 1959.
- [95] W. Mitsui. Dielectric and X ray Studies of Ca_xBa_{1-x}TiO₃ and Ca_xSr_{1-x}TiO₃. *Physical Review*, 124:1345–59, 1961.
- [96] A. Samara. Pressure and Temperature Dependences of the Dielectric Properties of the Perovskites BaTiO₃ and SrTiO₃. *Physical Review*, 151:378–86, 1966.
- [97] U. Sakudo. Dielectric Properties of SrTiO₃ at Low Temperatures. *Physical Review Letters*, 26:851–53, 1971.
- [98] K.A. Mueller and H. Burkard. SrTiO₃: An Intrinsic Quantum Paraelectric below 4 K. *Physical Review B: Condensed Matter*, 19:3593–602, 1979.
- [99] J. Maier, G. Schwitzgebel, and H.J. Hagemann. Electrochemical Investigations of Conductivity and Chemical Diffusion in Pure and Doped Cubic SrTiO₃ and BaTiO₃. *Journal of Solid State Chemistry*, 58:1–13, 1985.
- [100] J. Jamnik, J. Maier, and S. Pejovnik. A powerful electrical network model for the impedance of mixed conductors. *Electrochimica Acta*, 44:4139–4145, 1999.

-
- [101] B.A. Boukamp. Electrochemical impedance spectroscopy in solid state ionics: recent advances. *Solid State Ionics*, 169:65 – 73, 2004.
- [102] B.A. Boukamp. A Linear Kronig–Kramers Transform Test for Impedance Data Validation. *Journal of The Electrochemical Society*, 142:1885–1894, 1995.
- [103] H. Naefe. Resistive Switching: A Solid-State Electrochemical Phenomenon. *ECS Journal of Solid State Science and Technology*, 2:P423–P431, 2013.
- [104] T. Kawada, T. Watanabe, A. Kaimai, K. Kawamura, Y. Nigara, and J. Mizusaki. High temperature transport properties in SrTiO₃ under an oxygen potential gradient. *Solid State Ionics*, 108:391 – 402, 1998.
- [105] R.A. De Souza and M. Martin. Using 18O/16O exchange to probe an equilibrium space-charge layer at the surface of a crystalline oxide: method and application. *Physical Chemistry Chemical Physics*, 10:2356–2367, 2008.

Acknowledgements

Ganz besonders möchte ich mich bei meinem Doktorvater Jürgen Fleig bedanken. Er hat mir von Beginn an die Freiheit gegeben meine eigenen Ideen umzusetzen. Trotzdem hatte er immer mal fünf Minuten Zeit um Probleme, Messdaten oder Ideen für neue Experimente zu besprechen. Aus den fünf Minuten wurden nicht selten 1 bis 2 Stunden, und bei einer Gruppe die zwischendurch aus bis zu 15 Leuten bestand, muss ich ihm diese intensive Betreuung sehr hoch anrechnen.

Weiters möchte ich mich bei Günter Faflek für seine fruchtbaren Ideen zu den, zunächst unmöglichen und dann doch erklärbaren induktiven Loops bedanken. Die Gespräche mit ihm haben mich in meiner Arbeit ein großes Stück vorangebracht, und auch ihn konnte ich immer mit meinen Fragen belästigen. Bei Prof. Gernot Fiedbacher und Prof. Bernardi möchte ich mich für die gute Zusammenarbeit im Rahmen der AFM- und TEM-Untersuchungen bedanken.

Ich könnte mich, was meine Arbeitsgruppe betrifft, fast dazu verleiten lassen zu sagen, dass ich die beste Arbeitsgruppe überhaupt hatte. Natürlich fehlen mir ein wenig die Vergleichsmöglichkeiten, aber in den 4 Jahren in denen ich Teil dieser Gruppe sein durfte, sind aus Kollegen Freunde geworden. In allen habe ich gute Zuhörer und Ratgeber gefunden, wenn es um wissenschaftliche Fragestellungen theoretischer und praktischer Natur ging. Nebenbei hatten wir ein extrem vielversprechendes Eistraining, haben unser Können beim Billard bewiesen und auch beim Bowling eine verdammt gute Figur gemacht. Dafür möchte ich mich bei der gesamten Mannschaft: Alex, Tobi, Gregor, Andi, Sandra, Edvinas, Plüsch und Plausch, Tschisi, Kathi, Silvia, Matthias sowie

Lukas, Till, Gerald und Markus (die wir leider an die Wissenschaft da draußen verloren haben), und natürlich bei Kurt und Udo sowie bei den Mädels aus dem Sekretariat, bedanken.

Vor allem möchte ich mich bei Alex für seine anscheinend grenzenlose Zeit sich mit den Problemen der anderen, mich inkludiert, zu beschäftigen und für die köstlichen Honiglieferungen bedanken. Kathi möchte ich für ihre unendliche Geduld danken, die sie mir mit meinen Proben für die SIMS entgegen gebracht hat und für ihre unglaubliche Ausdauer bezüglich Messzeiten und Reproduzierbarkeiten von Daten.

Mit dem Kurt ist das so eine Sache. Na ja, wir hatten nicht den perfektesten Start. Ich bin wohl zum tatsächlich ungünstigsten Zeitpunkt in sein Leben getreten. Freunde waren wir in dem Moment als er sich bei der Kaffeemaschine entschuldigt hat. Danke für all die Frühstückssemmerl, und den Spass den wir jeden Tag haben.

Im letzten Jahr habe ich in meinem neuen Zimmerkollegen Andi (Plüsch) einen sehr guten Freund gefunden. Für seine Unterstützung bei der Lösung der alltäglich auftretenden Problemchen, und für die Tatsache dass er mir regelmässig den Shaqtin' A Fool-Link schickt, möchte ich mich ebenfalls recht herzlich bedanken.

Zu ganz besonderem Dank bin ich meiner Martina verpflichtet, die ich zu Beginn des Studiums kennengelernt habe (dafür muss ich wohl auch dem Schicksal meinen Dank aussprechen), und die mit mir gemeinsam das Studium gemeistert hat. Während der Doktorarbeit hat sie mich trotz der Entfernung Wien-Graz immer ermutigt meinen Weg zu gehen. Egal ob per Telefon, Email oder SMS, ich konnte mit ihr meine Erfolge teilen und meine kleinen Niederlagen überstehen.

Meinen Eltern, Elfriede und Dietmar möchte ich für all die Jahre der Unterstützung danken, und dafür dass sie immer an mich glauben und hinter mir stehen. Meinem Bruder Patrick bin ich ebenfalls zu großem Dank verpflichtet. Wir teilen nicht nur die Freude am Eishockey spielen, sondern auch die Tätigkeit in der Wissenschaft, wodurch ich in ihm immer einen guten Gesprächspartner finde. Zu meinem großen Glück ist vor 3 Jahren auch mein Sascha in mein Leben getreten. Er hat mich in diesen Jahren immer motiviert

und aufgebaut, wenn ich nach dem ein oder anderen missglückten Experiment nachhause gekommen bin. Er hat meine Vergesslichkeit bezüglich alltäglicher Dinge hingenommen, die während dem Schreiben meiner Arbeit ab und an aufgetreten sind, und hat sich als hervorragender Hausmann herausgestellt. Ich danke ihm von Herzen und freue mich auf unsere gemeinsame Zukunft.

Zu guter Letzt möchte ich meiner Oma danken. Dafür, dass sie eine der stärksten Frauen ist die ich kenne, und dafür dass sie mich auf meinem Weg ebenfalls immer unterstützt hat.

Stefanie Huber

Curriculum Vitae

Education

- 2010–2014 **PhD thesis.**
- 2009–2010 **Master thesis.**
- 2003–2010 **Study of Technical Chemistry at the Vienna University of Technology**, *spezialied on "Chemistry and Technology of Materials"*.
- 6.2003 **Matura at the Oberstufenrealgymnasium – Englische Fräulein, Krems**, *spezialied on natural science.*

Master Thesis

- 2009–2010 **Division: Chemical Technologies**, *Research group: Nanomaterials and Composites.*
Title *Funktionell gradierte W/Cu-Interlayers für aktiv gekühlte "flat-tile" Divertor mock-ups*
Supervisors Ao.Univ.Prof.Dipl.-Ing.Dr.techn. Wolf-Dieter Schubert
Univ.Ass.Dipl.-Ing.Dr.techn. Christian Edtmaier

PhD Thesis

- 2010–2014 **Division: Electrochemistry**, *Research group: Solid State Electrochemistry and Electroceramics Laboratory.*
Title *Mass and charge transport properties of Fe-doped SrTiO₃ thin films and their dependence on DC voltage*
Supervisors Univ.Prof. Dipl.-Phys. Dr.rer.nat. Jürgen Fleig

Communication Skills

- 2014 Oral Presentation at the Bunsentagung, Hamburg, Germany
- 2014 Oral Presentation at the annual MPI Workshop, Reimsburg, Germany
- 2014 Oral Presentation at the GÖCH Symposium, Leoben
- 2013 Poster at the Solid State Ionics Conference, Kyoto, Japan
- 2012 Oral Presentation at the Electroceramics Conference at the University of Twente, Enschede, Netherlands
- 2011 Oral Presentation at the Junior Scientists Conference at the St. Petersburg mining institute, St. Petersburg, Russia
- 2011 Poster at the GÖCH Chemietage, Linz

Languages

- German **Mothertongue**
- English **Intermediate**